New approaches to exploration for IOCG-style mineralisation, Middleback Ranges, S.A.

Thesis submitted in accordance with the requirements of the University of Adelaide for an Honours Degree in Geology.

Holly Feltus

November 2013

THE UNIVERSITY of ADELAIDE

RUNNING TITLE

REE distributions: a new IOCG exploration tool.

ABSTRACT

Iron oxide copper gold (IOCG) systems display well-developed spatial zonation with respect to alteration assemblages, mineralogy and the distribution of rare earth elements (REE). The Middleback Ranges, South Australia, located in the Olympic Province, Gawler Craton, hosts anomalous Fe-oxide-bearing Cu-Au mineralisation, and are considered potentially prosperous for larger IOCG-style deposits. This study investigates whether the distribution of REE and other trace elements within selected minerals represents a potential exploration tool in the area. Iron-oxides (hematite and magnetite), potassium feldspar, albite and accessory minerals have been analysed by laser-ablation inductively-coupled plasma mass spectrometry (LA-ICP-MS) from two prospects (Moola and Princess) and in samples of the Myola Volcanics. The resultant multi-element datasets are compared to other IOCG systems.

The results support the presence of sizeable and/or multiple IOCG alteration envelopes within the Middleback Ranges. Significant evolving hydrothermal events resulted in hydrolithic alteration and remobilisation of REE within the Moola Prospect and Myola Volcanics.

Replacement of early magnetite by hematite (martitisation) in the Myola Volcanics is accompanied by an influx of REE visible on LA-ICP-MS element maps showing partial martitisation at the grain-scale. It is thus inferred the initial generation of magnetite must have pre-dated introduction of oxidised, REE-enriched hydrothermal fluids into the system. Sulphide assemblages observed within the Moola Prospect are complex and record sequential recrystallisation under evolving fS_2 and fO_2 conditions. Trace minerals, cycles of brecciation and replacement, and distributions of REE within minerals are similar to that observed in other IOCG domains. The Princess Prospect displays REE distributions in minerals which are dissimilar to the Moola Prospect, the Myola Volcanics and also those reported from other IOCG domains. This is interpreted as indicating that the Moola Prospect and Myola Volcanics in the south of the Middleback Ranges are more prospective IOCG targets.

KEYWORDS

Middleback Ranges, Iron-Oxide Cu-Au (IOCG), Rare Earth Elements (REE), incompatible elements, exploration, alteration.

TABLE OF CONTENTS

LIST OF FIGURES

LIST OF TABLES

INTRODUCTION

The Middleback Ranges are located in north-eastern Eyre Peninsula, 40 km west of Whyalla, South Australia, within the Gawler Craton (Figure 1) (Chamalaun & Porath 1967; Yeates 1990). Exploration work in and adjacent to the Middleback Ranges has identified several areas of anomalous Cu-Au mineralisation (McIntyre 2001). Due to limited access and minimal research, the defining features of this mineralisation and related alteration are poorly understood. Anomalous Cu-Au within the Gawler Craton is often affiliated to Iron-Oxide-Copper-Gold (IOCG)-style mineralisation since the discovery of the World-class Olympic Dam deposit, Prominent Hill, and in recent years, many other examples (Skirrow *et al.* 2007; Conor *et al.* 2010; Hayward & Skirrow 2010). Cu-Au mineralisation in the Middleback Ranges may represent an additional IOCG domain.

The Gawler Craton is a major Proterozoic crustal province that has experienced a complex multiphase deformation, metamorphic and intrusive history (e.g. Hand *et al.* 2007). IOCG deposits have become a major focus for exploration in the Gawler Craton due to their generally large size and good grade (e.g. Skirrow *et al.* 2007). The distribution of the IOCG deposits is constrained to a >500 km long Mesoproterozoic metallogenic belt, known as the Olympic Province, within which all prospects studied here lie (Figure 1) (Skirrow *et al.* 2007).

Alteration footprints in IOCG systems hosted within igneous rocks appears to show well-developed spatial zonation (Figure 2) (Hitzman *et al.* 1992). Sodic alteration is dominant at deeper levels within the system and is characterised by albite-magnetite ± actinolite or chlorite, little to no quartz and an association with magnetite. A zone of potassic alteration sits spatially above sodic alteration (Hitzman *et al.* 1992). This

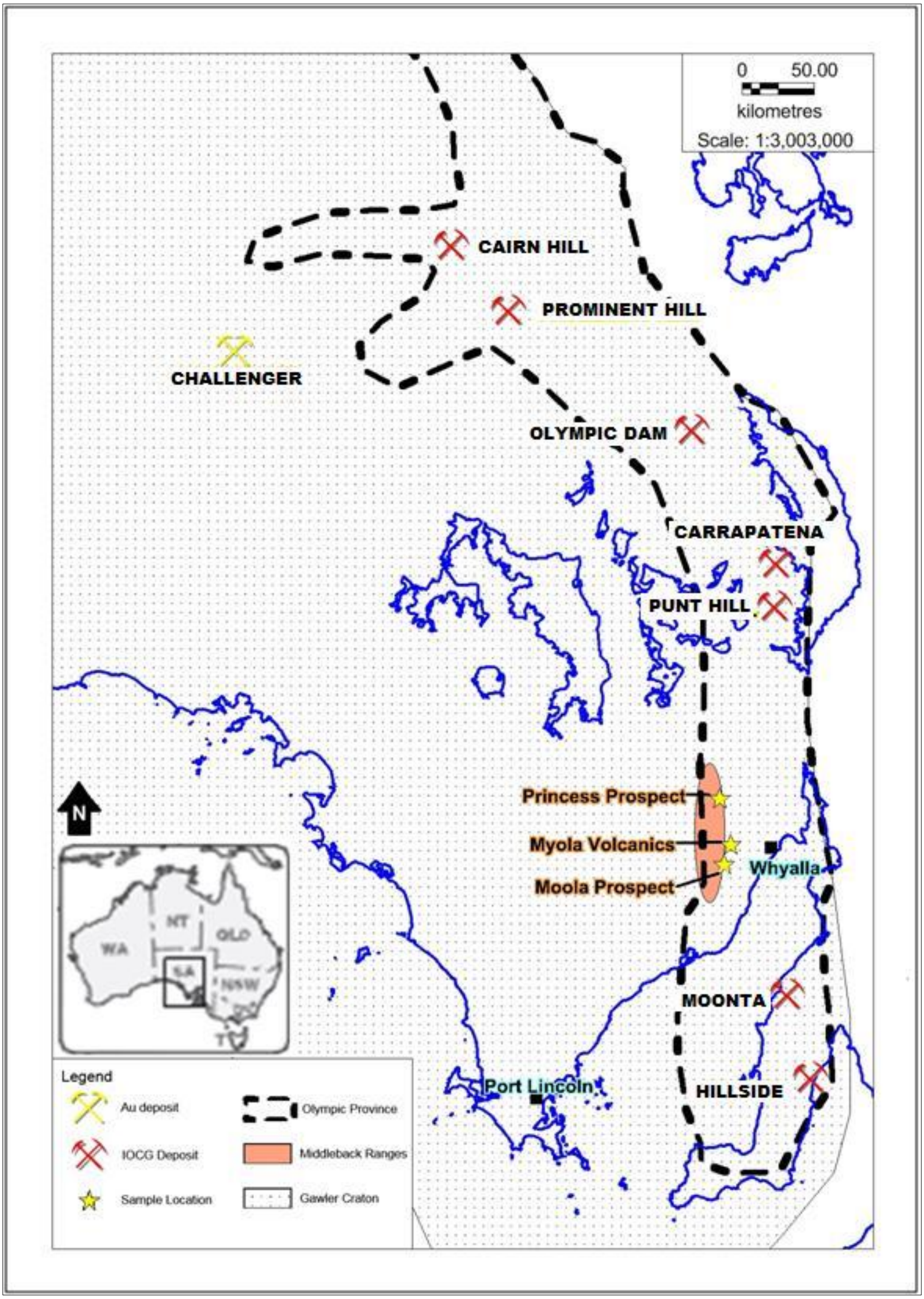

Figure 1 Regional-scale map showing the Middleback Ranges within the Olympic Province. Major IOCG deposits are located.

mainly comprises an assemblage of potassium feldspar-sericite-biotite-quartz in felsic rocks and sericite-chlorite-actinolite±epidote in intermediate to mafic rocks (Hitzman *et al.* 1992). Potassic alteration is also associated with magnetite and silicic alteration, characterised by sericite-carbonate-chlorite±quartz and spatially association with hematite (Hitzman *et al.* 1992). The alteration footprint enclosing mineralisation may be much broader than the deposit itself. An understanding of regional-scale alteration and geochemical/mineralogical variations within the alteration envelope may provide an ore vectoring tool which can be utilised in exploration.

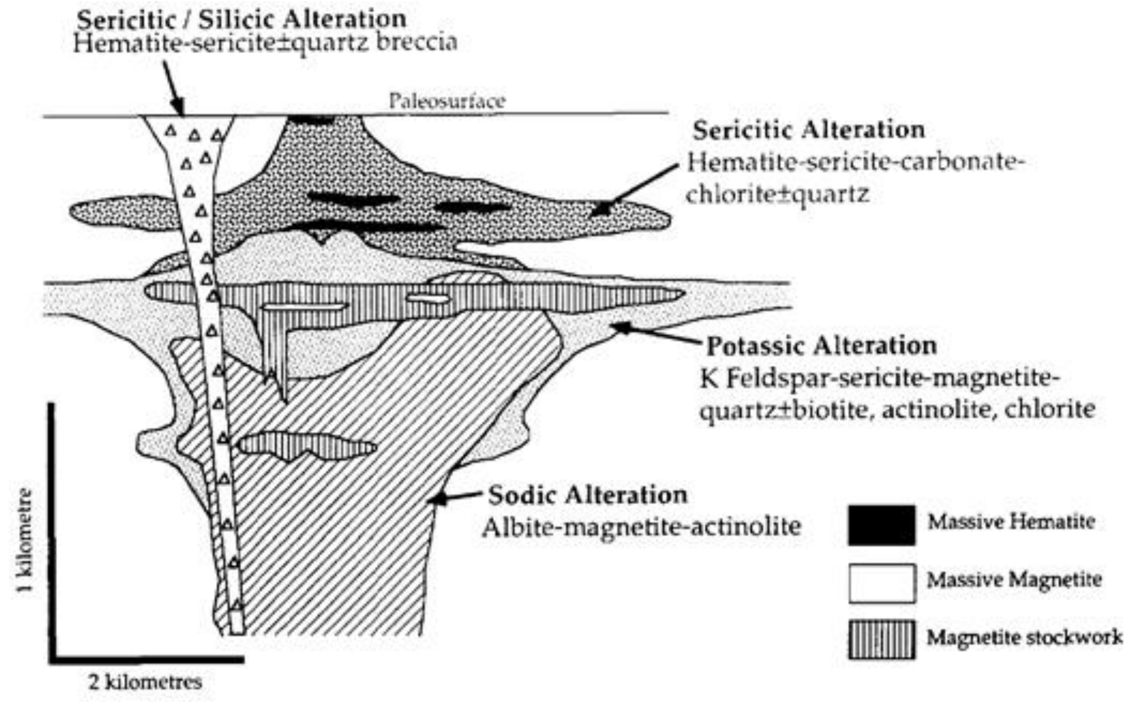

Figure 2 Schematic cross-section illustrating idealised alteration zonation in IOCG deposits (Hitzman *et al.* 1992).

A common characteristic of many/most IOCG systems is the abundance of Rare Earth Elements (REE) (Hitzman *et al.* 1992; Hitzman 2000; Williams *et al.* 2005). The relative abundances of REE vary between co-existing minerals and within individual minerals across a zoned rock package (Ismail *et al.* in press). One possible guide to IOCG-style mineralisation is the regional distribution and variance of REE within

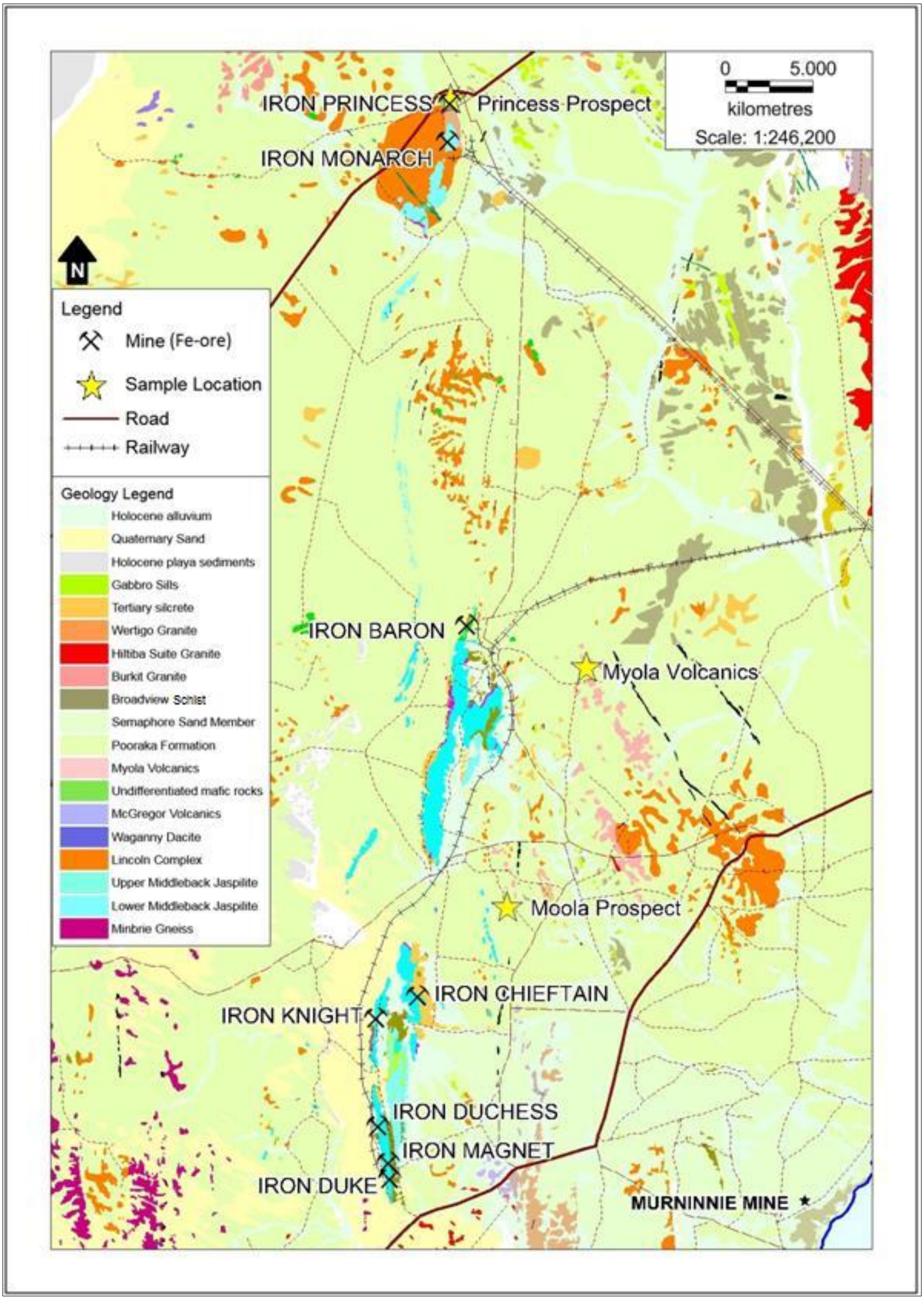

Figure 3 Geological sketch map of the Middleback Ranges, also showing the three sampling localities.

selected minerals (Ismail *et al.* in press). Implementation of this type of exploration tool requires a complete understanding of the REE distribution and partitioning role of all minerals within a mineralising system (Ismail *et al.* in press).

This study contributes to current efforts to define an integrated holistic model for REE distributions in IOCG systems. Two iron-oxide-copper-gold (IOCG) prospective areas in the Middleback Ranges are considered: the Princess Prospect and the Moola Prospect (McIntyre 2001). Samples from the Myola Volcanics type location (Figure 3) are also included, to assist definition of mineralogical-geochemical signatures in unaltered rock. Lithologies within the Princess Prospect drill-core mainly comprise fine-grained chlorite-sericite dominated metasediments whereas drill core from the Moola Prospect is dominated by felsic gneiss, rhyolite and rhyodacite. Mineralisation in both prospect areas has been exclusively observed in drill cores. The Myola Volcanics type location surface hand samples consist of porphyritic rhyolite.

Petrographic, mineralogical and trace element geochemical investigation aims to assess the REE distribution within and between selected minerals, as well as the relationship between mineralisation and alteration in a local and regional context. Iron-Oxide-Copper-Gold (IOCG)-style mineralisation has been proposed as a potential model for Cu-Au deposition in the Middleback Ranges. This paper reports a comparative study of REE distribution and Cu-Au mineralisation/alteration styles in the Middleback Ranges. The intention is to compare these styles with other better-exposed and -documented IOCG deposits in the Olympic Province and elsewhere, and to determine whether regional alteration zonation and the REE geochemical footprint may provide a basis for a vectoring approach in exploration.

BACKGROUND

IOCG mineral systems

Iron oxide-copper-gold (IOCG) systems became accepted as a distinct deposit type (Hitzman *et al.* 1992; Skirrow *et al.* 2002) following discovery of the World-class Olympic Dam IOCG deposit in 1975, and then elsewhere in the World in the following decade. The IOCG classification system encompasses a broad range of deposit styles (Groves *et al.* 2010). These deposits are often found in geologically complex terranes with several different mechanisms for ore formation proposed (Hitzman *et al.* 1992; Hitzman 2000; Williams & Pollard 2002; Williams *et al.* 2005). Deposit morphology is variable and largely influenced by permeability along faults, shear zones and intrusive contacts or by the presence of permeable horizons such as limestone or volcanic tuffs. Both structural and lithological controls are viewed as critical for IOCG deposit generation (Hitzman *et al.* 1992).

Australia has two main IOCG-terranes: the Gawler Craton, SA and the Cloncurry district, QLD (Williams & Pollard 2002; Baker *et al.* 2011). Gawler Craton deposits are characterized by shallow-crustal Cu-Au mineralisation hosted in structurally-controlled hydrothermal breccias with hematite as the dominant Fe-oxide mineral (Hitzman *et al.* 1992; Williams & Pollard 2002). Variable host rocks coincide temporally and spatially with Hiltiba Suite magmatic event (1585±2 Ma) (Johnson & Cross 1995; Skirrow *et al.* 2007).

The most economically significant deposits in South Australia are characterized by hematite-magnetite breccias with strong associations to magmatism; Hiltiba Suite Granites and Gawler Ranges Volcanics (e.g. Olympic Dam and Prominent Hill)

(Williams & Pollard 2002). Other IOCG styles include skarn-like deposits that are high-temperature and broadly coincide with Hiltiba Suite magmatic events (e.g. Hillside and Punt Hill) and ironstone-hosted deposits which predate magmatism and have non-magmatic fluid sources (Baker *et al.* 2011). A consistent pattern of hematite overprinting magnetite is common to the Olympic Dam district; however Haynes (1995) argued that magnetite and hematite formed effectively coevally during multiple overprinting hydrothermal cycles within the Olympic Dam Breccia Complex (Bastrakov *et al.* 2007).

In contrast to the Olympic Province, the Cloncurry district features a diverse range of IOCG deposits. All have magnetite as the dominant Fe-oxide indicating the depth of mineralisation was many kilometres (Hitzman *et al.* 1992; Williams & Pollard 2002). Key features in both terranes that contribute genetically to IOCG formation are the presence of ultra-saline high-temperature fluids, A-type magmatism, association with granites and mafic rocks of age ~1.6 Ga; these characteristics have been linked to supercontinent assembly (Skirrow *et al.* 2007; Groves *et al.* 2010; Baker *et al.* 2011). This process generated two exceptionally saline reservoirs; sequestered giant halite beds and A-type magmas which produce F-, Cl- and CO_2-rich saline fluids (Hitzman *et al.* 1992; Bastrakov *et al.* 2007; Baker *et al.* 2011; McPhie *et al.* 2011)

Regional geology

The Middleback Ranges are located on the south-eastern flank of the Gawler Craton within the Cleve and Moonta Subdomains (Chamalaun & Porath 1967). The Cleve and Moonta Subdomains consist primarily of Archaean to Paleoproterozoic Hutchison Group metasediments (Parker & Fanning 1998; McIntyre 2001; Szpunar *et al.* 2011).

Table 1 Archaean to Paleoproterozoic stratigraphy of north-eastern Eyre Peninsula (Parker 1993).

Age	Stratigraphic unit and symbol	Lithology	Thickness (m)	Comments
PROTEROZOIC / PALAEOPROTEROZOIC	Moonabie Formation (Ꝑmm)	Massive to poorly bedded, pebbly volcaniclastic grit grading into a gritty, often heavy-mineral bedded quartzite away from the volcanic source. Rare siltstone.	400–1000+	The top is not exposed but the base is defined as the top of the uppermost basalt in the McGregor Volcanics.
	McGregor Volcanics (Ꝑmv)	Massive, dark grey, porphyritic to non-porphyritic rhyodacite and rhyolite with minor basalt, dacite and interbedded volcaniclastic grit near top.	1000+	U–Pb zircon age ~1740 Ma.
		unconformity		
	Broadview Schist (Ꝑdb)	Grey slate, phyllite and fine-grained schist with interbedded schistose amphibolite (Ꝑβ) and minor fine-grained, laminated quartzite.		Amphibolites may be original basic sills. Relationships of schist and volcanics not certain.
	Myola Volcanics (Ꝑdm)	Partly recrystallised rhyolite, rhyodacite and fine-grained quartz–feldspar–hornblende gneiss.		The gneiss is interpreted as a recrystallised felsic volcanic. U–Pb zircon age 1791±4 Ma.
		unconformity		
HUTCHISON GROUP (Ꝑh)	Yadnarie Schist (Ꝑhy)	Quartz-veined quartz–feldspar–mica (garnet) schist.	1000+	Top of unit is not known.
MIDDLEBACK SUBGROUP	Upper Middleback Jaspilite (Ꝑhm$_2$) (Mount Shannan Iron Formation)	Banded magnetite quartzite and quartz–grunerite/cummingtonite–magnetite gneiss with minor dolomite bands.	50–200+	Variable magnetite content. Base is locally interbanded with schist. Silicified at surface.
	Cook Gap Schist (Ꝑhc) (Mangalo Schist)	Interbanded pelitic and semipelitic quartz-veined quartz–feldspar–mica (garnet–sillimanite) schist and gneiss. Grades into migmatitic quartz–feldspar–biotite–garnet–sillimanite gneiss.	200–1500+	Variable thickness due to both structural and sedimentary facies changes. Rb–Sr metamorphic age 1688±76 Ma (I.R. = 0.7061).
	(Ꝑβ)	Schistose and porphyroblastic amphibolite.	<150	Locally at base of schist unit but also as sills within. May be intrusive.
	Lower Middleback Jaspilite (Ꝑhm$_1$)	Banded magnetite quartzite, diopside–magnetite quartzite, quartz–grunerite/cummingtonite schist with variable magnetite and talc–magnetite schist. Locally graphitic and/or sulphide-rich near base.	0–500+	Iron content increases from west to east. Silicified at surface. Host to major supergene haematite ores.
	Katunga Dolomite (Ꝑhk)	Massive, white, dolomitic marble with local serpentine and talc after forsterite, diopside and amphibole. Minor calcsilicate layers and local graphite schist.	2–20	Apparent thickness up to 500 m due to folding. Top grades into overlying iron formation.
	Warrow Quartzite (Ꝑhw)	Medium to coarse-grained, massive to flaggy, feldspathic and micaceous quartzite. Pelitic mica schist interbands near top.	<500	Base is frequently intruded by granite and pegmatite sills and dykes.
	(Ꝑhd)	Unnamed dolomitic marble, banded calcsilicate and massive diopside rock.	<20	Developed locally at the base of the Warrow Quartzite.
		unconformity		
	Miltalie Gneiss (AꝐs)	Migmatitic grey granite gneiss with minor amphibolite sills.		Rb–Sr metamorphic age 1697±65 Ma; U–Pb zircon age 2003±18 Ma.
		unconformity		
ARCHAEAN	SLEAFORD COMPLEX	Unnamed quartzo–feldspathic gneiss, garnet gneiss and minor amphibolite.		Rb–Sr age ~2300 Ma. Enclaves within Minbrie Gneiss at Ullabidinie Creek and Minbrie Springs (not differentiated on map).

97-0007

The Hutchison Group was formerly believed to be a single sedimentary succession; it is now thought to consist of three temporally- and isotopically-distinct groups, divided by the crustal-scale Kalinjala Mylonite Zone (Szpunar *et al.* 2011). Deposition of sediments was previously thought to have occurred between 1950 to 1850 Ma

(McIntyre 2001), however zircon analysis by Szpunar *et al.* (2011) has defined deposition to have occurred between 2500 Ma and 1780 Ma.

The Hutchison Group unconformably overlies the Archaean Sleaford Complex which has experienced a complex multiphase deformation, metamorphism and intrusive history (Yeates 1990). Work by Fraser *et al.* (2010) incorporating U-Pb SHRIMP zircon ages and Sm-Nd isotopic techniques identified one of the oldest rock packages in the area, and reported an early Mesoarchaean age (~3150 Ma) for the Cooyerdoo Granite orthogneiss.

The stratigraphy of the Middleback Ranges is well documented (Parker 1993) and is summarized in Table 1. The Sleaford Complex and Hutchison Group are intruded or overlain by granitoid bodies and mafic dykes (Chamalaun & Porath 1967).

Key granitic phases are the Lincoln Complex (~1650 Ma) and the Charleston Granite of Hiltiba Suite age (1585±2 Ma). There are several phases of mafic intrusives emplaced throughout the Paleoproterozoic that are now deformed and altered to amphibolites. The late-stage (700-1000 Ma) doleritic Gairdner Dyke Swarm retains original textures (Parker & Fanning 1998; McIntyre 2001).

The Gawler Craton has experienced three major orogenic events: the Kimban Orogeny (~1730-1690 Ma); the Kararan Orogeny (~1585-1540 Ma); and the Isan Orogeny (~1600-1500 Ma) (Parker 1993; Baker *et al.* 2011). Deformation of the Middleback Ranges is largely attributed to the Kimban Orogeny which caused several fold forming events and the generation of mylonite zones west of the ranges (Parker *et al.* 1988; Yeates 1990). Prograde metamorphism, at up to upper amphibolite facies occurred early during the Kimban Orogeny with localized retrograde metamorphism occurring in later stages of the orogenic event (Yeates 1990). Several major N-S-trending crustal-scale structures crosscut the Middleback Ranges (Parker *et al.* 1988; Parker 1993). These structures are potentially related to splaying off the Kalinjala Shear Zone (KSZ), a major NE-trending mylonite zone that is up to 3 km in width (Parker & Fanning 1998). These structures are associated with several small Cu-Au prospects and historic Cu-Au workings, such as the Murninnie Cu-Bi Mine (see summary in Cave 2010).

IOCG mineralisation in the Middleback Ranges

The Middleback Ranges (Figure 1 & 3) is a historical iron ore mining district with production beginning in 1899 (Yeates 1990). All iron ore deposits of economic significance are situated in the Lower Middleback Formation within the Hutchinson Group (Parker 1993). Economic minerals mined are hematite, magnetite, goethite and limonite (Leevers 2006). The age of iron ore deposits in the Middleback Ranges is poorly understood; a proposed lower age constraint for supergene Fe-ore enrichment within the Iron Duke operations is 1795 Ma to 1745 Ma (Fietz 1989; Leevers 2006). Exploration in the Middleback Ranges has historically focused on iron mineralisation with limited non-ferrous exploration activities. Recent significant Cu-Au-base metal exploration took place in the period 1998-2003 by BHP and Helix Resources and aimed to test areas prospective for IOCG-type mineralisation in BHP's exploration and mining tenements. Potential Cu-Au prospects were identified by analysing historic iron ore drill-hole data, surface geochemistry and previous exploration data (Appendix C) (McIntyre 2001). Research identified two main areas of interest for IOCG-style mineralisation; the Iron Monarch area and Moola Prospect (McIntyre 2001).

Iron Monarch is a structurally-controlled hydrothermal breccia system. Economic iron ore mineralisation has a polymetallic halo and several potential prospects were defined within the Iron Monarch area (Figure 3), including the Princess, Melody, Highway and Monarch SE Prospects. The Moola Prospect (Figure 3) was selected as an area of interest in this study due to the presence of a major north-south structure associated with Cu-Au anomalies in calcrete and drill sample geochemistry, biogeochemistry, geophysical interpretation and proximity to the Charleston Granite (Hiltiba Suite) (McIntyre 2001; Hicks 2010; Mitchell 2010).

The Princess Prospect (Figure 3), a magnetic and gravity anomaly shown to be a pyrrhotite-rich hydrothermal system, was tested by Helix in 2000 with two diamond drill-holes, PRCD1 (381 m; 180m RC pre-collar with 201m diamond core tail) and PRCD1A (510 m; 172m RC pre-collar with 338m diamond core tail). PRCD1 was abandoned at 381 m due to poor ground conditions and a re-drill, PRCD1A was completed. Assay results showed anomalous Cu-Co-Ag-Au-As intercepts throughout the drill holes (McIntyre 2001). Hydrothermal alteration was observed below 356 m, consisting of magnetite, hematite, silica and carbonate alteration. Pyrite, pyrrhotite and epithermal-style barite, siderite and calcite veining was observed throughout the hole. The alteration, textures and geochemistry indicate that a large hydrothermal system was active in the area (McIntyre 2001). No petrographic analysis had, however, been conducted on this core prior to the present study.

A single diamond drill-hole, ML001DD, was completed at the Moola Prospect (Figure 3) in November 2009 by OneSteel (now Arrium Mining) to test Cu-Au mineralisation. Studies on the drill-core revealed Cu-Au mineralisation hosted within altered Myola Volcanics. Mineralisation is characterized by pyrite ± chalcopyrite, with both hematite and magnetite recognised (malachite and native copper are also recognised in the weathered zones). Four alteration styles were identified: sodic alteration characterized by the formation of albite; sericitic alteration; chloritic alteration; and late-stage quartz, quartz-carbonate and carbonate flooding which hosts sulphide mineralisation (Cave 2010). Although follow-up RC drilling by Arrium Mining in 2012 (Project Mawson) did not discover significant mineralisation, the Moola Prospect remains an attractive exploration target.

Cave (2010) interpreted the Moola Prospect as an epigenetic hypothermal Cu-Au system with affinities to other IOCG deposits on the Gawler Craton. Neodymium isotopes and Co:Ni ratios of pyrite indicate metals were derived from the crust with a minor mantle input. Sulphur isotopes and trace element whole-rock geochemistry indicate a primitive magmatic fluid source is responsible for alteration and metal transport (Cave 2010).

METHODS

The sample suite from three locations in and proximal to the Middleback Ranges included 2 hand-samples from the Myola Volcanics type location, 16 from the Iron Princess diamond drill core (hole ID: PRCD1A), and 17 from the Moola diamond drill core (hole ID: ML001DD). A total of 35 thin-sections were prepared by Pontifex and Associates for petrographic examination. Preliminary characterisation of the mineral assemblages was conducted using both transmitted and reflected-light optical microscopy and Scanning Electron Microscopy (SEM) and was aimed at documenting size, texture, zonation and relationships between Fe-oxides, feldspars, sulphides and accessory and alteration minerals. The EDS system fitted to the SEM also provided qualitative compositional data.

Analysis of the trace element distribution within specific minerals was conducted by Laser-Ablation Inductively-Coupled Mass Spectroscopy (LA-ICP-MS), supported by Electron Probe Microanalysis (EPMA). Minerals targeted were hematite, magnetite, ilmenite, titanite, microcline, perthite, sericite, chlorite, apatite, rutile, monazite, zircon, hornblende, kutnohorite, calcite and pyrite. LA-ICP-MS was also used to map the elemental composition of selected compositionally-zoned minerals. Full details of analytical methodology, including analytical operating conditions and calibration routines, are given as Appendix A. LA-ICP-MS trace element data was normalised to chondrite using values from McDonough & Sun (1995). Estimations of mineralisation temperature were afforded by chlorite geothermometry using the calibrations of Cathelineau (1988) and Jowett (1991), and by Zr-in-rutile geothermometry using equations given by Watson *et al.* (2006)

RESULTS

Petrography - Lithology

MYOLA VOLCANICS

Rhyolite porphyry

The Myola Volcanics rhyolite has a porphyritic-texture with porphyryblasts of inter-grown microcline and albite (15%) within a fine-grained felsic matrix (75%). A weak gneissic fabric, defined by Fe-oxide stringers, chlorite, sericite, biotite and elongated zones of feldspar (10%) (Figures 4a & 5a).

The feldspar phenocrysts are medium- to coarse-grained (<1 mm) and show some deformation. There are some sulphides associated with the Fe-oxide and biotite stringers. Pseudomorphic replacement of magnetite by hematite (martitisation) is common throughout and is of varying intensity (Figure 9); fresh magnetite and late-stage pyrolusite are also present (Figure 6d).

Zircon is present (Figure 6b), associated with chlorite rich zones, as is minor, fine-grained (<30μm) apatite (Figure 6j). Rutile is associated with titanite, Fe-oxides, zircon, rare monazite and xenotime. Late-stage calcite was observed.

MAWSON PROSPECT

Felsic breccia

The breccia zone lies within grey-pink fine-grained siliceous banded felsic gneiss. The felsic breccia contains 40% transported, coarse-grained pink granitic clasts, 30% locally sourced fine-grained pink/grey felsic gneiss clasts and 20% dark grey fine- to medium-grained infill. Infill is defined by fine-grained rock flour, chlorite, kutnohorite (late-stage Mn influx), quartz and biotite (Figure 4b).

Microcline is the dominant feldspar, with albite and perthite also present. Muscovite is present as coarse-grains or as fine-grained sericite alteration (in particular of feldspars). Chlorite is very fine-grained and occurs predominantly in the breccia infill (Figure 5b) and altering feldspars.

There are two main varieties of Fe-oxides; a pervasive Ti-rich hematite that occurs in gneissic clasts (Figure 7e), and a fine-grained bladed Ti-poor hematite seen as a late-stage infill mineral.

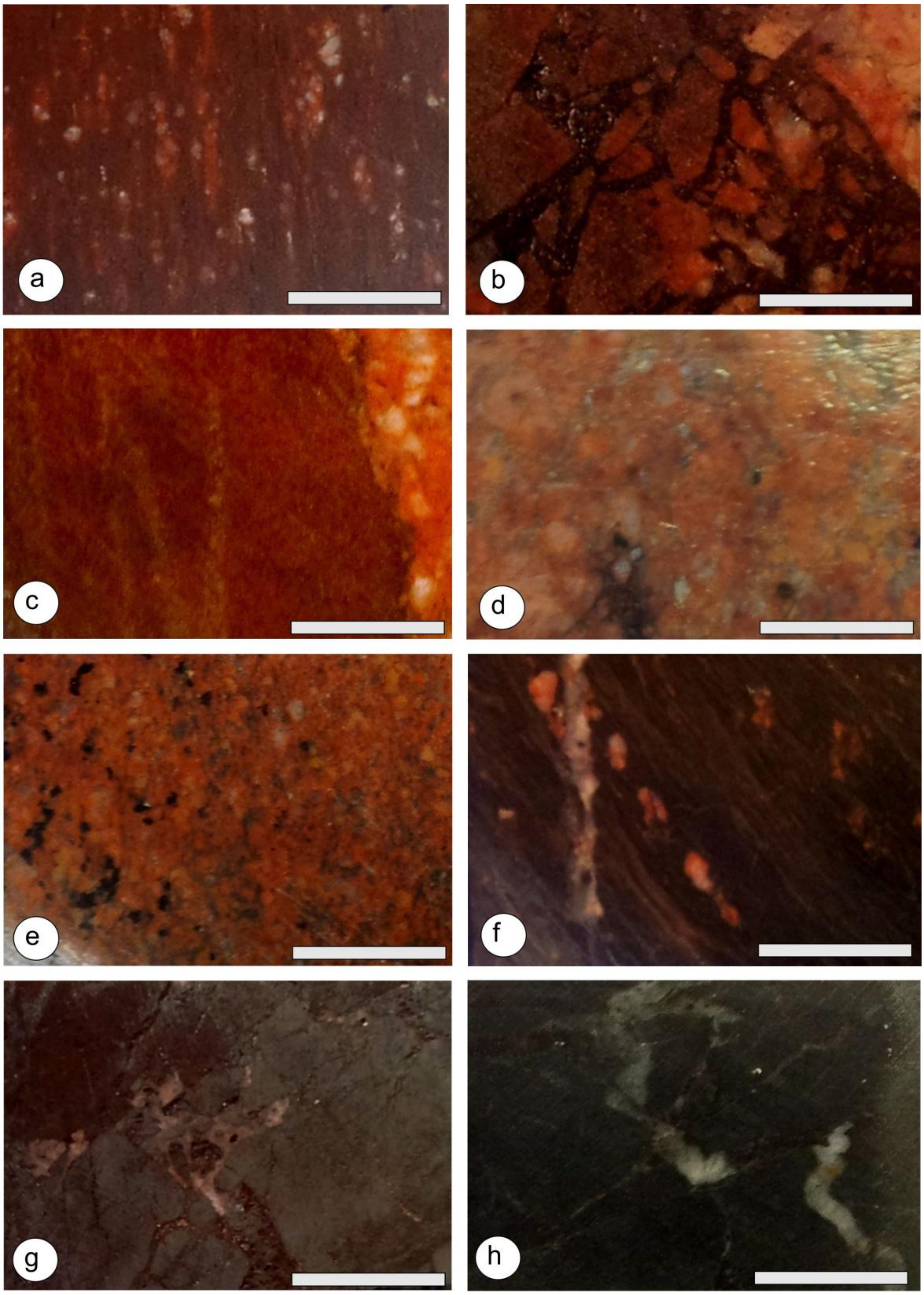

Figure 4 (a-h) Photographs of hand-specimens of typical lithologies (scale-bars: 1 cm). (a) Myola Volcanics porphyry rhyolite (sample: MV01); (b) Felsic breccia (sample: ML01); (c) Banded felsic gneiss; granitic veinlet is seen on the RHS of image (sample: ML02); (d) Granite veinlet (sample: ML06); (e) Granite (sample: ML07); (f) Flow banded rhyolite-dacite volcaniclastic (sample: ML15); (g) Hematite breccia (sample: PS01); (h) Metasedimentary rock (sample: PS03).

Accessory minerals observed include rutile, monazite, zircon and apatite. Monazite is typically very fine-grained (<20 µm) and often associated with zones of increased chlorite and sericite content. Zircon is only found in granitic clasts.

Banded felsic gneiss

The felsic banded gneiss is very fine-grained and displays mm- to cm-scale compositional banding (Figures 4c & 5c). Microcline is the dominant feldspar; feldspars are heavily altered by sericite. Hornblende is very minor, and where observed, has a corroded texture and is largely replaced by chlorite (similar to that seen in Figure 5d).

Titaniferous hematite, the dominant Fe-oxide, contains oriented, cooling related exsolution lamellae of ilmenite.

Accessory minerals found disseminated throughout the rock include apatite, monazite (<20 µm) and fine-grained zoned zircon (Figure 5b). Rutile was associated with ilmenite and was mainly observed at contacts between banded felsic gneiss and granite veinlet (Figures 5g & 5h). Very fine-grained xenotime occurs within carbonate veins, or included within Fe-oxides.

Pink granite veinlet

The pink medium- to coarse-grained granite is observed as veinlets intruding fine-grained felsic gneiss parallel to gneissic fabric (Figures 4d & 5d). The texture of the granite veinlets varies from granoblastic to having a slight fabric defined by augen shaped microcline and aligned micas.

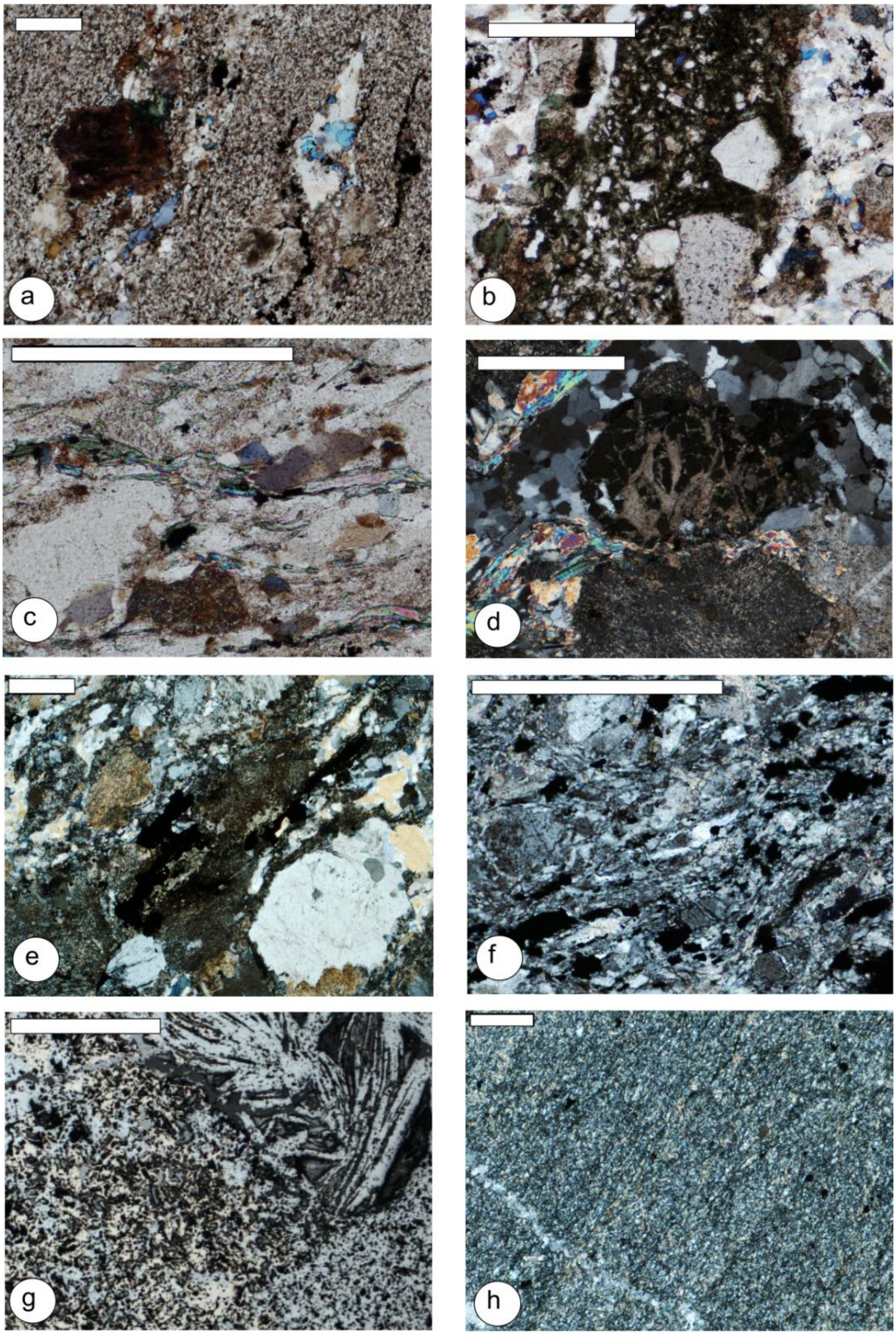

Figure 5 (a-h) Petrographic images of typical lithologies; all transmitted cross polarised light images except g) (reflected light cross polars). (a) Myola Volcanics porphyry rhyolite (sample: MV01), Microcline porphyryblast within a fine grained matrix comprised of quartz, feldspar and sericite. Chlorite, sericite and rutile are associated with feldspars. Fabric is defined by elongated zones of coarse-grain minerals and martite stringers (opaque mineral). (b) Felsic breccia (sample: ML01); Chlorite dominated breccia infill. RHS of image is a clast of granite composed of quartz, altered feldspars and minor zircon. (c) Banded felsic gneiss (sample: ML02); Fabric is defined by

coarse-grain chlorite and sericite. Rock is dominated by quartz and altered feldspars. (d) Granite veinlet (sample: ML06); Central mineral is heavily chlorite altered hornblende surrounded by quartz, muscovite and altered feldspars. (e) Granite (sample: ML07); Granite is dominated by quartz, heavily altered microcline, plagioclase, chlorite, sericite and titaniferous hematite. Opaque mineral in centre of image is chalcopyrite. (f) Flow banded rhyolite-dacite volcaniclastic (sample: ML15); Fine grained volcaniclastic is dominated by quartz, feldspar, muscovite, titaniferous hematite and ilmenite. (g) Hematite breccia (sample: PS01); Bladed hematite (fine- and coarse-grained in infill and clasts respectively) dominates the breccia. (h) Metasedimentary rock (sample: PS03); The very fine-grained rock is dominated by quartz, chlorite and sericite with minor kutnohorite and quartz-carbonate crackle veins. Scale bar: 500 µm.

Late-stage Ti-rich hematite is associated with rutile and has ilmenite exsolution lamellae (Figure 5e & f). Some iron oxides are conspicuously Ba-rich and are tentatively identified as the rare mineral barioferrite ($BaFe^{3+}_{12}O_{19}$). If confirmed by X-ray diffraction, this would represent a second World occurrence of barioferrite, previously reported only from the type locality in Israel (Appendix G) (Murashko *et al.* 2011). The synthetic analogue of barioferrite is, however, the main industrial ferromagnetic material.

Microcline is the dominant feldspar and shows polysynthetic twinning (Figure 7f); perthite is also present. Feldspars show sericite alteration. Kutnohorite is present in 2D as diamond-shaped crystals associated with areas rich in quartz, chlorite and sericite. Accessory minerals include rutile, apatite, monazite, uraninite, xenotime and zircon. Multiple generations of rutile are recognised from their different textures; euhedral coarse-grained rutile is associated with Ti-rich Fe-oxides and chlorite rich zones. Apatite is sparsely disseminated and fractured crystals are associated with sericite-rich veins. Monazite is concentrated near rhodochrosite, zircon and kutnohorite. Late-stage calcite veins are observed (Figure 7c).

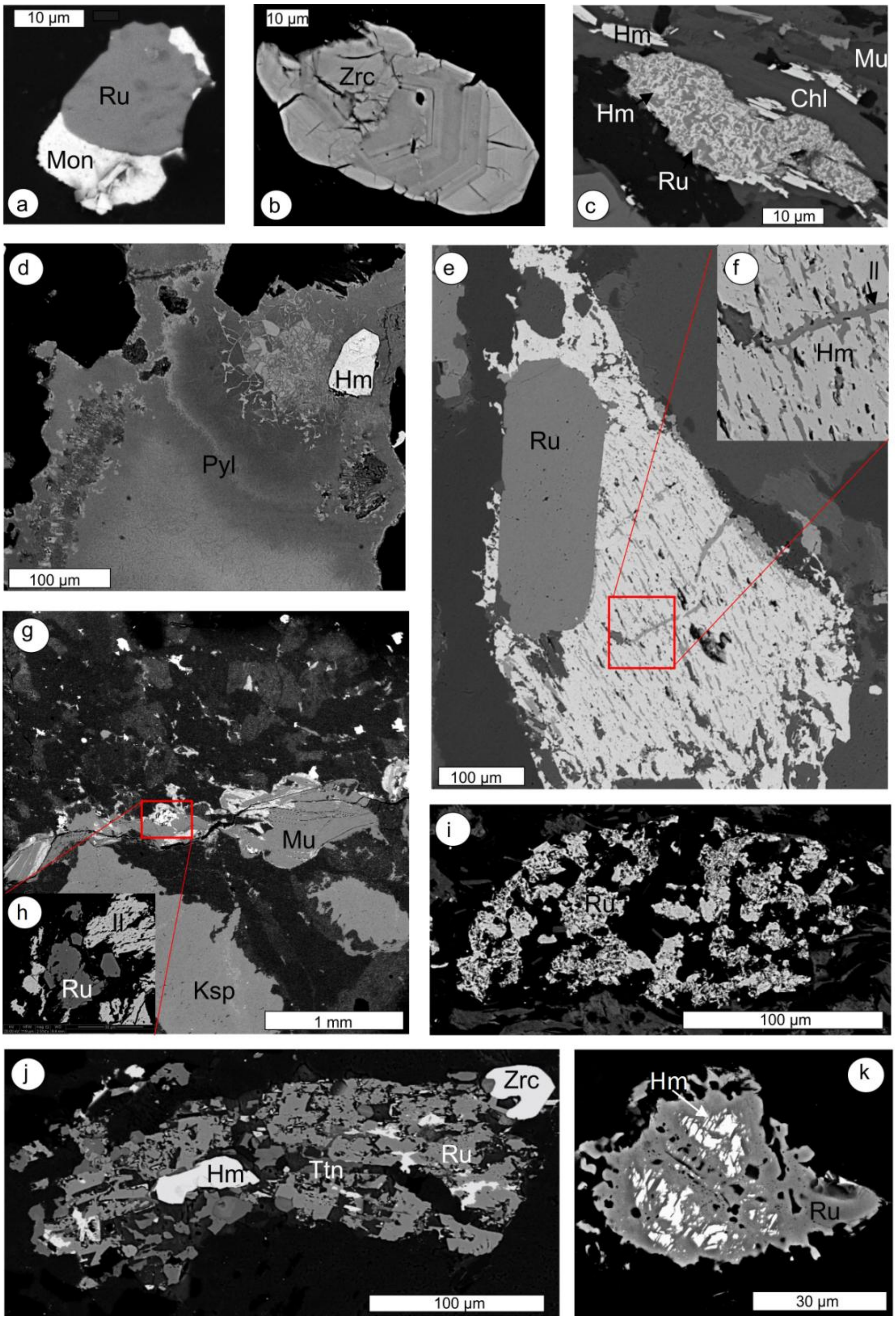

Figure 6 (a-k) Back-scatter electron images showing accessory minerals. a) Equigranular rutile (Ru) associated with monazite (Mon) from the Princess Prospect metasediments; rutile is potentially hydrothermal (sample ID: PS06). b) Zoned and broken zircon (Zrc) is common throughout the sample suite (sample ID: ML04 - felsic banded gneiss). c) The felsic volcaniclastic rock has symplectic rutile (darker grey) and hematite (Hm) (brighter grey) after ilmenite (Il). Bladed Ti-poor hematite is also observed in this image (brightest mineral) (sample ID: ML14). (d)

Myola Volcanics – late-stage pyrolusite (Pyl); zonation is apparent in image however analysis showed no obvious chemical variation (sample ID: MV01). e) & f)) Granitic veinlet - hematite with ilmenite exsolution lamellae is associated with a homogenous course grained rutile. Inset f) is a close up of exsolution textures (sample ID: ML03). g) & h) The contact between felsic banded gneiss and granitic veinlet commonly has rutile and ilmenite; inset h) Rutile and ilmenite close up (sample ID: ML04). i) This rutile from the Princess Prospect metasediments may represent a corroded detrital grain (sample ID: PS06). j) Rutile in the Myola Volcanics is often associated with titanite (Ttn) and Fe-oxides (sample ID: MV01). k) The rutile in the felsic volcaniclastic rock is observed to replace Fe-oxides (sample ID: ML17).

Hybrid zone

The hybrid zone consists of intercalated pink siliceous banded felsic gneiss and medium- to coarse-grained granite with moderate fabric intensity. Microcline is the dominant feldspar and both microcline and albite showed significant sericite alteration. Chloritisation and potassic alteration are also observed.

Iron oxides are associated with apatite and rutile; titaniferous hematite is the main Fe-oxide. Late-stage kutnohorite and ankerite is present within fractures and voids.

Granite

The granite is medium- to coarse-grained, dark-pink to grey-pink and equigranular (Figures 4e & 5e). Zones of brecciation, intense sericite alteration and potassic alteration are observed. An intensely silicified breccia zone at the contact between the granite and the felsic volcaniclastic rock displays unique sulphide mineralogy. Potassic alteration is mainly associated with quartz veining.

Titaniferous hematite is associated with chlorite and Mn-oxides. Late-stage goethite/limonite, pyrolusite and minor delafossite is observed.

Microcline is the dominant feldspar with some albite and Na rich perthite. Quartz, muscovite, chlorite and biotite make up the rest of the rock. Carbonates present, ankerite, kutnohorite and calcite were distinguished using EDS analysis.

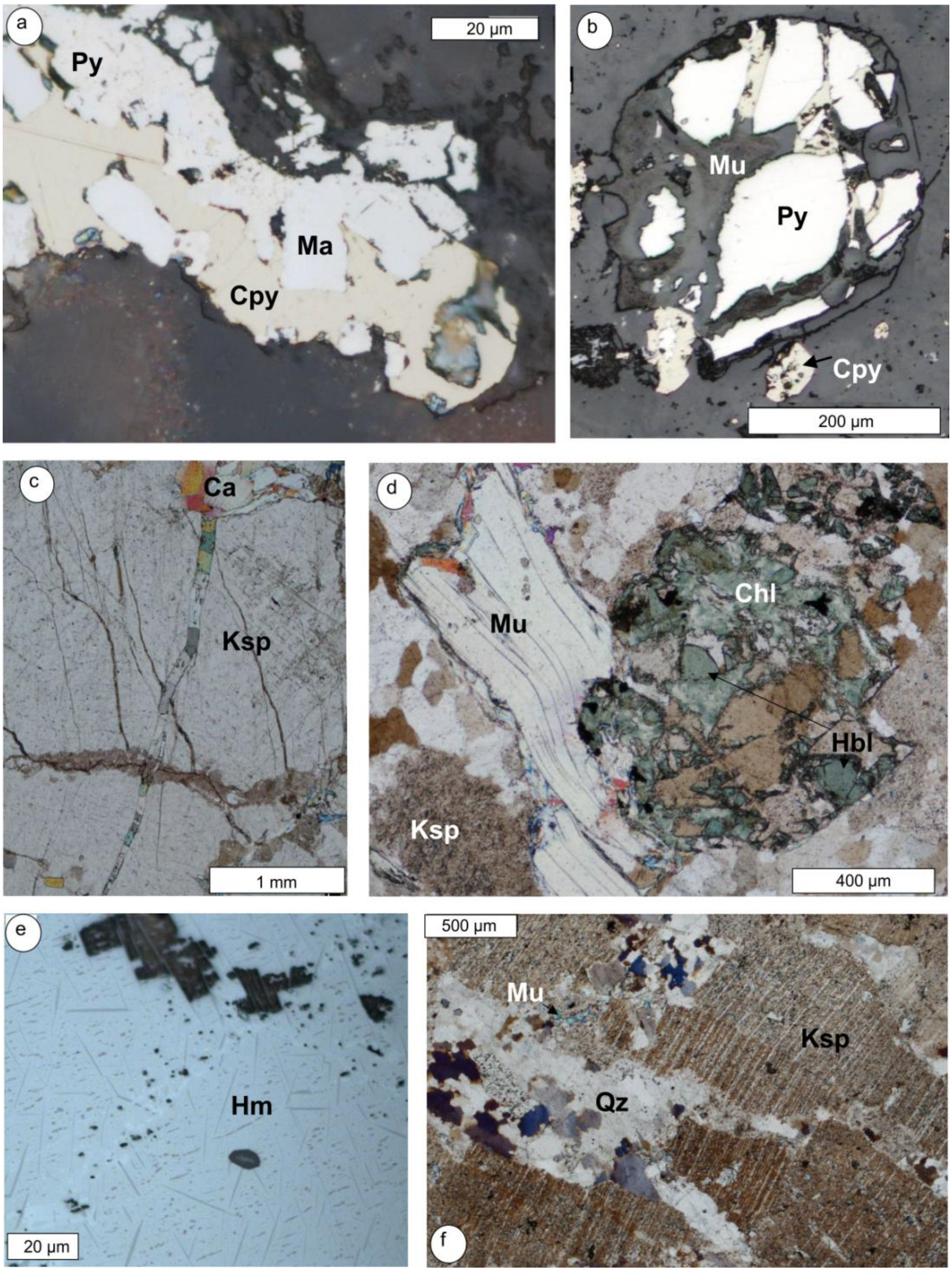

Figure 7 (a-f) Petrographic images – (a, b & e) reflected light, plane polars light; (c, d & f) transmitted light, cross polars light. All images are from the Moola Prospect. a) This image from the hybrid zone shows pyrite (Py) and marcasite (Ma) with late-stage chalcopyrite (Cpy) (sample ID: ML15). b) Corroded pyrite with late-stage chalcopyrite was observed within a quartz-carbonate vein in the granitic veinlet; fine-grain sphalerite was also observed within the vein (sample ID: ML03). c) Late-stage carbonate vein within the granitic veinlet (sample ID: ML04). d) Hornblende (Hbl) is commonly altered to chlorite (Chl); feldspars are often altered by chlorite and sericite. Muscovite (Mu) can be both coarse- and fine-grained (sample ID: ML04). e) Titaniferous hematite (Hm) showing ilmenite exsollution lamellae (<1 μm across and ~10 μm long) (sample ID: ML01). f) Simple twinning of microcline (Ksp) with sericite (Mu) alteration within granitic clast in felsic breccia (sample ID: ML01).

Accessory minerals include zircon, zoned apatite, fine-grained monazite, barite, native bismuth and copper (Figure 8i) and late-stage uraninite associated with kutnohorite.

Felsic volcaniclastic

The rhyodacite is a moderately-foliated, weakly-magnetic, dark-grey fine-grained felsic volcanic rock (Figures 4f & 5f). The rock is rich in feldspar, chlorite and sericite and displays mm-scale banding with alternating pink, K-Si-rich bands and green-grey chlorite and Fe-oxide rich bands. Microcline is the dominant feldspar with some albite and perthite present. Weak to moderate carbonate alteration is commonly observed with some quartz and carbonate crackle veins.

Iron oxides, in particular bladed titaniferous hematite, are ubiquitous throughout the samples. Rutile and hematite symplectites after ilmenite are present (Figure 6c). Late-stage zoned kutnohorite is seen in the matrix as diamond-shaped crystals and within fractures and veins.

Rutile is found throughout and displays varying textures. It is sometimes coarse-grained, fractured and associated with hematite and late-stage ilmenite (Figure 11). In some instances the rutile is observed to replace Fe-oxides (Figure 6k). Other fine-grained rutile, with a characteristic corroded texture, is found disseminated throughout the samples. Some apatite grains within the main matrix are compositionally zoned from core to rim but are generally too fine-grained (<30 µm) to permit identification of the element concentration expressing this change. Zircon displays fracturing and compositional zoning.

IRON PRINCESS PPROSPECT

Fe-dominated breccia

The breccia is hematite-dominant with minor magnetite; hand samples are weakly magnetic. Breccia clasts are massive, very fine-grained and have a blue metallic-lustre and red streak. Infill is composed of soft, medium-grained hematite with a feathered platy texture (Figures 4g & 5g). Quartz is seen as infill, growing into vughs and as crackle veins. There are multiple phases of Fe- minerals (siderite, magnetite and colloform goethite) with late-stage magnetite rims on hematite (Figure 8f). Bladed goethite is seen to pseudomorph pyrite. Accessories include monazite and barite.

Table 2 Petrographic summary of main lithologies.

Lithology	Mineralogy	Sulphides	Veining
MYOLA VOLCANICS			
Myola Volcanics ***MV01 & MV02.***	65% fine grained felsic matrix (chlorite, sericite, quartz); plagioclase 10%; microcline 10%; martite/magnetite 5%; biotite 5% & quartz 5%.	Trace sulphides are associated with martite.	Minor quartz veins.
MOOLA PROSPECT			
Banded Felsic Gneiss ***ML02, ML04***	30% rounded coarse grained quartz crystals, 29% microcline, 10% fine to medium grained platy muscovite, 10% very fine grained yellow platy sericite, 10% plagioclase, 5% biotite, 5% chlorite & 1% hornblende.		Calcite veins.
Granite Veinlet ***ML03, ML06*** *ML02*	45% quartz, 15% microcline 10% albite, 10% muscovite, 10% chlorite, 5% biotite & 5% magnetite.	Chalcopyrite, pyrite & sphalerite.	Discontinuous clotty quartz veins. Calcite veins.
Hybrid Zone ***ML05***	30% microcline, 30% quartz; 20% plagioclase 10% muscovite; 10% biotite & <1% iron oxide.	Pyrite, chalcopyrite & marcasite.	Late-stage quartz veining.
Granite ***ML07-ML12***	40% microcline, 20% plagioclase, 20% quartz, 10% muscovite, 5% biotite & 5% amphibole.	Pyrite, chalcopyrite, sphalerite & marcasite.	Quartz and carbonate veins associated with sulphides.
Felsic Volcaniclastic ***ML13-ML17***	65% fine grained felsic matrix (chlorite, sericite, quartz); plagioclase 10%; microcline 10%; magnetite/hematite 5%; biotite 5% & quartz 5%.	(ML13 cpy, py, covellite, chalcocite, bornite) Disseminated chalcopyrite and pyrite	Quartz and carbonate veins.
PRINCESS PROSPECT			
Fe Dominated Breccia ***PS01 & PS02.***	75-85% hematite; 10-15% magnetite; 10% quartz.		Minor quartz crackle veins.
Metasediment ***PS03-PS16***	35% chlorite; 30% sericite; 20% quartz; 5% biotite; 5% iron oxides & 5% kutnohorite/jacobsite/rhodochrosite.	Chalcopyrite, pyrite & pyrrhotite.	Quartz veins, some quartz carbonate crackle veins.

Metasedimentary rocks

The metasedimentary rocks are very fine-grained, massive, dark green-grey in colour and dominated by chlorite and sericite (Figures 4h & 5h). There are zones of minor brecciation, ductile deformation, weak fracturing and also potential flow-banding. A slight foliation is defined by aligned micas and is sometime seen crosscutting itself. Some sericite alteration is associated with vughs, sparry quartz and carbonate crystals with trace sulphides. Rhodochrosite and late-stage, F-enriched kutnohorite are seen growing in quartz veins and vughs. Quartz-calcite crackle vein are present and are associated with increased sericite alteration.

Apatite, rutile, zircon and minor fine-grained monazite are disseminated throughout the samples. Rutile is sparse; zones (~100 μm) of fine-grained feathery rutile may represent a corroded pre-existing detrital grain (Figure 6i) and equigranular rutile (potentially hydrothermal) is associated with late-stage monazite (Figure 6a). Zircons are compositionally-zoned with highly variable trace element concentrations. These are quite often broken and, in part, also metamict in character. They are probably detrital in origin although a hydrothermal overprint cannot be ruled out. Minor uraninite is associated with vughs.

Sulphide petrography

MYOLA VOLCANICS

Trace sulphides (chalcopyrite and pyrite) are associated with martite-rich stringers.

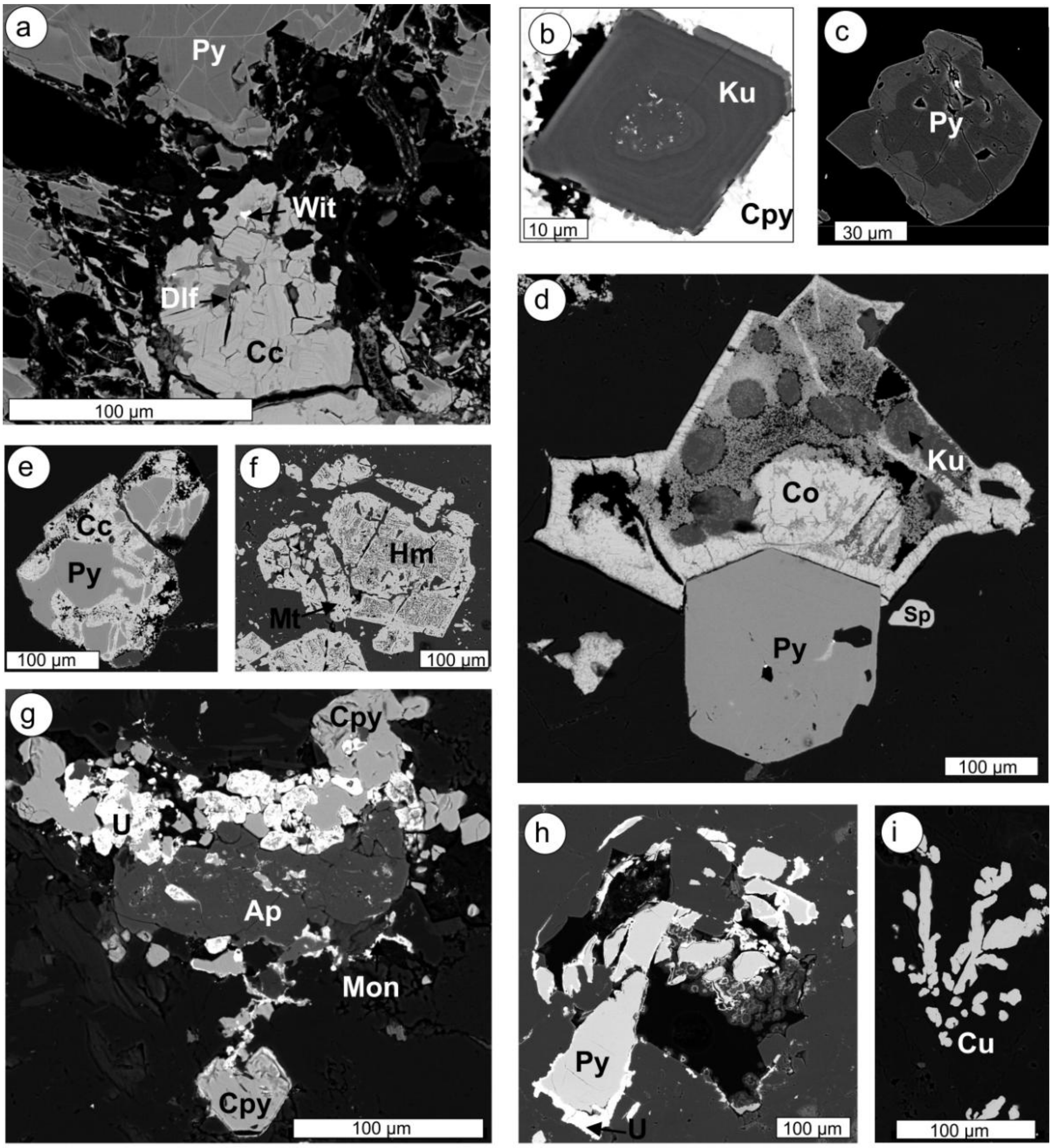

Figure 8 (a-i) Back-scatter electron images of Fe-oxides and sulphides; all images are from within the silicic breccia at the contact between the granite and felsic volcaniclastic in the Moola Prospect except for c), f), g) & h). a) Early pyrite (Py) has chalcocite (Cc) along fractures. Massive chalcocite is associated with wittichenite (Wit) and has late-stage delafossite (Dlf) (sample ID: ML13). b) Kutnohorite (Ku) is zoned with respect to Mn; coeval growth is supported by Cu-sulphate (?) inclusions within the core of the kutnohorite grain. (sample ID: ML13). c) Pyrite within the Princess Prospect metasedimentary rocks is zoned with respect to As (sample ID: PS12). d) Early pyrite is proximal to minor sphalerite (Sp); covellite (Co) is observed growing into the void, and late-stage Kutnohorite and Cu-sulphates are forming within voids. Relationships in b) and d) may support a relationship between late-stage remobilisation of Cu and Mn (sample ID: ML13). e) Chalcocite replacing pyrite (sample ID: ML13). f) Hematite breccia: Princess Prospect. Bladed hematite (Hm) is rimmed by a late-stage magnetite (Mt) that has elevated REY in comparison to the Hm (sample ID: PS02). g) Moola Prospect: granite. Late-stage uraninite (U) and monazite (Mon) is commonly closely associated with chalcopyrite and apatite (Ap) and is proximal to kutnohorite veins (sample ID: ML10). h) Moola Prospect: granite veinlet. Corroded pyrite is rimmed by late-stage uraninite (sample ID: ML03). i) Native dendtritic copper (sample ID: ML13).

MOOLA PROSPECT

No sulphides are documented in the felsic breccia or the banded felsic gneiss. The granite veinlet hosts chalcopyrite, pyrite and associated minor sphalerite within discontinuous clotty quartz veins. Pyrite is seen to be fractured, corroded, and associated with sericite (Figure 7b). Corroded pyrite is often rimmed; in some instances by chalcopyrite and in others with fine-grained uraninite (Figures 7b & 8h). Chalcopyrite is observed in fractures adjacent to the granite veinlets. The granite veinlet/felsic gneiss hybrid zone hosts patches of pyrite, marcasite and chalcopyrite (Figure 7a).

In the granite, intergrown chalcopyrite, apatite, uraninite and monazite are often seen as discontinuous patches or hosted within kutnohorite-bearing veins (Figure 8g). Chalcopyrite, pyrite, marcasite and sphalerite are disseminated throughout the felsic volcaniclastic rocks and found within and adjacent to quartz veins. Sulphides are seen in vughs and also associated with potassic alteration. Chalcopyrite infill and may represent a late-stage, potentially remobilised, generation of mineralisation.

The siliceous breccia at the granite/felsic volcaniclastic contact hosts multiple generations of sulphides displaying a range of textures. Both bladed and euhedral pyrite is observed. Chalcopyrite is seen after bornite. Homogenous coarse-grained chalcocite is observed to replace chalcopyrite. Chalcocite is found within fractures in pyrite and is commonly associated with wittichenite (Figure 8a). Chalcocite replaces pyrite (Figure 8e) and is associated with sphalerite, digenite and emplectite. Covellite is observed growing into voids is associated with zoned coarse-grained diamond-shaped kutnohorite and has later-stage fine-grained inter-grown Cu-(Fe)-sulphates (Figure 8d).

The kutnohorite is zoned with respect to Mn content and the distribution of Cu-sulphide inclusions (Figure 8.b). Late-stage delafossite is associated with chalcocite (Figure 8a). Dendritic native copper is present (Figure 8i).

Pyrite → Bornite → chalcopyrite → chalcocite → covellite/wittichenite → Kutnohorite/a secondary (hydrated) Cu-(Fe)-sulphate.

The felsic volcaniclastic contains ubiquitous though sparse disseminations of fine-grained sulphides (predominantly chalcopyrite).

PRINCESS PROSPECT:

No sulphides were documented in the Fe-dominated breccia.
Within the metasedimentary rocks disseminated sulphides are associated with quartz veins and silica flooding and Mn minerals (kutnohorite and jacobsite (?)); chalcopyrite is the most abundant and is associated with both pyrite and pyrrhotite. Chalcopyrite is sometimes associated with minor xenotime. Compositional zoning, expressed as concentric zones with different As contents, is observed in pyrite (Figure 8c). Minor galena, sphalerite and bornite were observed.

Laser-Ablation Inductively-Coupled-Plasma Mass-Spectrometry (LA-ICP-MS)

REE DISTRIBUTION

When characterising REE concentrations, Y has been included in the tables and figures, positioned between Dy and Ho on the chondrite-normalised fractionation trends following practise elsewhere (e.g. Bau 1996). ΣREY is defined as the sum of measured

La+Ce+Pr+Nd+Sm+Eu+Gd+Tb+Dy+Y+Ho+Er+Tm+Yb+Lu. Normalization to chondrite follows McDonough and Sun (1995).

Fe-oxide & ilmenite

Samples from the Myola Volcanics show 3 phases of Fe-oxides; fresh unaltered magnetite, magnetite associated with martite and martite. Fresh unaltered magnetite is low in REY; the chondrite-normalised plot shows a slight depletion of LREE with strong negative Cs- and Y-anomalies. Magnetite associated with martite displays a slight increase of HREE. The degree of martitisation correlates with enrichment of REE; in particular LREE and has strong negative Cs- and Eu-anomalies (Figure 9 & Table 3). No ilmenite was analysed.

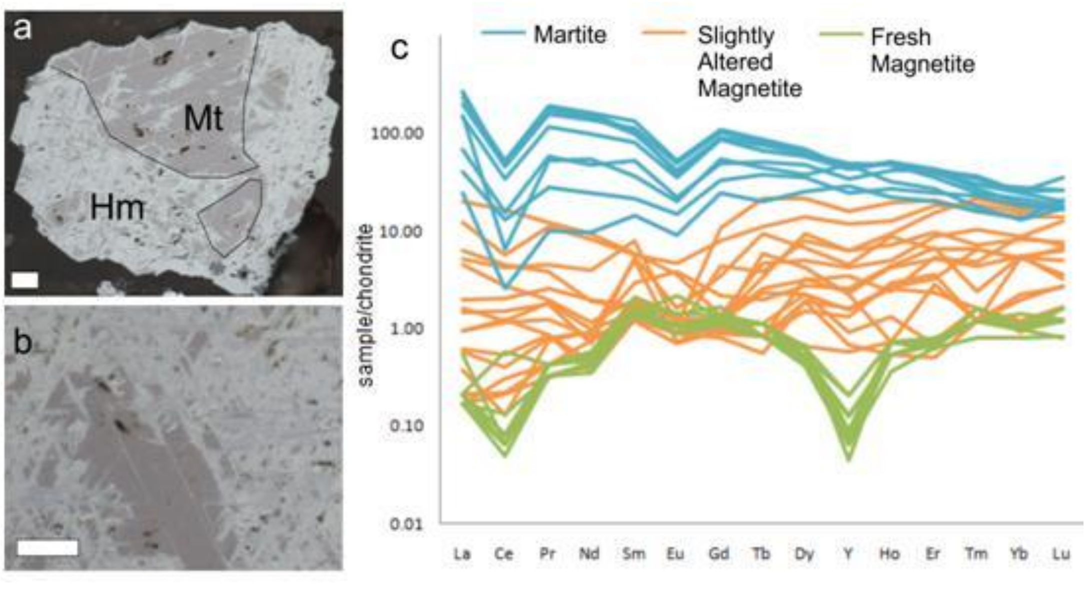

Figure 9 (a & b) Reflected light images in plane polarised light; martite texture – hematite (Hm) replacing magnetite (Mt). This feature is predominant in the Myola Volcanics. c) Chondrite-normalised REY fractionation trends for fresh magnetite, slightly altered magnetite and martite show the degree of martitisation is associated with REE enrichment.

The titaniferous hematite analysed in the Moola Prospect samples are low in REY and show quite variable patterns in the REY chondrite-normalised plot (Figure 10 & Table 3). The felsic gneiss and hybrid zone titaniferous hematite have the lowest REY; both have quite a flat chondrite-normalised plot distribution with the felsic gneiss showing slight LREE enrichment. There was a slight HREE enrichment in the foliated rhyodacite (sample ML14) with the flow banded rhyolite having the highest titaniferous hematite (sample ML16) REY concentrations of varying distribution.

Ilmenite was analysed in 2 Moola Prospect felsic volcaniclastic samples; ML14 has fine-grained disseminated ilmenite and ML16 has late-stage ilmenite (containing unknown inclusions) associated with a coarse rutile grain (Figure 11 & Table 3). The

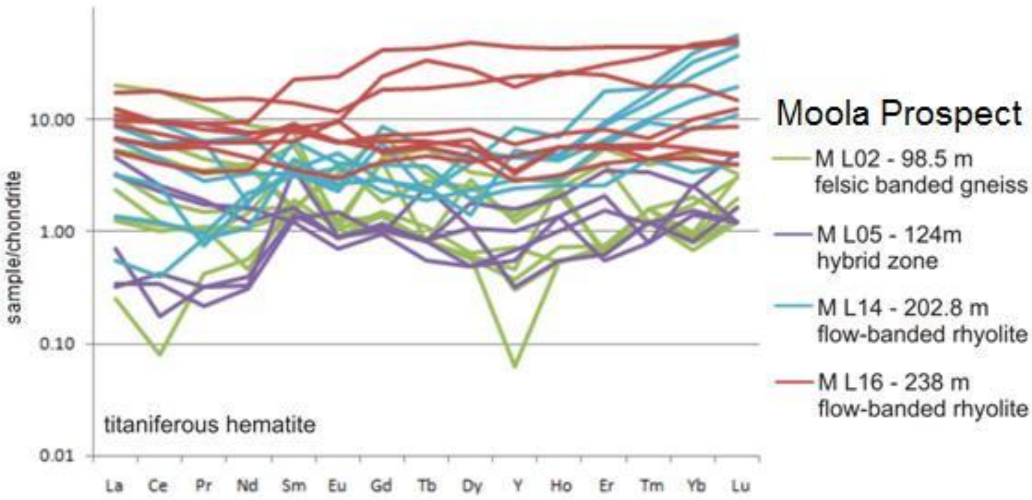

Figure 10 Chondrite-normalised REY fractionation trends for titaniferous hematite (Moola Prospect). Note irregular distribution; there is a slight increase of REY down-hole.

fine-grained disseminated ilmenite has very low variable REY concentrations. The late-stage ilmenite has elevated REY concentrations and is slightly enriched in LREE; adjacent titaniferous hematite and rutile had REY concentrations orders of magnitude lower. The resolution of analysis may have resulted in unknown inclusions within ilmenite affecting the REY concentrations.

The Fe-dominated breccia in the Princess Prospect has fine-grained bladed hematite found within the breccia clasts is slightly enriched in LREE and higher REY concentrations overall than the coarse-grained hematite found as infill (Figure 5g). Late-stage magnetite rims around bladed hematite core have higher REY enrichment than hematite (Figure 8f, Table 3).

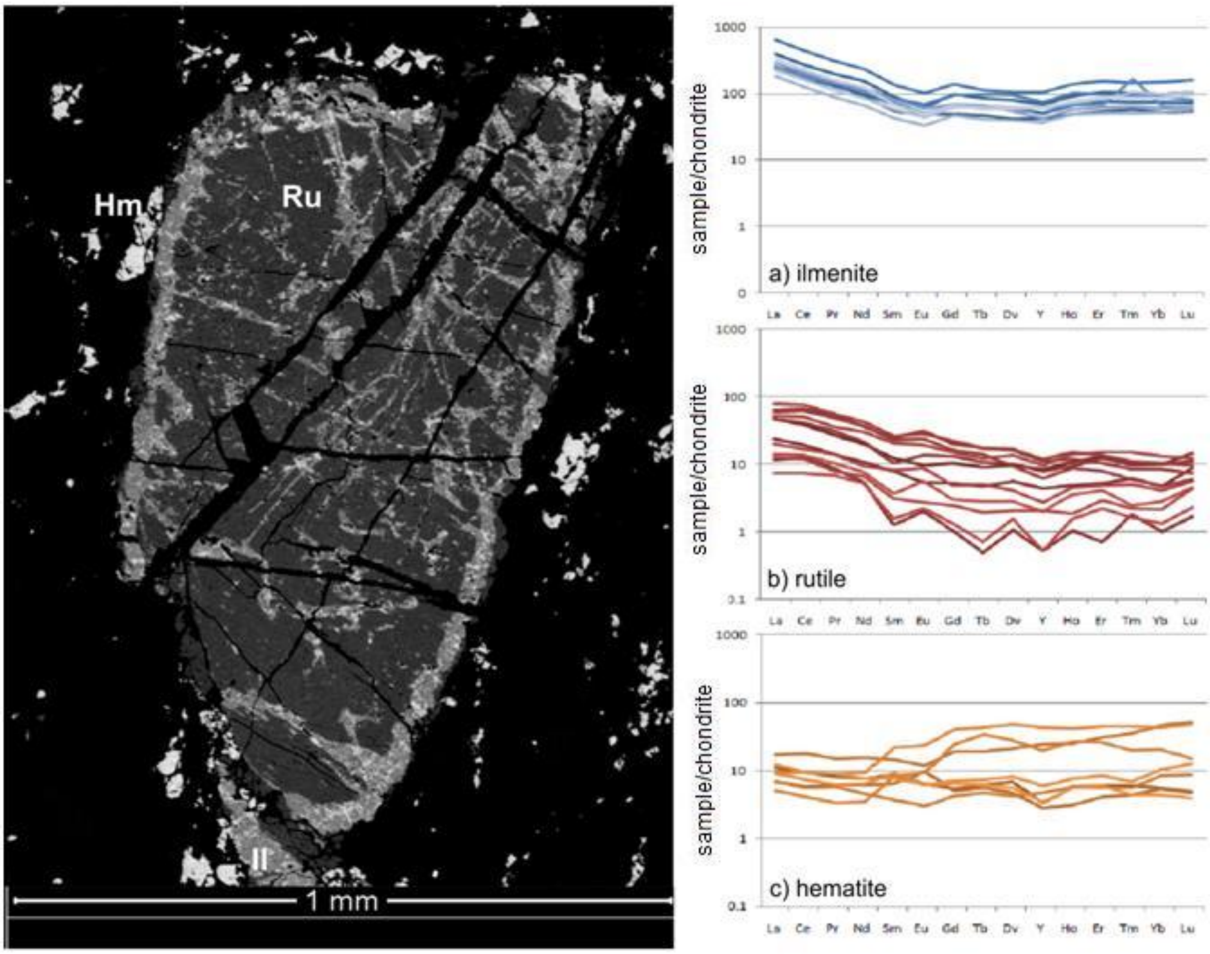

Figure 11. Back-scatter electron image showing the relationship between titaniferous hematite, rutile and ilmenite in the flow-banded rhyolite found towards the base of ML001DD. Primary titaniferous hematite is observed throughout the sample; this coarse grained rutile shows fracturing and replacement by late-stage impure ilmenite. Chondrite-normalised REY fractionation trends for a) ilmenite, b) rutile and c) hematite, clearly indicating that the late-stage ilmenite is associated with an influx of REY.

Feldspar

Feldspars (albite, microcline and perthite) were only observed in the Myola Volcanics and the Moola Prospect. Greater than 95% for all REY, except La and Ce, were below detection limits; REY plots and tabulated values have been calculated based on half the minimum detection limits. The feldspars observed in this study are not significant carriers of REE (Table 4). Although plotting data which is below minimum detection limits (Figure 11), the REY plots are moderately comparable well with those seen in Hillside (Ismail *et al.* in press). The patterns for albite and microcline are very similar, raising the question of whether the chondrite-normalised REY fractionation trends are the result of REE distribution of the feldspar or if the pattern is related to the minimum detection limits of the LA-ICP-MS method. Even if the plots are misrepresentative, the enrichment of La, Ce and Eu is, however, real as these elements are present at concentrations above detection limits.

Albite REY plots for Moola Prospect granite, felsic volcaniclastic rocks and Myola Volcanics rhyolite porphyry typically display a slight enrichment of HREE with a strong negative Y-anomaly and slight negative Eu-anomaly; this distribution is similar to hydrothermal signatures seen in early skarn assemblages at Hillside (Ismail *et al.* in press) (Figure 12a). A unique distribution is presented by the granitic veinlets which show a slight LREE enrichment, a positive Eu-anomaly and less pronounced negative Eu-anomaly.

Microcline REY plots for the Moola Prospect felsic volcaniclastic and Myola Volcanics rhyolite porphyry show similar distributions to one another, a slight enrichment of HREE with a strong negative Y-anomaly and slight negative Eu-anomaly; an exception is the Myola Volcanics has variable Eu-anomalies (Figure 12b); the granite veinlet has a similar trend of lower magnitude. In comparison the granitic veinlet has elevated La and a variable Eu-anomaly and has a similar distribution to REY plots for ‘green-rock’ with skarn overprint that is seen proximal to ore at Hillside (Ismail *et al.* in press).

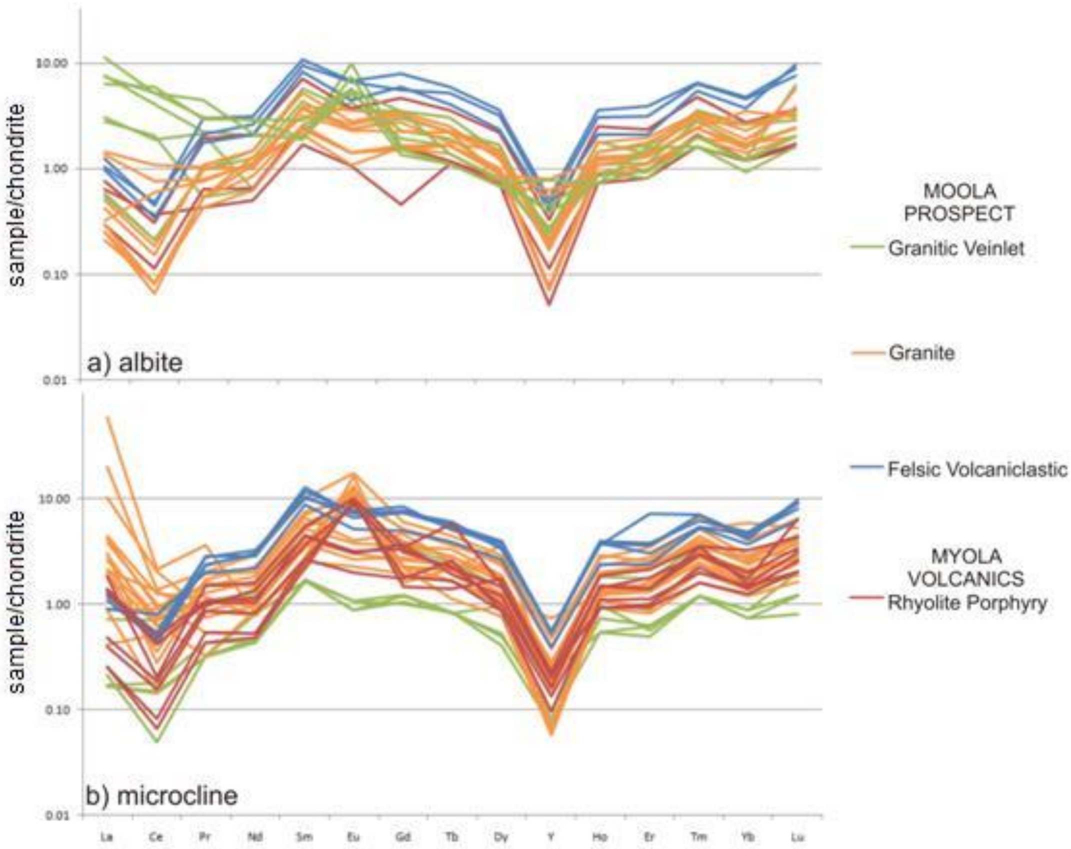

Figure 12 Chondrite-normalised fractionation trends for a) albite and b) microcline. See text for additional information.

Rutile

Several distinct generations of rutile are present; grain-size dictated which generations could be analysed (Table 5).

Rutile in the Myola Volcanic rhyolite porphyry display very different REY fractionation patterns between the two samples (Figure 13c). Rutile in MV01 has a strong association with titanite and is enriched in REE, in particular LREE, has a negative Eu- anomaly and Y-anomalies of varying size and sense (mean ΣREY: 8573 ppm) (Figure 6j, Table 5). The MV02 rutile is associated with apatite, Fe-oxides and zircon; their REY chondrite plots are of lower magnitude, typically HREE enriched relative to LREE and

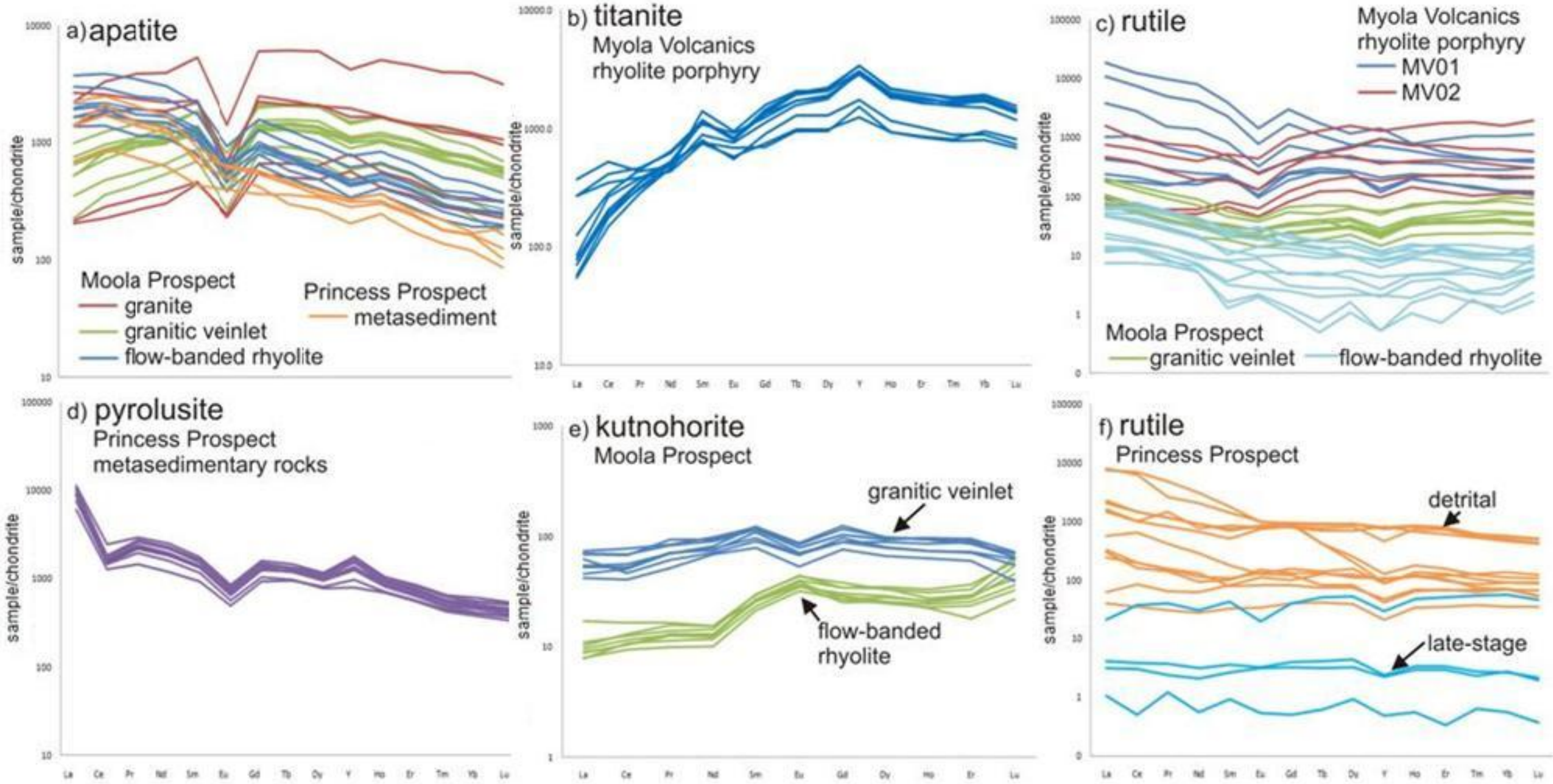

Figure 13 Chondrite-normalised REY fractionation trends for accessory minerals. a) Apatite, containing significant amounts of REY. Granitic apatite within the Moola Prospect displays a concave trend similar to Hillside ore-stage altered skarn (Ismail *et al.* in press). b) Titanite is particularly HREE-rich, a feature unique to a subset of environments within IOCG and skarn systems. c) & f) Rutile, showing variable REY plots throughout the sample suite; see text for explanation. e) Late-stage pyrolusite is a significant carrier of REY and is LREE-enriched. e) Kutnohorite REY patterns differ between samples. Note: standard used for kutnohorite analysis did not contain Tb, Y, Tm or Yb – these elements are not displayed.

with no Eu-anomaly (mean ΣREY: 1228 ppm).

Rutile in samples from the Moola Prospect contains < 130 ppm ΣREY. Rutile of magmatic/hydrothermal origin within the granitic veinlet had a slight concave chondrite plot with a small negative Y-anomaly. A single coarse-grained rutile grain associated with ilmenite was analysed from the flow-banded rhyolite; this shows a slight downwards-sloping REY fractionation trends (Figures 11 & 13c).

Corroded rutile in the Princess Prospect metasedimentary rocks typically appears to be largely detrital (Figure 6i) and features variable REY fractionation trends ranging over several orders of magnitude; some show consistent patterns with slight enrichment of LREE and negative Eu-anomalies. Late-stage rutile (potentially hydrothermal) has lower REY than the detrital rutile, and characteristically, relatively flat REY fractionation trends (Figures 6i & 13f).

Apatite

Apatite in all samples contains significant amounts of REY (ΣREY: 2986-7276 ppm) (Figure 13a, Table 6). Chondrite-normalised REE fractionation plots from the Moola Prospect show the felsic gneiss and granite have relatively flat, slightly concave patterns with a pronounced negative Eu-anomaly; a pattern similar to that seen in the ore-stage altered skarn at Hillside (Ismail *et al.* in press). The flow-banded rhyolite typically displays a gentle downwards-sloping trend and negative Eu-anomaly, which is representative of REY patterns for magmatic to early skarn apatite. Apatite REY plots from the Princess Prospect metasedimentary rocks have a negative trend with no Eu-anomaly; this is not comparable to any trends seen at Hillside (Ismail *et al.* in press).

Only two apatite analyses were conducted on the Myola Volcanic samples and they display inconsistent patterns.

Titanite

Analysed titanite from the Myola Volcanics rhyolite porphyry is relatively enriched in REY (mean ΣREY: 5472 ppm); has a concave REY chondrite-normalised plot with modest HREE-enrichment, a negative Eu-anomaly, and positive Y-anomaly (Figure13b, Table 7). Interestingly, however, the REY pattern displayed is not convex as has been observed in majority of titanite grains from analogous IOCG or skarn systems (Smith *et al.* 2009; Ismail *et al.* in press). Analogous LREE-poor, HREE-rich trends have, however, been repeated in selected environments within particular areas. For example, the Nautanen Deposit in the Nautanen Deformation Zone, Kiruna District, Sweden has the same REY distribution and magnitude, but has no Eu-anomaly (Smith *et al.* 2009). These authors suggest the LREE depletion is not related to hydrothermal activity but may be attributed to a local source for trace element via metal leaching during alteration of metavolcanic rocks, or to LREE loss during metamorphic recrystallisation. Interestingly, titanite occurring adjacent to pyrite infilled magnetite at Hillside (Ismail *et al.* in press) displayed a similar REY pattern as that reported here.

Manganese minerals

Pyrolusite and kutnohorite are shown to be carriers of REY (Table 7). The significant enrichment of REY (mean ΣREY: 7219 ppm) in late-stage pyrolusite further supports the relationship between Mn and REY, and the simultaneous remobilisation of these

Table 3 Summary of LA-ICP-MS trace element data for Fe-oxides (ppm).

Sample	Mineral		Na	Mg	Al	Si	K	Sc	Ti	V	Cr	Mn	Co	Ni	Cu	Zn	Sr	Y	Zr	Nb	Mo	Sn	Sb	Ba
MV01	Magnetite (n-9)	mean	63.1	18.1	421	4383	35.0	1.58	456	10.2	6.89	332	0.53	2.50	2.78	356	0.32	2.46	28.5	0.16	0.66	2.92	0.80	0.95
		std. dev.	17.1	17.8	159	2371	34.0	0.31	194	1.58	1.31	248	0.21	1.77	0.92	156	0.18	2.24	74.1	0.12	0.33	1.92	0.64	1.07
		min	36.7	2.70	206	2341	13.6	1.07	170	8.61	5.08	174	0.32	1.23	1.60	79.7	0.08	0.20	0.13	0.06	0.37	0.63	0.18	0.33
		max	90.5	66.6	799	8732	118	2.12	770	14.3	9.42	1000	1.01	7.33	4.40	650	0.54	6.65	238	0.46	1.55	5.99	2.04	3.92
	Martite (n-4)	mean	45.3	96.4	629	3924	71.6	6.36	311	9.85	6.08	199	0.80	1.37	11.1	352	1.95	67.9	748	0.75	0.42	1.20	2.46	0.80
		std. dev.	2.67	87.8	326	2853	45.6	2.39	16.2	0.47	0.59	23.0	0.13	0.08	6.95	82.5	0.84	54.9	725	0.60	0.02	0.96	1.14	0.54
		min	41.2	31.0	394	2193	13.5	3.51	294	9.04	5.18	173	0.62	1.29	1.52	244	0.97	12.7	9.33	0.15	0.39	0.61	1.05	0.26
		max	48.6	247	1192	8863	140	10.1	336	10.2	6.69	227	0.96	1.50	20.6	459	3.17	132	1840	1.62	0.44	2.87	4.17	1.61
	Fresh Magnetite (n-5)	mean	135	46.5	494	4516	42.4	2.43	400	14.6	8.13	266	0.49	2.44	3.97	257	0.27	0.16	0.68	0.21	0.54	2.27	0.37	1.12
		std. dev.	60.4	81.5	258	1344	37.2	1.13	131	0.92	1.39	64.6	0.06	0.32	2.39	56.8	0.35	0.08	0.98	0.13	0.04	1.03	0.14	1.28
		min	71.3	2.55	319	3164	20.3	1.64	309	13.7	6.42	188	0.40	2.00	2.22	196	0.08	0.10	0.18	0.10	0.49	0.90	0.20	0.29
		max	208	209	998	7097	117	4.64	658	16.3	9.70	375	0.55	2.86	8.69	349	0.96	0.32	2.63	0.46	0.59	3.43	0.61	3.65
			La	Ce	Pr	Nd	Sm	Eu	Gd	Tb	Dy	Ho	Er	Tm	Yb	Lu	Ta	W	^{206}Pb	^{207}Pb	^{208}Pb	Th	U	ΣREY
	Magnetite (n-9)	mean	0.74	1.54	0.19	0.72	0.29	0.07	0.22	0.05	0.50	0.12	0.51	0.09	0.70	0.12	0.21	0.14	22.2	18.9	21.7	0.36	0.44	7.49
		std. dev.	1.46	3.05	0.33	1.24	0.20	0.05	0.04	0.04	0.35	0.09	0.43	0.08	0.47	0.09	0.29	0.07	20.0	17.9	21.0	0.40	0.75	9.33
		min	0.04	0.04	0.03	0.16	0.18	0.04	0.16	0.02	0.11	0.03	0.08	0.03	0.16	0.03	0.03	0.10	2.57	1.36	1.41	0.02	0.03	0.00
		max	4.78	10.0	1.13	4.22	0.86	0.20	0.27	0.17	1.22	0.28	1.41	0.26	1.44	0.31	0.95	0.34	64.3	59.1	68.4	1.21	2.54	33.1
	Martite (n-4)	mean	2.67	8.11	0.86	2.95	1.49	0.30	1.86	0.81	9.66	3.08	12.8	2.63	21.3	3.30	0.87	0.73	106	86.1	100	5.87	8.11	140
		std. dev.	2.29	5.60	0.47	1.56	0.68	0.20	0.88	0.57	7.28	2.42	10.3	2.21	18.9	2.97	0.77	0.26	28.2	23.1	24.4	4.86	7.16	99.5
		min	0.45	1.38	0.13	0.52	0.43	0.12	0.59	0.22	2.45	0.65	2.42	0.45	2.99	0.44	0.16	0.43	67.7	55.6	65.5	2.50	0.71	28.6
		max	6.51	16.9	1.43	4.59	2.30	0.61	2.79	1.42	18.7	6.02	25.0	5.63	46.8	7.53	2.14	1.02	147	121	135	14.2	17.0	260
	Fresh Magnetite (n-5)	mean	0.06	0.11	0.04	0.22	0.24	0.07	0.25	0.03	0.13	0.03	0.11	0.03	0.16	0.03	0.33	0.35	2.48	1.74	1.46	0.05	0.08	1.67
		std. dev.	0.03	0.12	0.00	0.0	0.04	0.01	0.05	0.00	0.02	0.01	0.01	0.01	0.01	0.01	0.42	0.48	2.43	2.53	2.48	0.02	0.04	0.30
		min	0.04	0.04	0.03	0.16	0.20	0.05	0.21	0.03	0.10	0.02	0.10	0.02	0.13	0.02	0.03	0.07	0.40	0.35	0.18	0.03	0.03	1.33
		max	0.13	0.35	0.04	0.26	0.31	0.08	0.33	0.04	0.15	0.04	0.13	0.04	0.17	0.04	1.14	1.30	6.43	6.80	6.43	0.09	0.14	2.16
Sample	Mineral		Na	Mg	Al	Si	K	Sc	Ti	V	Cr	Mn	Co	Ni	Cu	Zn	Sr	Y	Zr	Nb	Mo	Sn	Sb	Ba
MV02	Magnetite (n-6)	mean	29.5	14.5	441	3028	69.0	2.60	578	13.9	4.85	119	1.43	1.17	2.52	74.3	0.34	3.81	6.28	0.34	0.43	1.41	0.22	4.34
		std. dev.	27.0	10.4	107	1193	124	1.45	172	1.06	1.71	29.7	0.47	0.53	3.5	21.4	0.20	3.55	7.72	0.48	0.32	0.97	0.04	8.37
		min	6.99	3.00	241	1103	3.85	0.35	291	12.8	1.99	97.0	0.82	0.55	0.51	48.3	0.12	0.07	0.13	0.06	0.06	0.33	0.17	0.27
		max	83.1	33.9	571	5012	345	4.33	806	15.9	7.08	181	2.01	2.06	10.3	102	0.65	9.84	19.9	1.40	0.82	3.19	0.29	23.0
	Martite (n-9)	mean	60.3	100.9	805	4985	24.5	2.90	858	16.5	4.29	236	1.24	1.38	11.8	174	2.29	53.7	49.9	5.40	3.71	2.74	1.09	1.59
		std. dev.	17.1	95.7	330	1583	10.9	1.73	288	1.94	2.03	67.7	0.42	0.42	7.97	86.8	0.57	21.1	32.9	5.92	3.40	1.64	0.82	0.52
		min	33.5	34.0	533	2956	3.31	0.40	394	13.2	1.42	137	0.46	0.91	2.06	90.7	1.39	17.8	4.53	0.17	1.00	0.58	0.48	0.58
		max	90.1	363	1663	8474	40.4	4.62	1360	20.7	7.24	357	2.07	2.29	27.8	342	3.24	77.2	121	16.2	12.5	5.64	3.19	2.43

Table 3 cont. Summary of LA-ICP-MS trace element data for Fe-oxides (ppm).

Sample	Mineral		La	Ce	Pr	Nd	Sm	Eu	Gd	Tb	Dy	Ho	Er	Tm	Yb	Lu	Ta	W	^{206}Pb	^{207}Pb	^{208}Pb	Th	U	ΣREY
MV02	Magnetite (n-6)	mean	0.17	0.37	0.09	0.30	0.41	0.07	0.41	0.14	0.92	0.18	0.56	0.08	0.51	0.08	0.19	0.13	9.72	4.85	9.09	0.95	0.34	8.09
		std. dev.	0.14	0.34	0.06	0.10	0.25	0.03	0.26	0.11	0.69	0.19	0.55	0.06	0.44	0.06	0.20	0.03	7.55	5.22	7.15	1.25	0.29	6.49
		min	0.04	0.03	0.03	0.19	0.21	0.04	0.21	0.03	0.16	0.04	0.10	0.03	0.15	0.03	0.03	0.10	0.27	0.11	0.22	0.04	0.02	1.53
		max	0.38	0.91	0.17	0.45	0.80	0.12	0.86	0.34	1.95	0.48	1.54	0.18	1.33	0.19	0.63	0.20	23.5	14.9	22.0	3.4	0.74	18.4
	Martite (n-9)	mean	28.2	14.4	7.58	32.5	8.55	1.48	11.6	1.84	11.0	2.00	4.97	0.59	3.04	0.49	0.24	0.70	59.4	41.8	57.0	20.5	1.45	182
		std. dev.	22.9	12.1	6.66	28.1	6.81	0.97	7.21	0.95	4.43	0.68	1.46	0.17	0.95	0.09	0.13	0.56	36.0	24.6	34.8	12.1	0.71	109
		min	1.01	1.57	0.46	1.28	0.82	0.26	2.28	0.53	4.87	1.14	3.11	0.37	1.62	0.38	0.03	0.12	18.2	14.5	18.4	2.71	0.47	38.2
		max	63.2	32.2	17.4	73.7	19.5	2.94	21.5	3.12	16.9	2.84	6.83	0.87	4.61	0.65	0.49	1.81	126	87.5	119	40.5	2.43	322
Sample	**Mineral**		**Na**	**Mg**	**Al**	**Si**	**K**	**Sc**	**Ti**	**V**	**Cr**	**Mn**	**Co**	**Ni**	**Cu**	**Zn**	**Sr**	**Y**	**Zr**	**Nb**	**Mo**	**Sn**	**Sb**	**Ba**
ML02	Titaniferous Hematite (n-11)	mean	119	143	588	6396	31.8	51.3	110448	1903	1481	1843	13.4	17.4	3.89	51.4	3.11	1.61	3.81	150	4.17	179	7.18	1.50
		std. dev.	75.7	71.7	279	1045	12.3	15.6	13264	232	884	904	3.87	5.29	1.77	26.8	8.50	1.36	2.73	180	1.90	34.1	8.70	1.80
		min	8.49	49.74	257	4345	4.43	29.2	92681	1643	655.1	628.1	8.01	8.00	2.15	24.60	0.06	0.10	0.98	8.61	1.97	119	0.53	0.27
		max	317	263	1004	7688	43.2	85.3	137819	2466	3891	3125	21.5	26.5	8.07	103	30.0	4.71	10.5	674	8.73	226	32.5	6.49
			La	**Ce**	**Pr**	**Nd**	**Sm**	**Eu**	**Gd**	**Tb**	**Dy**	**Ho**	**Er**	**Tm**	**Yb**	**Lu**	**Ta**	**W**	**^{206}Pb**	**^{207}Pb**	**^{208}Pb**	**Th**	**U**	**ΣREY**
		mean	1.41	2.77	0.31	1.35	0.43	0.09	0.52	0.06	0.37	0.08	0.24	0.04	0.26	0.05	33.1	15.1	8.84	6.31	5.78	0.62	2.06	9.60
		std. dev.	1.48	3.20	0.33	1.17	0.30	0.06	0.38	0.05	0.25	0.05	0.26	0.02	0.19	0.02	20.7	33.7	8.62	7.43	6.94	0.71	1.91	8.65
		min	0.06	0.05	0.03	0.21	0.22	0.05	0.20	0.03	0.12	0.03	0.01	0.03	0.11	0.03	6.93	0.28	2.97	0.96	0.92	0.03	0.39	1.50
		max	4.75	10.9	1.18	4.07	1.12	0.23	1.44	0.20	0.83	0.15	0.87	0.10	0.77	0.08	64.6	120	34.8	28.7	26.7	2.65	6.79	30.7
Sample	**Mineral**		**Na**	**Mg**	**Al**	**Si**	**K**	**Sc**	**Ti**	**V**	**Cr**	**Mn**	**Co**	**Ni**	**Cu**	**Zn**	**Sr**	**Y**	**Zr**	**Nb**	**Mo**	**Sn**	**Sb**	**Ba**
ML05	Titaniferous Hematite (n-5)	mean	7.62	215	953	6626	5.16	89.2	116436	1769	358	7668	30.6	36.3	5.05	82.0	0.27	1.32	6.29	40.7	1.35	202	1.27	0.41
		std. dev.	0.91	62.3	141	1005	2.67	5.06	10835	68.9	12.7	4540	8.05	6.36	0.46	38.9	0.28	0.72	3.30	37.3	0.49	22.2	1.09	0.21
		min	6.45	128	821	4976	3.37	79.8	105316	1686	341	3127	22.5	26.2	4.37	33.7	0.04	0.50	3.01	6.90	0.76	164	0.08	0.20
		max	8.71	319	1171	7970	10.4	94.7	132804	1857	378	16002	45.6	46.0	5.51	147	0.69	2.56	10.5	90.6	2.03	231	3.00	0.76
			La	**Ce**	**Pr**	**Nd**	**Sm**	**Eu**	**Gd**	**Tb**	**Dy**	**Ho**	**Er**	**Tm**	**Yb**	**Lu**	**Ta**	**W**	**^{206}Pb**	**^{207}Pb**	**^{208}Pb**	**Th**	**U**	**ΣREY**
		mean	0.44	0.72	0.09	0.36	0.27	0.06	0.21	0.04	0.24	0.07	0.27	0.04	0.29	0.05	11.5	3.34	2.12	2.13	0.98	0.33	1.23	9.60
		std. dev.	0.42	0.65	0.07	0.25	0.14	0.02	0.02	0.02	0.12	0.03	0.18	0.02	0.11	0.04	6.81	5.85	1.31	1.98	0.56	0.38	1.48	8.65
		min	0.08	0.11	0.02	0.14	0.18	0.04	0.19	0.02	0.12	0.03	0.09	0.02	0.13	0.03	2.87	0.12	1.04	0.14	0.30	0.03	0.31	1.50
		max	1.10	1.61	0.18	0.75	0.54	0.09	0.24	0.09	0.45	0.11	0.57	0.09	0.41	0.13	22.3	15.0	4.68	5.83	1.99	1.07	4.19	30.7
Sample	**Mineral**		**Na**	**Mg**	**Al**	**Si**	**K**	**Sc**	**Fe**	**V**	**Cr**	**Mn**	**Co**	**Ni**	**Cu**	**Zn**	**Sr**	**Y**	**Zr**	**Nb**	**Mo**	**Sn**	**Sb**	**Ba**
ML14	Ilmenite (n-7)	mean	*	104	115	15053	*	13.9	343367	385	165	662	2.23	*	14.9	35.0	2.52	3.99	330	524	1.55	2.95	1.99	3.17
		std. dev.		59.3	94.8	11150		4.73	31612	109	168	149	0.71		11.6	10.0	1.27	1.90	483	259	0.83	2.32	0.86	2.62
		min		53.7	21.4	5054		6.75	287101	244	19.4	448	1.40		4.61	19.5	0.59	1.71	0.39	343	0.74	0.85	0.72	0.33
		max		235	324	35481		20.9	398087	536	551	988	3.34		39.1	53.9	4.77	7.01	1470	1091	2.71	7.54	3.09	8.49
			La	**Ce**	**Pr**	**Nd**	**Sm**	**Eu**	**Gd**	**Tb**	**Dy**	**Ho**	**Er**	**Tm**	**Yb**	**Lu**	**Ta**	**W**	**^{206}Pb**	**^{207}Pb**	**^{208}Pb**	**Th**	**U**	**ΣREY**
		mean	1.33	2.31	0.24	1.06	0.28	0.12	0.44	0.06	0.79	0.16	0.77	0.16	1.44	0.30	26.3	28.6	10.2	11.0	8.46	0.63	1.41	13.5
		std. dev.	1.48	2.66	0.29	1.25	0.08	0.06	0.23	0.04	0.60	0.10	0.42	0.07	1.22	0.23	4.11	35.3	4.36	7.61	5.30	0.63	0.74	7.44
		min	0.04	0.19	0.03	0.16	0.20	0.05	0.21	0.03	0.16	0.04	0.13	0.08	0.18	0.05	20.3	6.12	5.49	3.48	3.62	0.10	0.21	6.05
		max	4.43	8.15	0.90	4.00	0.47	0.21	0.92	0.13	2.13	0.35	1.62	0.30	3.85	0.70	33.7	108	19.8	27.7	19.7	1.99	2.69	29.8

Table 3 cont. Summary of LA-ICP-MS trace element data for Fe-oxides (ppm).

Sample	Mineral		Na	Mg	Al	Si	K	Sc	Ti	V	Cr	Mn	Co	Ni	Cu	Zn	Sr	Y	Zr	Nb	Mo	Sn	Sb	Ba
ML16	Hematite (n-9)	mean	1699	1183	9279	25322	3929	7.67	2783	574	5.44	156	8.08	8.50	7.66	24.3	5.29	23.6	163	4.31	0.85	16.7	7.67	28.4
		std. dev.	1023	668	8220	19651	3873	3.12	1455	129	1.55	125	1.15	1.62	3.89	12.1	3.47	24.5	224	2.63	0.20	8.97	4.43	25.5
		min	136	432	1669	13476	995	4.08	742	460	3.15	51.2	6.55	7.45	2.54	10.7	1.80	5.26	7.47	1.01	0.55	4.01	2.32	6.78
		max	3268	2356	24850	64430	11228	13.3	4219	749	7.61	392	9.89	11.7	13.0	41.8	10.4	68.4	607	8.30	1.14	28.2	14.6	77.5
			La	Ce	Pr	Nd	Sm	Eu	Gd	Tb	Dy	Ho	Er	Tm	Yb	Lu	Ta	W	^{206}Pb	^{207}Pb	^{208}Pb	Th	U	ΣREY
		mean	2.14	4.68	0.66	2.99	1.51	0.55	3.26	0.68	4.58	0.95	2.81	0.40	2.67	0.40	0.37	4.68	19.6	17.2	17.1	4.34	5.42	19.4
		std. dev.	0.63	1.42	0.21	1.00	0.93	0.41	2.88	0.59	4.23	0.83	2.48	0.38	2.39	0.40	0.26	1.88	9.04	6.12	6.23	3.95	5.45	5.73
		min	1.23	2.53	0.32	1.58	0.55	0.17	0.85	0.17	1.06	0.31	0.90	0.11	0.70	0.10	0.04	1.79	9.74	10.0	9.80	1.10	1.41	11.6
		max	2.93	5.86	0.85	4.35	3.30	1.34	8.17	1.54	11.8	2.33	7.11	1.11	7.09	1.17	0.75	6.91	33.8	25.2	26.2	12.0	16.0	28.0
	Ilmenite (n-9)		Na	Mg	Al	Si	K	Sc	Fe	V	Cr	Mn	Co	Ni	Cu	Zn	Sr	Y	Zr	Nb	Mo	Sn	Sb	Ba
		mean	13122	1211	1867	35425	1382	150	400648	489	202	635	3.67	20.0	43.4	51.0	23.0	95.3	110	472	0.33	30.8	13.8	39.2
		std. dev.	1294	595	1670	4744	742	58.6	78211	141	52.8	172	0.92	5.00	8.30	20.4	6.62	29.1	201	139	0.11	7.77	2.54	9.35
		min	11159	368	669	29933	991	70.3	278212	291	131	371	2.43	7.54	35.9	17.5	16.9	55.8	2.28	276	0.12	19.2	8.06	23.9
		max	15385	2529	5437	46414	3460	229	557360	773	306	904	5.43	25.6	61.2	82.5	37.5	161	656	786	0.47	41.9	17.2	52.5
			La	Ce	Pr	Nd	Sm	Eu	Gd	Tb	Dy	Ho	Er	Tm	Yb	Lu	Ta	W	^{206}Pb	^{207}Pb	^{208}Pb	Th	U	ΣREY
		mean	74.2	134	15.0	56.8	11.4	3.27	15.8	2.62	17.0	4.42	14.2	2.44	13.9	2.20	57.7	127	87.8	62.9	60.2	16.1	18.4	462
		std. dev.	31.4	52.9	5.67	21.6	3.58	1.08	5.22	0.79	4.95	1.40	4.79	0.89	4.60	0.77	29.4	50.7	21.9	15.1	16.1	5.26	4.54	169
		min	43.8	77.4	8.20	30.9	6.40	1.89	9.61	1.48	9.93	2.72	8.28	1.27	8.47	1.44	26.6	75.0	63.3	46.2	44.0	6.75	10.4	268
		max	154	268	29.1	110	20.0	5.86	27.9	4.23	26.7	7.65	25.6	4.16	24.8	4.01	120	249	133	96.8	98.6	25.6	25.9	873
Sample	Mineral		Na	Mg	Al	Si	K	Sc	Ti	V	Cr	Mn	Co	Ni	Cu	Zn	Sr	Y	Zr	Nb	Mo	Sn	Sb	Ba
PS01	Bladed Hematite c.g. (n-6)	mean	92.5	36.9	297	7073	34.9	1.70	279	22.0	9.12	103	0.40	4.44	1.65	10.6	0.38	0.96	1.12	5.32	2.56	86.6	23.1	2.42
		std. dev.	6.85	11.2	66.9	546	1.34	0.11	96.9	5.35	0.77	26.2	0.12	1.44	0.13	5.04	0.16	0.24	0.18	1.76	1.66	16.2	4.21	0.37
		min	83.9	18.8	185	6321	32.6	1.59	156	14.4	7.93	80.9	0.33	1.78	1.49	2.39	0.11	0.59	0.76	2.88	0.50	68.8	17.2	1.96
		max	101	50.8	406	8026	36.7	1.92	442	30.0	10.3	152	0.67	5.75	1.87	17.1	0.63	1.29	1.32	7.33	5.13	121	29.0	2.94
	Bladed Hematite f.g. (n-6)	mean	146	110	543	5178	33.7	1.48	330	21.3	18.9	274	0.74	10.0	5.26	8.06	0.87	1.62	2.08	3.40	1.27	31.4	10.1	2.76
		std. dev.	105	106	249	520	2.30	0.10	157	12.8	11.2	366	0.28	3.75	2.30	4.10	0.33	0.53	1.79	2.45	1.24	28.8	4.21	1.00
		min	88.6	22.0	296	4805	30.4	1.34	173	13.0	8.83	60.7	0.31	7.02	1.87	2.06	0.45	0.97	0.91	1.36	0.44	7.66	6.65	1.60
		max	382	260	1062	6312	37.6	1.65	608	49.3	40.0	1080	1.04	18.0	7.76	14.4	1.38	2.69	6.04	8.62	3.96	90.8	18.9	4.27
			La	Ce	Pr	Nd	Sm	Eu	Gd	Tb	Dy	Ho	Er	Tm	Yb	Lu	Ta	W	^{206}Pb	^{207}Pb	^{208}Pb	Th	U	ΣREY
	Bladed Hematite c.g. (n-6)	mean	0.53	0.87	0.10	0.58	0.38	0.08	0.27	0.04	0.18	0.05	0.11	0.04	0.15	0.04	0.15	87.5	10.8	9.47	8.82	1.09	1.90	4.38
		std. dev.	0.21	0.47	0.08	0.30	0.22	0.04	0.10	0.02	0.09	0.02	0.01	0.00	0.01	0.01	0.04	21.3	4.18	4.50	3.63	0.38	0.45	1.02
		min	0.25	0.49	0.03	0.21	0.21	0.04	0.20	0.03	0.12	0.03	0.10	0.03	0.14	0.03	0.09	57.9	7.17	5.09	5.37	0.31	1.06	2.82
		max	0.88	1.85	0.23	1.01	0.78	0.14	0.50	0.08	0.38	0.09	0.12	0.04	0.17	0.04	0.23	125	17.4	18.6	15.0	1.49	2.48	5.71
	Bladed Hematite f.g. (n-6)	mean	1.33	1.89	0.25	1.05	0.33	0.17	0.45	0.04	0.12	0.04	0.12	0.04	0.16	0.03	0.16	21.8	8.05	7.57	7.82	1.05	1.47	7.63
		std. dev.	0.65	0.81	0.10	0.50	0.12	0.06	0.17	0.02	0.01	0.02	0.06	0.01	0.07	0.01	0.09	22.2	3.19	2.11	1.87	0.94	1.37	2.17
		min	0.47	0.52	0.10	0.34	0.18	0.07	0.18	0.02	0.09	0.03	0.07	0.03	0.09	0.02	0.03	3.90	4.32	4.47	4.24	0.23	0.70	3.59
		max	2.33	2.83	0.36	1.89	0.46	0.26	0.70	0.07	0.13	0.07	0.22	0.06	0.25	0.05	0.28	70.0	14.2	10.1	9.75	3.06	4.51	10.3

Table 3 cont. Summary of LA-ICP-MS trace element data for Fe-oxides (ppm).

Sample	Mineral		Na	Mg	Al	Si	K	Sc	Ti	V	Cr	Mn	Co	Ni	Cu	Zn	Sr	Y	Zr	Nb	Mo	Sn	Sb	Ba
PS02	Bladed Hematite (n-3)	mean	43.0	31.0	248	2640	5.38	0.37	11.1	9.32	2.32	80.2	3.09	33.7	6.30	14.3	0.70	1.12	0.61	0.04	11.1	0.52	14.2	4.47
		std. dev.	9.33	14.8	42.5	1463	2.72	0.02	3.06	1.78	1.38	7.04	1.58	3.80	3.09	8.03	0.41	0.44	0.24	0.00	1.39	0.17	3.52	1.40
		min	33.5	16.9	211	810	3.27	0.35	8.73	7.28	1.30	74.1	1.82	29.9	3.03	6.14	0.38	0.62	0.40	0.04	9.15	0.29	9.35	2.59
		max	55.7	51.5	308	4392	9.22	0.39	15.4	11.6	4.27	90.1	5.32	38.9	10.4	25.2	1.28	1.68	0.95	0.04	12.3	0.68	17.7	5.93
	Hematite (n-2)	mean	55.6	57.1	745	2362	18.8	0.62	11.6	10.7	5.54	57.0	6.09	22.6	24.0	25.3	0.66	0.73	3.01	0.04	8.46	1.46	8.23	2.18
		std. dev.	18.7	34.9	477	635	4.82	0.27	2.29	3.18	1.18	11.0	1.48	4.19	8.66	12.8	0.10	0.08	2.18	0.00	3.04	1.17	4.81	0.87
		min	36.9	22.2	268	1727	14.0	0.35	9.31	7.48	4.36	46.0	4.61	18.5	15.3	12.5	0.57	0.65	0.83	0.04	5.42	0.29	3.42	1.31
		max	74.3	92.0	1222	2998	23.6	0.89	13.9	13.8	6.72	68.0	7.56	26.8	32.7	38.1	0.76	0.81	5.18	0.04	11.5	2.62	13.0	3.04
	Magnetite (n-2)	mean	335	309	967	5043	25.3	2.76	3.30	2.15	0.93	777	153	518	630	219	7.07	20.8	0.75	0.03	73.3	0.36	3.85	9.89
		std. dev.	160	5.60	287	933	14.7	0.88	0.18	0.63	0.02	54.5	17.3	69.2	141	37.6	0.91	2.82	0.21	0.01	3.25	0.18	0.83	2.09
		min	175	303	680	4110	10.6	1.88	3.12	1.52	0.91	722	136	449	489	181	6.16	18.0	0.54	0.02	70.0	0.18	3.02	7.80
		max	495	315	1254	5976	40.0	3.63	3.49	2.78	0.94	831	171	587	772	257	7.98	23.7	0.96	0.03	76.5	0.54	4.67	12.0
			La	**Ce**	**Pr**	**Nd**	**Sm**	**Eu**	**Gd**	**Tb**	**Dy**	**Ho**	**Er**	**Tm**	**Yb**	**Lu**	**Ta**	**W**	**^{206}Pb**	**^{207}Pb**	**^{208}Pb**	**Th**	**U**	**ΣREY**
	Bladed Hematite (n-3)	mean	0.14	0.40	0.06	0.27	0.16	0.07	0.36	0.05	0.14	0.05	0.18	0.03	0.09	0.03	0.02	2.21	9.81	9.94	9.14	0.02	1.13	3.16
		std. dev.	0.04	0.10	0.05	0.22	0.01	0.03	0.16	0.03	0.08	0.02	0.08	0.00	0.00	0.02	0.00	2.07	4.02	4.14	4.03	0.00	0.25	0.51
		min	0.09	0.31	0.02	0.11	0.14	0.03	0.14	0.03	0.09	0.02	0.07	0.02	0.09	0.02	0.02	0.47	6.14	6.10	5.52	0.02	0.78	2.75
		max	0.18	0.54	0.13	0.59	0.17	0.11	0.49	0.09	0.25	0.08	0.26	0.03	0.10	0.06	0.02	5.12	15.4	15.7	14.8	0.02	1.31	3.88
	Hematite (n-2)	mean	0.31	1.18	0.20	0.71	0.35	0.04	0.30	0.04	0.18	0.04	0.17	0.04	0.09	0.05	0.09	2.80	11.0	11.7	11.9	0.04	1.75	4.41
		std. dev.	0.16	0.57	0.12	0.58	0.19	0.01	0.16	0.02	0.09	0.01	0.10	0.02	0.00	0.03	0.07	1.70	1.06	2.16	1.42	0.02	1.27	1.74
		min	0.15	0.62	0.08	0.13	0.16	0.03	0.14	0.02	0.09	0.03	0.07	0.02	0.09	0.02	0.02	1.10	9.90	9.58	10.5	0.02	0.47	2.67
		max	0.47	1.75	0.33	1.29	0.53	0.04	0.46	0.05	0.27	0.05	0.27	0.05	0.09	0.08	0.17	4.50	12.0	13.9	13.3	0.06	3.02	6.15
	Magnetite (n-2)	mean	6.38	18.6	2.58	14.8	4.69	1.30	4.65	0.63	4.07	0.88	2.87	0.54	3.39	0.66	0.02	0.09	13.46	15.8	14.1	0.13	10.0	86.9
		std. dev.	3.01	8.54	1.20	5.68	1.60	0.39	1.14	0.13	0.42	0.10	0.08	0.00	0.18	0.01	0.01	0.04	3.80	4.63	4.54	0.04	0.04	25.3
		min	3.37	10.1	1.39	9.12	3.09	0.91	3.51	0.51	3.65	0.78	2.79	0.54	3.21	0.66	0.01	0.05	9.66	11.2	9.51	0.09	10.0	61.7
		max	9.39	27.2	3.78	20.5	6.29	1.70	5.78	0.76	4.49	0.98	2.94	0.55	3.56	0.67	0.02	0.14	17.3	20.5	18.6	0.18	10.1	112

Fe- Oxide elements removed because 95% below detection limit = P (408), Ca (4166) and Rb (0.51); ilmenite: *= 95% below detection limit. Fe was removed because it was used as the internal standard. The titanium value given is an average of calculated total Ti based on measurement of ^{47}Ti and ^{48}Ti.

Table 4 Summary of LA-ICP-MS trace element data for feldspar (ppm).

			Na	Mg	K	Ca	Sc	Ti	V	Mn	Fe	Cu	Zn	Rb	Sr	Y	Zr	Ba	La
ML02	Albite (n-4)	Mean	86896	1085	16520	3326	7.62	25.4	2.65	44.6	3363	10.8	8.62	119	87.5	0.40	0.61	127	2.56
		St dev	10151	295	2973	847	1.38	10.1	1.19	11.7	840	4.99	3.06	17.6	23.7	0.06	0.56	65.6	2.98
		Min	75010	807	13191	2504	6.38	15.1	1.42	35.1	2534	4.72	3.95	101	57.7	0.29	0.21	54.7	0.68
		Max	99540	1534	20024	4628	9.94	41.9	4.58	64.3	4718	18.1	12.5	146	119	0.45	1.57	231	7.72
	albite diff (n-4)	Mean	67525	727	12692	5758	5.44	33.9	3.17	55.7	1849	7.19	6.71	78.0	115	0.71	0.16	74.3	1.94
		St dev	3743	435	2650	1746	0.97	9.74	3.12	15.2	1024	4.73	3.08	34.5	20.5	0.32	0.02	44.6	0.44
		Min	61156	233	8782	3517	4.30	26.3	0.11	31.3	452	0.79	2.33	25.7	84.2	0.33	0.13	29.5	1.52
		Max	70736	1416	16145	7798	6.80	50.2	8.38	71.9	3236	12.9	10.9	116	140	1.22	0.17	148	2.67
			Ce	Pr	Nd	Sm	Eu	Gd	Tb	Dy	Ho	Er	Tm	Yb	Lu	Pb206	Pb207	Pb208	ΣREY
ML02	Albite (n-4)	Mean	5.28	0.47	1.41	0.45	0.30	0.41	0.13	0.23	0.06	0.19	0.06	0.24	0.08	4.07	3.75	3.28	11.5
		St dev	6.67	0.64	1.88	0.19	0.15	0.07	0.14	0.02	0.00	0.02	0.01	0.03	0.04	1.33	1.38	1.10	11.5
		Min	1.16	0.05	0.29	0.29	0.10	0.33	0.04	0.20	0.05	0.15	0.05	0.20	0.05	2.08	1.68	1.96	4.59
		Max	16.8	1.75	5.13	0.81	0.55	0.52	0.42	0.27	0.06	0.21	0.07	0.27	0.15	5.80	5.49	4.75	34.5
	albite diff (n-4)	Mean	3.15	0.33	1.22	0.33	0.35	0.42	0.04	0.18	0.04	0.18	0.04	0.18	0.05	3.66	4.08	4.00	9.55
		St dev	0.42	0.07	0.17	0.07	0.05	0.19	0.00	0.01	0.00	0.05	0.00	0.02	0.00	1.25	1.63	1.32	0.28
		Min	2.51	0.27	0.98	0.28	0.31	0.27	0.04	0.17	0.04	0.13	0.04	0.15	0.04	2.55	2.84	3.03	9.16
		Max	3.68	0.42	1.35	0.43	0.41	0.69	0.05	0.20	0.05	0.25	0.05	0.20	0.05	5.74	6.88	6.26	9.80
			Na	Mg	K	Ca	Sc	Ti	V	Mn	Fe	Cu	Zn	Rb	Sr	Y	Zr	Ba	La
ML05	Albite (n-4)	Mean	90467	363	3770	5241	5.84	21.2	1.39	24.4	1635	14.6	9.43	28.9	100	0.37	1.10	25.1	0.40
		St dev	6651	315	2372	616	1.70	4.62	0.16	3.79	1700	5.41	1.75	19.7	11.6	0.06	0.65	11.3	0.52
		Min	84414	13.2	349	4414	4.21	17.5	1.17	20.2	191	8.49	7.30	0.89	80.2	0.29	0.63	14.8	0.04
		Max	101406	855	6023	6035	8.67	29.1	1.62	29.4	4464	23.3	11.8	53.7	109	0.45	2.22	44.0	1.29
	Microcline (n-5)	Mean	2303	4201	77212	2132	8.85	461	54.7	114	13817	22.5	20.1	683	34.1	0.22	1.90	645	0.08
		St dev	3267	2128	50356	1373	3.21	228	27.8	69.1	7011	9.93	5.58	173	65.5	0.11	0.69	361	0.05
		Min	387	6.66	50900	1368	4.35	26.0	1.23	11.9	164	10.5	10.0	543	0.80	0.11	0.82	309	0.04
		Max	8809	5664	177907	4873	12.7	666	80.9	228	19301	34.2	26.7	1025	165	0.36	2.94	1346	0.17
	Perthite (n-4)	Mean	32059	3780	32200	3144	5.54	173	35.2	82.8	9653	60.4	15.3	381	23.0	4.88	32.7	135	0.22
		St dev	2259	642	4585	1062	2.08	103	16.3	20.4	3316	43.2	7.79	104	7.68	4.60	32.1	22.1	0.16
		Min	29800	3137	27615	2082	3.46	70.0	18.9	62.4	6337	17.2	7.50	277	15.3	0.28	0.58	113	0.06
		Max	34319	4422	36785	4205	7.61	276	51.5	103	12969	104	23.1	485	30.7	9.47	64.8	157	0.37
			Ce	Pr	Nd	Sm	Eu	Gd	Tb	Dy	Ho	Er	Tm	Yb	Lu	Pb206	Pb207	Pb208	ΣREY
ML05	Albite (n-4)	Mean	0.33	0.20	0.60	2.92	0.23	0.64	0.10	0.51	0.10	0.27	0.09	0.55	0.08	2.96	2.06	2.09	7.85
		St dev	0.38	0.17	0.06	3.62	0.14	0.08	0.01	0.24	0.03	0.07	0.02	0.15	0.01	1.57	1.20	1.06	4.33
		Min	0.09	0.09	0.51	0.64	0.13	0.54	0.08	0.35	0.07	0.20	0.07	0.42	0.06	0.92	0.87	1.05	4.02
		Max	0.99	0.50	0.67	9.19	0.47	0.75	0.11	0.92	0.14	0.38	0.11	0.79	0.10	5.34	4.07	3.87	14.9

Elements removed because 95% below detection limit (average det. lim. in brackets) = Cr (5.97), Ni (1.46), Zr (0.42), Nb(0.18), Mo (0.98), Sn (1.30), Sb (0.33), Ta (0.12), W (0.34), Th (0.12) & U (0.07). Pr (0.09), Nd (0.59), Sm (0.74), Eu (0.17), Gd (0.79), Tb (0.11), Ho (0.12), Er (0.35), Tm (0.12), Yb (0.49), Lu (0.11) are displayed but are calculated on half the minimum detection limit, Al was removed as it was used as the internal standard. The Si content of feldspars is not relevant to this study and as such is not displayed. The titanium value given is an average of calculated total Ti based on measurement of ^{47}Ti and ^{48}Ti.

Table 4 cont. Summary of LA-ICP-MS trace element data for feldspar (ppm).

			Ce	Pr	Nd	Sm	Eu	Gd	Tb	Dy	Ho	Er	Tm	Yb	Lu	Pb206	Pb207	Pb208	ΣREY
ML05	Microcline (n-5)	Mean	0.15	0.05	0.31	0.35	0.16	0.32	0.04	0.19	0.05	0.13	0.04	0.18	0.04	21.4	17.5	18.2	2.30
		St dev	0.14	0.03	0.15	0.21	0.21	0.19	0.02	0.09	0.03	0.08	0.02	0.10	0.02	34.4	30.9	31.4	1.39
		Min	0.03	0.03	0.20	0.24	0.05	0.20	0.03	0.10	0.03	0.08	0.03	0.12	0.02	3.04	1.49	1.83	1.43
		Max	0.43	0.10	0.58	0.78	0.57	0.69	0.09	0.35	0.10	0.28	0.09	0.39	0.09	90.2	79.4	81.0	5.07
	Perthite (n-2)	Mean	0.32	0.15	0.80	1.13	0.25	0.95	0.16	0.90	0.19	0.70	0.13	0.84	0.14	4.27	3.11	3.81	10.4
		St dev	0.12	0.13	0.65	0.94	0.14	0.79	0.10	0.46	0.09	0.37	0.08	0.42	0.09	0.84	0.32	0.42	5.19
		Min	0.20	0.05	0.27	0.37	0.12	0.28	0.06	0.26	0.07	0.20	0.05	0.25	0.06	3.43	2.79	3.39	3.09
		Max	0.44	0.33	1.72	2.45	0.44	2.06	0.30	1.29	0.28	1.07	0.25	1.23	0.26	5.11	3.42	4.22	14.8

			Na	Mg	K	Ca	Sc	Ti	V	Mn	Fe	Cu	Zn	Rb	Sr	Y	Zr	Ba	La
ML07	Albite (n-1)	Mean	82768	2.89	387	4809	4.18	20.9	1.40	5.27	362	8.80	12.1	1.80	79.8	0.52	1.04	3.41	0.18
		St dev	0.00	0.00	0.00	0.00	0.00	0.00	0.00	0.00	0.00	0.00	0.00	0.00	0.0	0.00	0.00	0.00	0.00
		Min	82768	2.89	387	4809	4.18	20.9	1.40	5.27	362	8.80	12.1	1.80	79.8	0.52	1.04	3.41	0.18
		Max	82768	2.89	387	4809	4.18	20.9	1.40	5.27	362	8.80	12.1	1.80	79.8	0.52	1.04	3.41	0.18
	Microcline (n-5)	Mean	9650	3.73	153913	5227	4.63	29.9	1.51	21.8	204	9.84	12.8	1206	92.8	0.57	1.09	1197	1.42
		St dev	2308	1.08	16268	887	0.72	12.0	0.22	5.52	37.7	1.68	3.11	167	12.1	0.12	0.19	242	1.67
		Min	7560	2.69	132460	4177	3.84	20.7	1.28	15.1	162	8.22	9.01	981	70.6	0.43	0.88	880	0.21
		Max	14003	5.77	175755	6791	5.86	53.6	1.86	30.5	270	13.0	17.8	1432	103	0.75	1.41	1629	4.73
	Perthite (n-6)	Mean	60852	2009	22299	3340	5.22	48.0	14.9	83.7	8117	24.2	16.0	292	62.5	1.56	2.12	103	91.5
		St dev	17705	407	4001	501	3.50	26.9	5.13	30.6	1685	18.2	6.55	58.4	16.5	2.67	1.47	26.7	188
		Min	40827	1207	14682	2292	2.11	17.6	7.88	52.1	6409	6.14	8.85	201	43.3	0.28	0.67	71.9	0.25
		Max	97794	2457	26825	3856	11.1	99.0	21.8	146	11415	59.3	28.9	388	93.6	7.54	4.59	154	512

			Ce	Pr	Nd	Sm	Eu	Gd	Tb	Dy	Ho	Er	Tm	Yb	Lu	Pb206	Pb207	Pb208	ΣREY
ML07	Albite (n-1)	Mean	0.19	0.18	0.98	1.06	0.21	0.94	0.13	0.54	0.14	0.38	0.12	0.45	0.09	0.08	2.84	1.60	6.11
		St dev	0.00	0.00	0.00	0.00	0.00	0.00	0.00	0.00	0.00	0.00	0.00	0.00	0.00	0.00	0.00	0.00	0.00
		Min	0.19	0.18	0.98	1.06	0.21	0.94	0.13	0.54	0.14	0.38	0.12	0.45	0.09	0.08	2.84	1.60	6.11
		Max	0.19	0.18	0.98	1.06	0.21	0.94	0.13	0.54	0.14	0.38	0.12	0.45	0.09	0.08	2.84	1.60	6.11
	Microcline (n-5)	Mean	0.47	0.16	0.96	1.09	0.55	0.99	0.12	0.56	0.13	0.43	0.13	0.59	0.12	86.6	113	116	8.30
		St dev	0.25	0.02	0.22	0.23	0.24	0.14	0.03	0.10	0.02	0.07	0.02	0.20	0.03	11.5	14.4	31.2	2.96
		Min	0.17	0.14	0.69	0.80	0.23	0.79	0.09	0.43	0.10	0.35	0.10	0.42	0.08	71.6	102	85.5	6.04
		Max	0.84	0.19	1.34	1.50	0.97	1.21	0.16	0.72	0.16	0.56	0.17	0.96	0.16	101	141	157	14.1
	Perthite (n-6)	Mean	152	0.11	0.65	0.80	0.18	0.61	0.08	0.36	0.09	0.28	0.08	0.32	0.10	5.37	1.62	2.89	12.2
		St dev	338	0.01	0.08	0.17	0.04	0.10	0.01	0.05	0.01	0.04	0.02	0.05	0.05	1.04	0.46	0.74	13.8
		Min	0.16	0.09	0.53	0.65	0.11	0.43	0.06	0.28	0.07	0.21	0.05	0.22	0.06	4.31	0.76	2.25	4.16
		Max	907	0.12	0.75	1.14	0.21	0.72	0.10	0.42	0.11	0.34	0.10	0.38	0.19	7.46	2.13	4.43	39.7

Table 4 cont. Summary of LA-ICP-MS trace element data for feldspar (ppm).

			Na	Mg	K	Ca	Sc	Ti	V	Mn	Fe	Cu	Zn	Rb	Sr	Y	Zr	Ba	La
ML09	Albite (n-3)	Mean	117325	1104	12579	2362	8.41	55.6	7.60	39.9	3069	12.4	9.53	107	36.5	0.75	1.69	77.4	0.24
		St dev	66369	679	9430	1521	3.52	32.3	4.82	41.3	1986	10.8	7.30	84.5	23.5	0.87	0.96	12.5	0.19
		Min	47592	254	3610	369	5.02	12.0	1.11	10.2	661	4.32	3.93	20.3	15.1	0.08	0.50	59.9	0.07
		Max	206598	1916	25610	4060	13.3	89.5	12.7	98.2	5523	27.8	19.9	222	69.2	1.98	2.85	88.5	0.50
	Microcline (n-11)	Mean	10961	280	186318	4094	5.79	25.3	0.81	11.2	321	4.64	5.24	860	75.6	0.32	0.75	927	1.96
		St dev	13580	761	74843	1946	1.15	26.0	4.83	36.2	2134	10.0	6.95	334	33.6	0.10	0.97	375	0.78
		Min	1266	4.65	114405	468	2.94	13.7	0.10	3.73	114	0.74	0.77	426	16.5	0.09	0.15	553	0.10
		Max	23337	2877	341884	8091	12.2	54.4	1.54	55.7	1245	9.00	9.32	1250	131	1.17	2.96	1178	14.1
	Perthite (n-4)	Mean	63396	1448	44083	3350	8.57	113	11.5	35.5	5037	9.86	9.94	441	41.2	0.30	0.84	314	0.43
		St dev	40053	916	40628	1760	2.01	77.2	9.07	31.0	3837	5.26	4.58	327	30.7	0.07	0.40	313	0.36
		Min	23153	12.2	12212	963	6.01	24.2	1.60	5.64	179	4.77	5.55	132	10.2	0.23	0.42	103	0.08
		Max	130085	2398	113645	5917	11.6	193	26.3	87.4	10619	18.3	16.8	975	90.3	0.39	1.49	856	0.93

			Ce	Pr	Nd	Sm	Eu	Gd	Tb	Dy	Ho	Er	Tm	Yb	Lu	Pb206	Pb207	Pb208	ΣREY
ML09	Albite (n-3)	Mean	0.47	0.06	0.35	0.35	0.09	0.31	0.04	0.22	0.05	0.17	0.06	0.22	0.05	4.09	1.78	2.02	3.43
		St dev	0.47	0.02	0.13	0.08	0.02	0.17	0.00	0.04	0.01	0.04	0.01	0.05	0.01	1.21	0.85	0.72	2.05
		Min	0.07	0.04	0.23	0.25	0.06	0.09	0.04	0.18	0.04	0.13	0.04	0.19	0.04	2.73	0.61	1.14	1.79
		Max	1.13	0.09	0.53	0.43	0.12	0.51	0.05	0.28	0.06	0.22	0.07	0.29	0.07	5.68	2.62	2.90	6.32
	Microcline (n-11)	Mean	0.63	0.11	0.46	0.52	0.50	0.49	0.08	0.35	0.07	0.23	0.07	0.29	0.07	115	132	124	6.15
		St dev	0.35	0.08	0.14	0.16	0.27	0.12	0.02	0.18	0.02	0.08	0.01	0.07	0.02	54.4	64.7	67.6	4.47
		Min	0.09	0.03	0.24	0.31	0.13	0.32	0.04	0.19	0.05	0.13	0.04	0.19	0.04	9.12	10.7	10.6	2.83
		Max	1.31	0.34	0.75	0.86	0.91	0.73	0.12	0.88	0.11	0.39	0.10	0.44	0.11	205	244	251	19.8
	Perthite (n-4)	Mean	0.32	0.12	0.44	0.45	0.14	0.44	0.07	0.28	0.07	0.44	0.07	0.29	0.07	35.7	30.4	29.7	3.90
		St dev	0.36	0.02	0.21	0.16	0.06	0.25	0.03	0.11	0.03	0.44	0.03	0.11	0.02	54.2	50.0	47.5	1.67
		Min	0.07	0.08	0.21	0.29	0.07	0.12	0.04	0.17	0.04	0.14	0.04	0.17	0.04	3.08	0.54	1.88	2.75
		Max	0.93	0.14	0.77	0.70	0.24	0.83	0.12	0.46	0.12	1.19	0.12	0.47	0.10	130	117	112	6.77

			Na	Mg	K	Ca	Sc	Ti	V	Mn	Fe	Cu	Zn	Rb	Sr	Y	Zr	Ba	La
ML15	Albite (n-3)	Mean	106548	171	1316	7604	4.50	22.1	1.65	47.5	5163	15.3	15.8	2.58	24.3	0.73	1.36	25.2	0.26
		St dev	15750	202	1082	2825	0.59	3.60	0.21	40.7	6270	2.73	2.31	1.86	3.12	0.08	0.20	4.87	0.03
		Min	92357	11.7	479	5410	3.67	19.0	1.37	6.59	230	11.8	13.4	1.03	19.9	0.64	1.13	20.6	0.23
		Max	128511	456	2843	11593	4.99	27.1	1.89	103	14010	18.5	19.0	5.20	27.1	0.83	1.63	31.9	0.29
	Microcline (n-7)	Mean	4663	248	214404	5817	4.80	22.9	1.85	10.2	566	16.7	18.3	482	88.0	0.79	1.62	1914	0.28
		St dev	4225	584	30005	780	0.67	4.37	0.17	5.17	456	1.51	5.35	45.9	61.3	0.11	0.32	622	0.04
		Min	1620	3.47	166785	4498	3.95	18.1	1.57	5.52	225	13.9	12.3	412	23.7	0.62	1.40	828	0.21
		Max	14868	1678	264612	6671	5.59	30.7	2.02	18.6	1545	18.5	30.4	550	198	0.88	2.37	2572	0.32
	Perthite (n-4)	Mean	108908	663	31151	3301	7.85	16.0	1.02	10.7	2808	7.00	7.00	93.3	41.5	0.38	0.91	525	0.15
		St dev	6550	645	12673	1850	4.68	10.9	0.60	5.49	2136	5.98	6.17	60.4	9.06	0.27	0.43	259	0.09
		Min	102399	13.1	18344	665	3.95	3.68	0.12	5.17	330	0.88	0.79	32.2	30.2	0.10	0.18	185	0.06
		Max	117861	1407	47137	5419	15.8	27.6	1.71	18.8	6224	13.6	14.5	168	54.7	0.71	1.30	798	0.29

Table 4 cont. Summary of LA-ICP-MS trace element data for feldspar (ppm).

			Ce	Pr	Nd	Sm	Eu	Gd	Tb	Dy	Ho	Er	Tm	Yb	Lu	Pb206	Pb207	Pb208	ΣREY
ML15	Albite (n-3)	Mean	0.26	0.21	1.21	1.41	0.34	1.30	0.18	0.75	0.16	0.49	0.15	0.71	0.22	1.48	1.08	1.35	8.37
		St dev	0.04	0.05	0.19	0.15	0.06	0.20	0.03	0.12	0.03	0.12	0.01	0.07	0.02	0.50	0.14	0.53	1.09
		Min	0.21	0.17	0.98	1.24	0.25	1.12	0.15	0.59	0.12	0.34	0.14	0.61	0.19	1.02	0.89	0.70	7.08
		Max	0.30	0.28	1.44	1.61	0.38	1.59	0.22	0.88	0.20	0.63	0.16	0.78	0.24	2.18	1.22	2.01	9.75
	Microcline (n-7)	Mean	0.32	0.23	1.32	1.62	0.46	1.44	0.25	0.83	0.19	0.61	0.16	0.71	0.21	78.1	84.6	92.3	9.42
		St dev	0.08	0.03	0.14	0.24	0.17	0.21	0.16	0.10	0.03	0.23	0.02	0.09	0.03	58.6	65.1	80.0	1.06
		Min	0.22	0.19	1.01	1.30	0.29	0.98	0.14	0.66	0.13	0.38	0.13	0.59	0.15	12.3	13.5	11.5	7.29
		Max	0.50	0.27	1.47	2.00	0.87	1.68	0.65	0.98	0.22	1.15	0.18	0.87	0.24	159	181	238	10.8
	Perthite (n-4)	Mean	0.14	0.12	0.80	0.92	0.19	0.75	0.10	0.52	0.10	0.31	0.10	0.40	0.11	18.9	22.2	20.3	5.08
		St dev	0.08	0.07	0.32	0.51	0.09	0.35	0.05	0.28	0.05	0.12	0.04	0.16	0.06	9.54	10.9	9.22	2.43
		Min	0.05	0.04	0.36	0.40	0.09	0.36	0.05	0.23	0.05	0.18	0.05	0.22	0.06	4.36	4.37	6.11	2.59
		Max	0.23	0.19	1.20	1.59	0.29	1.25	0.16	0.95	0.17	0.45	0.14	0.57	0.20	29.5	33.0	31.5	8.00
			Na	Mg	K	Ca	Sc	Ti	V	Mn	Fe	Cu	Zn	Rb	Sr	Y	Zr	Ba	La
MV02	Albite (n-10)	Mean	94603	1040	2734	25991	7.24	323	0.94	80.8	4180	6.49	70.2	8.35	93.4	4.54	33.8	91.3	0.84
		St dev	15420	2049	3905	58514	3.32	894	0.71	167	8606	6.86	166	19.3	32.6	12.1	97.8	200	2.11
		Min	69542	1.07	500	699	4.60	6.59	0.11	0.99	157	0.72	0.77	0.16	53.7	0.11	0.19	3.39	0.05
		Max	128633	5656	13344	201021	15.2	3005	2.07	574	28088	24.6	566	66	153	40.9	327	690	7.15
	Microcline (n-10)	Mean	28805	356	145038	4163	6.75	17.8	0.89	32.1	701	8.03	11.5	449	136	0.61	1.64	3866	0.82
		St dev	33714	648	88918	3056	3.43	8.04	0.64	40.2	567	8.92	11.0	209	54.6	0.83	2.07	1645	1.28
		Min	2184	0.90	1363	505	4.10	6.37	0.12	1.01	159	0.85	2.06	2.45	41.7	0.15	0.17	28.27	0.06
		Max	117560	1660	295808	7873	16.8	30.1	1.76	131	1876	32.9	40.9	737	211	3.02	7.22	5380	3.60
	Perthite (n-4)	Mean	47902	6.93	82222	3380	5.60	8.47	0.13	17.3	137	0.72	2.90	266	96.7	0.98	0.16	2373	0.06
		St dev	0.00	0.00	0.00	0.00	0.00	0.00	0.00	0.00	0.00	0.00	0.00	0.00	0.00	0.00	0.00	0.00	0.00
		Min	47902	6.93	82222	3380	5.60	8.47	0.13	17.3	137	0.72	2.90	266	96.7	0.98	0.16	2373	0.06
		Max	47902	6.93	82222	3380	5.60	8.47	0.13	17.3	137	0.72	2.90	266	96.7	0.98	0.16	2373	0.06
			Ce	Pr	Nd	Sm	Eu	Gd	Tb	Dy	Ho	Er	Tm	Yb	Lu	Pb206	Pb207	Pb208	ΣREY
MV02	Albite (n-10)	Mean	2.63	0.32	1.67	0.77	0.13	0.98	0.16	0.93	0.15	0.49	0.11	0.65	0.12	6.47	6.80	6.74	14.5
		St dev	7.27	0.76	3.55	0.89	0.05	1.54	0.28	1.96	0.26	0.80	0.13	1.00	0.14	2.39	2.55	2.27	32.8
		Min	0.04	0.04	0.29	0.31	0.06	0.30	0.05	0.19	0.05	0.15	0.05	0.19	0.05	3.75	4.43	4.43	2.39
		Max	24.4	2.61	12.31	3.42	0.21	5.58	1.01	6.80	0.93	2.89	0.49	3.64	0.53	11.8	11.9	11.4	113
	Microcline (n-10)	Mean	0.24	0.14	0.67	0.49	0.34	0.57	0.09	0.35	0.07	0.25	0.06	0.28	0.08	42.7	43.6	42.3	5.06
		St dev	0.38	0.18	0.76	0.15	0.18	0.31	0.05	0.21	0.02	0.13	0.02	0.09	0.03	28.4	28.2	24.9	3.55
		Min	0.04	0.04	0.22	0.33	0.11	0.29	0.04	0.18	0.05	0.15	0.04	0.20	0.05	6.72	5.33	8.50	2.59
		Max	1.35	0.67	2.90	0.80	0.56	1.35	0.21	0.94	0.10	0.59	0.09	0.52	0.16	89.1	88.3	80.9	15.1
	Perthite (n-4)	Mean	0.05	0.04	0.25	0.35	0.19	0.31	0.05	0.21	0.05	0.16	0.05	0.20	0.05	42.9	46.4	46.4	3.00
		St dev	0.00	0.00	0.00	0.00	0.00	0.00	0.00	0.00	0.00	0.00	0.00	0.00	0.00	0.00	0.00	0.00	0.00
		Min	0.05	0.04	0.25	0.35	0.19	0.31	0.05	0.21	0.05	0.16	0.05	0.20	0.05	42.9	46.4	46.4	3.00
		Max	0.05	0.04	0.25	0.35	0.19	0.31	0.05	0.21	0.05	0.16	0.05	0.20	0.05	42.9	46.4	46.4	3.00

Table 5 Summary of LA-ICP-MS trace element data for rutile (ppm).

ML06 (n-7)		Na	Mg	Al	P	K	Sc	V	Cr	Mn	Fe	Co	Cu	Zn	Rb	Sr	Y	Zr	Nb	Mo	Sn	Sb	Ba
	mean	1987	2369	6061	20.4	3105	186	455	538	1599	10500	1.16	29.0	36.2	38.9	10.8	34.0	13.7	1009	0.72	128	28.3	24.2
	std. dev.	2944	2116	4692	11.6	2369	44.9	96.2	194	2708	5394	1.08	4.90	12.4	30.4	3.81	6.38	5.11	303	0.54	49.9	11.4	11.0
	min	141	797	564	9.86	252	129	267	171	43.7	6085	0.22	23.4	27.3	3.13	7.51	21.8	7.37	651	0.33	62.3	11.6	12.1
	max	8854	7095	12133	39.0	6146	255	571	755	8072	22756	3.51	38.5	65.5	81.3	19.5	43.7	20.7	1438	2.00	228	52.6	39.0
		La	Ce	Pr	Nd	Sm	Eu	Gd	Tb	Dy	Ho	Er	Tm	Yb	Lu	Ta	W	^{206}Pb	^{207}Pb	^{208}Pb	Th	U	ΣREY
	mean	18.9	35.7	4.11	14.8	3.73	1.24	5.42	1.11	7.99	1.87	5.97	0.97	6.64	0.92	287	972	96.2	81.0	78.4	5.19	11.0	143
	std. dev.	4.41	7.14	0.88	3.0	0.72	0.25	1.27	0.27	1.58	0.34	1.17	0.23	1.60	0.24	66.9	389	102.9	94.3	86.7	1.29	6.12	28.7
	min	11.12	22.12	2.52	9.43	2.74	0.79	3.20	0.66	5.54	1.18	3.69	0.58	3.88	0.57	203	330	38.9	38.7	32.6	2.98	5.50	89.8
	max	25.6	45.4	5.42	19.2	4.99	1.55	6.95	1.44	10.7	2.34	7.81	1.39	9.15	1.32	373	1553	347	312	290	7.02	20.3	186
ML16 (n-11)		Na	Mg	Al	P	K	Sc	V	Cr	Mn	Fe	Co	Cu	Zn	Rb	Sr	Y	Zr	Nb	Mo	Sn	Sb	Ba
	mean	*	*	*	*	*	*	238	*	830	35476	*	763	82.7	3.34	7.79	9.33	18.4	2407	*	17.8	219	43.6
	std. dev.							37.1		655	23258		1789	34.1	3.77	2.65	6.25	5.96	1005		8.85	142	17.3
	min							169		57.9	10095		46.7	33.5	0.61	4.58	0.82	7.59	860		3.35	39.6	20.6
	max							315		2140	100501		6364	156	13.1	13.3	18.8	32.4	4064		36.3	464	78.4
		La	Ce	Pr	Nd	Sm	Eu	Gd	Tb	Dy	Ho	Er	Tm	Yb	Lu	Ta	W	^{206}Pb	^{207}Pb	^{208}Pb	Th	U	ΣREY
	mean	9.15	22.6	2.59	9.35	1.89	0.76	2.04	0.31	2.05	0.43	1.31	0.18	1.03	0.19	538	33.9	34.3	25.7	21.7	1.10	4.80	63.2
	std. dev.	5.53	14.4	1.65	6.12	1.34	0.55	1.46	0.22	1.36	0.26	0.77	0.10	0.63	0.10	606	26.1	41.0	33.1	23.9	0.98	1.23	39.8
	min	1.73	4.42	0.64	2.34	0.19	0.11	0.21	0.02	0.27	0.06	0.12	0.04	0.17	0.04	82.4	5.32	11.2	7.77	5.76	0.08	3.16	11.7
	max	19.0	47.8	5.31	19.8	3.91	1.74	4.52	0.63	4.25	0.85	2.40	0.37	2.09	0.36	2250	81.3	160	130	95.5	3.19	6.92	131
PS03 (n-6)		Na	Mg	Al	P	K	Sc	V	Cr	Mn	Fe	Co	Cu	Zn	Rb	Sr	Y	Zr	Nb	Mo	Sn	Sb	Ba
	mean	2958	9961	28680	1716	12684	558	258	77.2	306	16189	4.10	17.7	69.3	21.6	47.2	148	248	697	0.68	3.78	33.2	102
	std. dev.	1752	11437	28715	1904	12364	265	224	74.0	306	14725	3.30	8.74	24.8	22.0	77.0	260	279	312	0.84	1.98	51.6	129
	min	811	245	635	479	162	140.5	66.3	22.6	21.7	1607	0.85	5.88	38.5	1.27	1.00	0.76	38.8	322	0.11	1.26	0.99	7.32
	max	5313	31959	71731	5909	31745	938	615	220	747	36377	9.67	30.6	105	63.9	217	719	776	1213	2.38	7.35	147	372
		La	Ce	Pr	Nd	Sm	Eu	Gd	Tb	Dy	Ho	Er	Tm	Yb	Lu	Ta	W	^{206}Pb	^{207}Pb	^{208}Pb	Th	U	ΣREY
	mean	76.3	138	16.5	66.7	16.9	8.54	33.8	5.76	41.3	8.20	23.5	2.78	16.4	2.26	46.3	141	54.8	45.5	47.0	60.7	17.1	606
	std. dev.	122	216	26.7	110	27.1	14.8	57.7	10.1	72.1	14.4	41.8	4.84	28.5	3.84	18.7	109	70.5	61.6	62.2	102	26.2	1009
	min	0.25	0.31	0.11	0.25	0.14	0.03	0.10	0.02	0.22	0.03	0.05	0.02	0.09	0.01	30.9	44.3	6.18	6.13	6.15	0.40	0.58	2.39
	max	342	610	75.0	308	76	41.2	160	28.1	200	40.0	116	13.4	79.1	10.7	87	332	207	178	180	283	73.5	2819
PS07 (n-4)		Na	Mg	Al	P	K	Sc	V	Cr	Mn	Fe	Co	Cu	Zn	Rb	Sr	Y	Zr	Nb	Mo	Sn	Sb	Ba
	mean	*	30194	106886	*	40576	119	259	108	680	72466	25.9	189	218	156	64.6	86.1	457	480	*	10.2	22.2	1314
	std. dev.		14626	66804		28457	37.2	124	48.7	210	35046	14.4	101	93.5	101.6	17.7	43.1	396	140		6.14	10.4	965
	min		6381	16607		5354	83.9	60.1	59.3	329	18894	10.9	85.6	93.0	14.6	38.9	46.9	86	377		4.63	7.71	140
	max		44797	184970		73285	181	377	171	866	113258	49.1	356	345	255	88.7	159	1123	721		20.5	32.8	2552
		La	Ce	Pr	Nd	Sm	Eu	Gd	Tb	Dy	Ho	Er	Tm	Yb	Lu	Ta	W	^{206}Pb	^{207}Pb	^{208}Pb	Th	U	ΣREY
	mean	52.2	147	15.4	57.4	13.9	4.76	17.2	3.00	20.3	4.04	12.2	1.90	13.3	1.67	40.9	133	114	102.7	100	53.7	32.5	450
	std. dev.	50.4	146	13.5	43.9	7.22	2.31	6.07	1.01	6.13	1.34	3.96	0.68	4.86	0.74	14.2	20.0	53.9	66.3	60.5	27.5	17.2	260
	min	5.02	23.2	3.71	13.9	6.43	1.12	8.02	1.83	13.3	2.66	8.30	1.34	9.14	1.13	26.3	112	55.5	50.6	48.1	16.3	9.90	146
	max	133	392	37.7	128	25.9	7.24	24.6	4.59	30.1	6.25	18.8	3.07	21.6	2.94	61.1	162	184	216	201	83.3	54.0	864

Table 5 cont. Summary of LA-ICP-MS trace element data for rutile (ppm).

		Na	Mg	Al	P	K	Sc	V	Cr	Mn	Fe	Co	Cu	Zn	Rb	Sr	Y	Zr	Nb	Mo	Sn	Sb	Ba
MV01 (n-4)	**mean**	301	2027	11755	179	6151	31.3	4.43	*	16541	25077	0.36	8.65	98.1	30.5	40.8	940	89.8	4762	3.11	118	4.97	213
	std. dev.	327	1301	2884	220	2091	10.4	1.53		5473	6464	0.17	1.32	36.6	12.4	8.88	779	73.0	570	3.78	27.9	1.92	80.0
	min	65.2	419	7389	29.6	2530	16.5	2.55		9630	18461	0.12	6.90	51.9	12.7	29.0	203	27.1	3925	0.54	75.4	3.59	97.7
	max	859	3811	15438	557	7449	42.9	6.34		24951	34788	0.57	10.0	153	47.8	50.1	2158	205	5420	9.64	150	8.27	322
		La	**Ce**	**Pr**	**Nd**	**Sm**	**Eu**	**Gd**	**Tb**	**Dy**	**Ho**	**Er**	**Tm**	**Yb**	**Lu**	**Ta**	**W**	**^{206}Pb**	**^{207}Pb**	**^{208}Pb**	**Th**	**U**	**ΣREY**
	mean	1808	3156	354	1441	250	34.6	261	31.3	153	25.1	58.6	7.94	46.9	6.99	120	299	88.9	90.0	87.4	23.2	10.8	8573
	std. dev.	1885	3235	375	1504	235	30.6	231	22.8	94.3	13.6	27.4	3.45	20.8	3.28	27.7	50.7	10.6	9.66	11.9	3.87	4.06	8444
	min	45.1	111	14.3	72.4	31.1	5.98	47.1	9.53	60.7	11.0	27.6	3.48	19.8	2.62	82.1	214	74.6	76.0	69.5	19.2	3.74	694
	max	4530	7772	918	3709	593	80.2	604	64.8	289	43.6	91.9	11.6	67.4	10.8	155	349	102	101	100	27.7	13.4	20941
		Na	**Mg**	**Al**	**P**	**K**	**Sc**	**V**	**Cr**	**Mn**	**Fe**	**Co**	**Cu**	**Zn**	**Rb**	**Sr**	**Y**	**Zr**	**Nb**	**Mo**	**Sn**	**Sb**	**Ba**
MV02 (n-4)	**mean**	437	14900	38331	356	6766	128	6.41	*	8563	386838	7.43	45.7	451	66.8	29.8	551	1952	6883	9.34	277	4.47	149
	std. dev.	289	11390	23364	249	4643	42.9	0.39		2314	164317	4.29	7.14	206	31.3	3.45	504	1917	800	7.30	147	1.81	107
	min	154	2708	12099	139	422	63.4	5.88		6903	239858	3.35	34.2	243	13.8	24.6	145	567	5856	3.71	149	2.64	24.8
	max	917	30497	71822	747	13030	173	6.96		12552	659108	13.5	53.7	736	91.1	33.2	1413	5246	8102	21.9	523	7.29	313
		La	**Ce**	**Pr**	**Nd**	**Sm**	**Eu**	**Gd**	**Tb**	**Dy**	**Ho**	**Er**	**Tm**	**Yb**	**Lu**	**Ta**	**W**	**^{206}Pb**	**^{207}Pb**	**^{208}Pb**	**Th**	**U**	**ΣREY**
	mean	56.4	106	12.7	207	19.1	4.98	37.2	10.5	82.0	18.9	56.6	7.85	50.3	7.31	253	1358	153	145	140	118	50.5	1228
	std. dev.	38.9	80.1	8.21	281	8.22	2.01	18.1	5.79	50.2	12.6	37.4	4.84	31.5	4.33	42.5	167	26.6	42.0	4.69	94.8	24.6	837
	min	17.2	38.0	4.77	22.5	9.72	2.54	16.2	4.30	30.8	7.77	19.5	2.53	17.6	2.87	208	1070	111	93.7	135	34.0	22.7	346
	max	111	234	24.9	692	27.9	7.36	62.5	19.5	163	40.1	118	15.6	102	14.5	297	1469	183	206	148	276	86.9	2441

* = 95% below detection limit. The Si content was negligible so it is not included. Ti was removed because it was used as the internal standard.

Table 6 Summary of LA-ICP-MS trace element data for apatite (ppm).

Sample		Na	Mg	Al	Si	P	K	Sc	^{49}Ti	V	Cr	Mn	Fe	Co	Ni	Cu	Zn	As	Rb	Sr	Y	Zr	Nb	Mo	Sn
ML04 (n-11)	**mean**	598	76.7	25.5	747	193117	*	0.67	*	1.83	*	2381	244	0.62	*	*	4.97	22.0	*	99.4	1607	0.22	*	*	*
	std. dev.	246	44.6	41.1	614	5304		0.33		1.54		777	122	0.28			5.36	14.7		8.20	457	0.14			
	min	33.4	15.9	1.22	142	183889		0.23		0.59		1070	39.8	0.08			0.42	8.53		87.7	766	0.06			
	max	884	159	148	2281	201572		1.17		6.13		3414	441	1.17			19.4	63.8		113	2380	0.54			
		Sb	**Ba**	**La**	**Ce**	**Pr**	**Nd**	**Sm**	**Eu**	**Gd**	**Tb**	**Dy**	**Ho**	**Er**	**Tm**	**Yb**	**Lu**	**Ta**	**W**	**^{206}Pb**	**^{207}Pb**	**^{208}Pb**	**Th**	**U**	**ΣREY**
	mean	*	*	148	502	89.4	477	194	29.9	279	51.9	333	60.3	154	19.4	111	13.6	*	*	25.8	6.07	3.85	3.94	18.4	4069
	std. dev.			47.4	140	24.1	115	49.8	7.70	73.2	14.0	95.2	17.5	47.2	6.65	40.4	5.00			19.1	2.81	1.19	4.20	15.9	1155
	min			53.8	221	40.0	247	103	15.4	158	28.1	172	29.9	69.8	7.67	37.8	4.05			3.58	2.28	1.30	0.29	1.78	1954
	max			237	767	135	659	278	45.8	417	77.3	497	89.8	236	32.6	193	23.7			66.8	12.7	5.31	11.4	51.1	6039
ML06 (n-2)		**Na**	**Mg**	**Al**	**Si**	**P**	**K**	**Sc**	**Ti**	**V**	**Cr**	**Mn**	**Fe**	**Co**	**Ni**	**Cu**	**Zn**	**As**	**Rb**	**Sr**	**Y**	**Zr**	**Nb**	**Mo**	**Sn**
	mean	4047	3971	866	14893	186722	1404	1.15	472	26.4	5.2	992	591	1.25	3.22	23.2	62.4	44.2	32.5	63.8	589	4.83	0.3	0.24	*
	std. dev.	1944	2097	523	8109	50190	685	0.67	47.5	25.6	1.9	244	33.1	0.24	2.53	13.7	21.4	23.0	29.5	18.8	359	2.87	0.1	0.02	
	min	2103	1874	344	6785	136531	720	0.48	424	0.77	3.36	748	558	1.01	0.69	9.46	41.0	21.2	3.02	45.1	230	1.96	0.21	0.22	
	max	5991	6068	1389	23002	236912	2089	1.81	519	51.9	7.1	1236	624	1.49	5.75	36.9	83.8	67.2	62.0	82.6	947	7.70	0.3	0.27	
		Sb	**Ba**	**La**	**Ce**	**Pr**	**Nd**	**Sm**	**Eu**	**Gd**	**Tb**	**Dy**	**Ho**	**Er**	**Tm**	**Yb**	**Lu**	**Ta**	**W**	**^{206}Pb**	**^{207}Pb**	**^{208}Pb**	**Th**	**U**	**ΣREY**
	mean	0.34	26.8	184	309	52.3	218	78	10.5	115	22.7	155	28.6	68	8.2	50.2	5.49	0.09	1.05	185	165	127.6	2.45	9.4	1894
	std. dev.	0.15	13.5	106.2	55	8.9	78	33	3.79	47	10.7	66	12.2	28.8	3.13	19.7	2.61	0.02	0.73	151	143	102.4	0.84	1.9	878
	min	0.19	13.3	77.7	254	43.4	141	45.5	6.70	67.3	12.0	88.8	16.4	39.0	5.02	30.6	2.88	0.07	0.32	33.9	22.0	25.2	1.61	7.44	1273
	max	0.49	40.3	290	364	61	296	111	14.3	162	33.4	221	40.7	97	11.3	70	8.1	0.1	1.77	335	309	230	3.3	11.3	2515
ML10 (n-5)		**Na**	**Mg**	**Al**	**Si**	**P**	**K**	**Sc**	**^{49}Ti**	**V**	**Cr**	**Mn**	**Fe**	**Co**	**Ni**	**Cu**	**Zn**	**As**	**Rb**	**Sr**	**Y**	**Zr**	**Nb**	**Mo**	**Sn**
	mean	723	955	2767	27034	193876	676	9.55	662	2.61	3.53	524	12872	3.28	*	4584	21.2	69.8	6.20	91.7	2881	3829	68.2	6.91	1.46
	std. dev.	373	765	1996	25728	7654	775	9.77	1164	1.87	1.46	137	14239	2.89		4327	24.3	53.2	5.04	25.4	2030	3531	65.3	8.79	1.24
	min	245	16.6	24.4	145	179574	38.7	0.29	7.04	0.15	1.33	323	88.3	0.16		5.02	4.87	11.0	0.71	59.0	885	0.07	0.06	0.22	0.43
	max	1141	1739	5965	67226	199948	2202	27.0	2983	4.66	5.40	644	39047	7.94		11582	68.6	154	15.5	122	6602	9295	152	23.8	3.77
		Sb	**Ba**	**La**	**Ce**	**Pr**	**Nd**	**Sm**	**Eu**	**Gd**	**Tb**	**Dy**	**Ho**	**Er**	**Tm**	**Yb**	**Lu**	**Ta**	**W**	**^{206}Pb**	**^{207}Pb**	**^{208}Pb**	**Th**	**U**	**ΣREY**
	mean	30.4	25.4	321	1005	163	793	317	35.2	474	83.9	551	103	265	35.8	221	28.2	0.80	24.4	522	65.9	192	16412	9391	7276
	std. dev.	28.1	16.3	240	750	125	611	262	24.7	391	72.4	483	91.4	243	33.1	215	26.1	0.92	24.7	510	61.3	172	17397	15063	6096
	min	0.12	0.66	48.6	140	24.5	139	66	12.9	109	18.1	119	22.6	57.3	7.03	41.2	5.63	0.02	0.08	5.37	5.14	5.62	0.58	0.12	1772
	max	72.5	51.0	630	2027	358	1793	784	80.5	1188	219	1458	276	728	98.3	632	77.7	2.38	66.7	1384	170	432	46684	39323	16857
ML16 (n-9)		**Na**	**Mg**	**Al**	**Si**	**P**	**K**	**Sc**	**Ti**	**V**	**Cr**	**Mn**	**Fe**	**Co**	**Ni**	**Cu**	**Zn**	**As**	**Rb**	**Sr**	**Y**	**Zr**	**Nb**	**Mo**	**Sn**
	mean	7093	1643	7109	43954	327465	2662	*	1242	18.0	*	815	2510	*	14.1	*	*	51.0	28.3	510	759	17.2	0.56	*	3.23
	std. dev.	1808	1920	5866	19130	113821	2419		558	9.45		548	2013		9.30			25.5	26.2	82.4	208	11.3	0.93		4.26
	min	4795	91.6	756	26183	196756	509		609	6.07		438	435		4.45			12.9	3.61	442	515	6.43	0.09		0.29
	max	10461	6094	19248	87766	573063	8598		2263	32.8		2302	6067		35.5			96.5	93.4	656	1226	39.8	3.07		14.1

Table 6 Summary of LA-ICP-MS trace element data for apatite (ppm).

		Sb	Ba	La	Ce	Pr	Nd	Sm	Eu	Gd	Tb	Dy	Ho	Er	Tm	Yb	Lu	Ta	W	^{206}Pb	^{207}Pb	^{208}Pb	Th	U	ΣREY
ML16	mean	0.61	33.7	513	1381	181	828	195	34.2	201	28.1	156	29.4	70.0	8.12	48.2	6.59	0.05	3.50	29.9	21.7	21.8	15.8	6.41	4438
	std. dev.	0.46	20.1	166	423	59.9	255	57.2	8.34	51.5	7.80	42.6	7.51	17.9	1.98	12.6	1.37	0.08	2.13	15.4	9.72	7.53	5.72	3.25	1390
	min	0.10	10.5	324	851	107	504	118	21.4	129	17.8	98.9	19.8	45.2	5.39	30.9	4.73	0.00	1.47	18.0	13.7	13.6	11.0	3.36	2793
	max	1.39	76.4	881	2378	323	1407	321	53.0	313	45.8	253	46.3	109	12.6	74.5	9.23	0.27	8.56	67.2	45.4	34.6	30.5	15.2	7454
PS07 (n-4)		Na	Mg	Al	Si	P	K	Sc	Ti	V	Cr	Mn	Fe	Co	Ni	Cu	Zn	As	Rb	Sr	Y	Zr	Nb	Mo	Sn
	mean	5577	31647	39218	110344	133368	2345	69.6	670	43.3	136	704	*	8.40	51.5	37.4	121	12.5	7.20	2684	446	35.6	0.30	0.59	1.81
	std. dev.	1123	18940	22179	78666	26091	1110	34.4	128	27.0	49.6	278		5.30	28.4	15.4	77.5	6.18	5.42	756	77.3	46.4	0.16	0.12	0.96
	min	3971	11061	15576	19316	115428	634	45.2	485	6.36	73.3	364		2.64	18.6	20.1	17.4	7.10	0.43	1674	321	0.90	0.09	0.41	0.71
	max	6700	60905	72864	232054	178322	3489	129	832	79.8	196	1134		13.7	91.5	60.3	226	22.7	13.2	3757	524	114	0.50	0.75	3.22
		Sb	Ba	La	Ce	Pr	Nd	Sm	Eu	Gd	Tb	Dy	Ho	Er	Tm	Yb	Lu	Ta	W	^{206}Pb	^{207}Pb	^{208}Pb	Th	U	ΣREY
	mean	0.28	38.1	339	1102	131	555	102	30.3	95.0	14.1	83.8	16.8	37.6	4.45	24.8	3.07	0.02	2.37	21.2	22.1	23.2	14.5	10.2	2986
	std. dev.	0.16	27.6	130	366	43.0	177	25.4	5.37	17.1	2.39	11.2	2.33	5.75	0.73	3.28	0.93	0.01	0.54	7.65	11.4	9.15	2.18	3.94	876
	min	0.07	1.93	161	540	68.7	285	64.2	22.4	72.4	10.7	66.3	13.5	28.2	3.43	19.2	2.13	0.01	1.81	12.2	10.2	12.5	11.4	5.66	1845
	max	0.52	75.7	529	1519	190	778	135	36.0	115	16.7	97.2	20.0	43.6	5.50	27.6	4.57	0.03	3.15	33.3	40.7	36.0	17.1	14.4	3981
MV02 (n-2)		Na	Mg	Al	Si	P	K	Sc	Ti	V	Cr	Mn	Fe	Co	Ni	Cu	Zn	As	Rb	Sr	Y	Zr	Nb	Mo	Sn
	mean	11877	2538	18460	107771	479661	32222	3.67	506	0.44	*	832	6052	0.34	0.47	3.70	19.8	34.1	61.9	221	1323	1489	9.24	0.81	4.99
	std. dev.	6567	2195	11561	90195	4874	30429	0.65	3.58	0.36		251	3823	0.15	0.07	1.37	5.01	5.50	52.2	19.8	616	580	6.84	0.09	0.06
	min	5310	343	6899	17576	474786	1793	3.01	502	0.07		582	2229	0.18	0.40	2.33	14.8	28.6	9.8	202	707	909	2.40	0.72	4.92
	max	18444	4732	30022	197966	484535	62651	4.32	510	0.80		1083	9874	0.49	0.54	5.07	24.8	39.6	114	241	1939	2069	16.1	0.89	5.05
		Sb	Ba	La	Ce	Pr	Nd	Sm	Eu	Gd	Tb	Dy	Ho	Er	Tm	Yb	Lu	Ta	W	^{206}Pb	^{207}Pb	^{208}Pb	Th	U	ΣREY
	mean	0.28	350	250	1114	92.7	465	125	20.4	163	28.2	183	41.4	108	14.5	99.4	14.7	0.51	2.61	30.4	14.8	23.2	361	11.2	4043
	std. dev.	0.06	342	195	899	64.0	307	69.6	2.94	79.5	13.4	83.6	16.9	41.2	5.45	28.6	3.96	0.35	1.37	15.6	6.76	3.24	325	2.14	3431
	min	0.22	7.70	55.2	215	28.7	158	55.7	17.5	83.4	14.8	100	24.5	66.3	9.05	70.7	10.7	0.16	1.24	14.8	8.06	20.0	35.5	9.09	1617
	max	0.34	692	445	2013	157	773	195	23.4	242	41.6	267	58.2	149	19.9	128	18.6	0.86	3.97	46.1	21.6	26.4	686	13.4	6469

* = 95% below detection limit. Ca was removed because it was used as the internal standard. The titanium (Ti) value given is an average of calculated total Ti based on measurement of ^{47}Ti and ^{48}Ti; in ML04 and ML10 the ^{49}Ti measurement is displayed.

Table 7 Summary of LA-ICP-MS trace element data for kutnohorite (Ku), pyrolusite (Pyl) and titanite (Ti) (ppm).

Ku	ML06 (n-7)		Na	Mg	Al	P	K	Ca	Sc	Ti	V	Cr	Mn	Fe	Co	Ni	Cu	Zn	As	Rb	Sr	Y	Zr	Nb	Mo	Sn
		mean	4050	50158	•	•	•	-	3.56	20.6	5.67	*	27704	73844	13.8	6.79	21.7	56.6	0.34	•	73.5	•	0.11	0.26	0.69	2.73
		std. dev.	2955	4255					0.68	4.12	2.40		6436	9069	2.25	1.44	9.15	8.62	0.16		14.8		0.12	0.12	0.38	1.41
		min	662	43536					2.84	16.8	2.51		21243	59413	10.8	5.16	10.3	44.6	0.09		59.2		0.02	0.09	0.32	0.63
		max	8409	57498					4.92	29.1	10.0		40793	87524	17.4	9.02	35.9	69.8	0.61		101		0.37	0.46	1.47	4.73
			Sb	Ba	La	Ce	Pr	Nd	Sm	Eu	Gd	Tb	Dy	Ho	Er	Tm	Yb	Lu	Ta	W	^{206}Pb	^{207}Pb	^{208}Pb	Th	U	ΣREE
		mean	0.28	65.8	2.46	7.39	1.24	6.08	3.85	2.17	6.14	•	7.36	1.47	4.52	•	•	1.14	0.06	0.16	10.1	8.44	10.8	0.07	2.33	208
		std. dev.	0.18	35.5	0.69	1.30	0.20	0.83	0.41	0.22	0.84		0.91	0.20	0.89			0.31	0.03	0.10	2.39	1.49	6.71	0.03	1.51	33.6
		min	0.05	23.1	1.86	5.83	0.92	4.66	3.16	1.83	5.06		6.19	1.22	2.89			0.66	0.02	0.07	5.73	6.21	5.52	0.03	0.97	155
		max	0.59	140	4.04	10.1	1.53	7.10	4.37	2.48	7.45		8.63	1.82	5.89			1.57	0.12	0.36	13.5	10.1	26.8	0.10	5.15	252
	ML16 (n-7)		Na	Mg	Al	P	K	Ca	Sc	Ti	V	Cr	Mn	Fe	Co	Ni	Cu	Zn	As	Rb	Sr	Y	Zr	Nb	Mo	Sn
		mean	26287	51335	•	•	•	-	35.4	64.2	9.31	67.8	10360	76286	18.6	12.8	18.7	29.7	3.97	•	76.2	•	4.43	0.08	0.45	1.36
		std. dev.	14715	9999					10.6	13.8	4.06	31.5	1504	10935	5.19	7.32	5.97	13.5	0.67		17.4		2.61	0.04	0.21	0.31
		min	3404	35686					16.9	38.6	4.64	41.4	7575	61713	7.70	5.46	6.92	10.0	2.90		48.5		1.01	0.03	0.16	0.77
		max	40901	65099					55.3	83.0	15.7	140	12459	95910	24.3	27.6	27.1	54.8	4.96		95.6		8.65	0.15	0.74	1.66
			Sb	Ba	La	Ce	Pr	Nd	Sm	Eu	Gd	Tb	Dy	Ho	Er	Tm	Yb	Lu	Ta	W	^{206}Pb	^{207}Pb	^{208}Pb	Th	U	ΣREE
		mean	0.07	30.5	14.2	35.8	6.81	37.9	15.8	4.17	20.2	•	21.8	4.72	13.3	•	•	1.54	0.02	0.04	9.22	9.89	9.42	0.65	0.20	113
		std. dev.	0.05	11.6	2.74	7.64	1.25	4.88	2.49	0.61	3.06		2.75	0.68	1.82			0.25	0.00	0.01	4.14	4.40	4.34	0.39	0.25	35.9
		min	0.02	9.79	10.0	24.8	4.80	31.2	11.6	3.01	15.1		16.3	3.42	9.61			0.97	0.01	0.02	5.28	6.15	5.76	0.23	0.05	70.5
		max	0.17	47.7	17.3	47.1	8.65	44.8	18.2	4.91	25.0		24.5	5.33	15.1			1.77	0.02	0.07	16.5	17.2	17.6	1.21	0.80	181
Pyl	MV02 (n-9)		Na	Mg	Al	Si	P	K	Ca	Sc	Ti	V	Cr	Fe	Co	Ni	Cu	Zn	As	Rb	Sr	Y	Zr	Nb	Mo	Sn
		mean	3817	19924	460	1056	25.8	32899	6728	6.03	66.9	1.52	*	19571	103	74.8	418	2501	6.45	9.06	4241	2037	212	3.44	187	0.28
		std. dev.	909	5094	41.4	119	2.61	12642	1350	1.11	14.0	0.29		2886	27.5	25.0	41.2	1297	1.36	0.34	664	455	321	0.70	26.8	0.14
		min	2743	11234	365	870	20.1	16754	4341	4.39	49.5	1.19		13653	63.7	36.6	355	1538	3.75	8.56	2997	1209	16.4	2.43	138	0.14
		max	5512	27951	495	1245	29.5	55998	8760	7.93	89.9	1.98		22719	148	116	490	5188	8.36	9.53	5150	2523	1018	4.90	222	0.55
			Sb	Ba	La	Ce	Pr	Nd	Sm	Eu	Gd	Tb	Dy	Ho	Er	Tm	Yb	Lu	Ta	W	^{206}Pb	^{207}Pb	^{208}Pb	Th	U	ΣREY
		mean	0.44	22987	2099	976	210	862	202	37.9	255	43.0	241	47.3	110	12.8	75.6	10.6	0.04	1.84	759	527	671	17.6	12.7	7219
		std. dev.	0.08	2088	334	97.9	36.8	159	31.8	5.43	38.9	5.32	30.3	6.48	16.0	1.78	11.8	1.64	0.02	0.43	331	230	286	2.86	1.78	1144
		min	0.32	19605	1418	779	133	536	136	27.4	185	34.1	191	37.2	87.5	10.3	59.7	8.21	0.02	1.10	167	118	150	13.3	8.72	5112
		max	0.58	25670	2535	1108	253	1053	238	43.9	298	48.7	287	57.2	137	16.1	97.5	13.3	0.07	2.55	1193	815	1047	21.2	14.6	8646
Ti	MV01 (n-8)		Na	Mg	Al	Si	P	K	Ca	Sc	V	Cr	Mn	Fe	Co	Ni	Cu	Zn	As	Rb	Sr	Y	Zr	Nb	Mo	Sn
		mean	888	1865	15449	71660	2479	3709	101953	76.6	3.32	9.42	3118	13674	0.09	0.13	6.21	41.6	3.33	10.6	12.5	3590	279	2130	3.09	260
		std. dev.	1156	2455	3276	23850	7356	6912	20349	27.2	1.18	10.2	2196	10604	0.12	0.04	1.84	64.1	1.71	15.1	8.73	1536	330	351	0.95	40.4
		min	49.3	366	12090	33334	18.4	51.1	63171	45.1	2.01	0.31	1178	6674	0.02	0.08	3.36	4.65	2.01	0.37	3.99	494	25.4	1486	1.81	166
		max	3190	8059	22720	120044	24546	23911	150510	126	5.91	32.1	8622	43456	0.44	0.20	8.74	229	8.26	52.9	29.8	5197	1032	2695	4.62	335
			Sb	Ba	La	Ce	Pr	Nd	Sm	Eu	Gd	Tb	Dy	Ho	Er	Tm	Yb	Lu	Ta	W	^{206}Pb	^{207}Pb	^{208}Pb	Th	U	ΣREY
		mean	5.23	60.1	36.8	169	33.6	223	139	40.9	214	53.8	386	83.8	224	32.0	218	26.9	44.0	6.22	58.9	18.8	21.7	17.5	81.4	5472
		std. dev.	1.32	94.0	24.6	70.2	7.15	52.5	45.1	10.2	78.7	20.1	151	33.7	90.9	12.9	86.5	10.1	13.2	3.69	22.1	8.96	15.1	16.1	79.6	2084
		min	1.92	2.57	13.0	91.1	18.8	93.9	38.1	19.2	48.1	11.7	81.0	16.2	45.0	6.88	52.5	6.95	29.0	3.53	28.3	8.30	5.41	5.93	13.9	1080
		max	6.40	323	87.7	320	43.7	296	207	53.8	312	74.8	547	119	317	45.6	309	38.3	68.3	15.3	97.0	33.8	49.0	53.6	260	7542

* = 95% below detection limit. - = removed because it was used as the internal standard. • = element not present in the standard. The titanium value given is an average of calculated total Ti based on measurement of ^{47}Ti and ^{48}Ti. Note: ΣREY for kutnohorite doesn't incorporate Y, Tb, Tm & Yb which were not present in the standard.

elements. Pyrolusite shows an enrichment of LREE relative to HREE, negative Eu-anomaly and positive Y-anomaly (Figure 13d). Kutnohorite in the Moola Prospect shows REY fractionation trends differ between lithologies, although both have a slight HREE-enrichment; the granitic veinlet had elevated REY with a negative Eu-anomaly in comparison to the flow-banded rhyolite (positive Eu-anomaly) (Figure 13e).

DISTRIBUTIONS OF OTHER TRACE ELEMENTS

Feldspars

Albite and microcline differ greatly with respect to Rb-Sr-Ba concentrations; albite has high Sr with respect to Rb and Ba and microcline has high Rb and Ba (Ba often has considerably higher concentrations than Rb) with respect to Sr. Microcline has a higher total concentration of Rb-Sr-Ba than albite (mean Σ(Rb-Sr-Ba) concentrations; microcline: 2531 ppm and albite: 187 ppm). Ternary Rb-Sr-Ba plots allow differentiation between minerals and lithology (Figure 14).

Albite Rb-Sr-Ba ternary plot shows greater spread between different lithologies (Figure 14a); the Moola Prospect felsic volcaniclastic and the Myola Volcanics rhyolite porphyry plot along the Sr-Ba line. The Moola Prospect granitic veinlet has albite plotting towards the centre of the ternary plot. Albite was under-represented in the granite, only four were sampled and they show variable distributions. Microcline plots between Rb and Ba and is relatively depleted in Sr (Figure 14b). The granite and granitic veinlet plot within the same cluster which lies halfway between Rb and Ba; the felsic volcaniclastic has higher Ba when compared to the granite and the Myola Volcanic plots almost at the Ba apex. A Ba-Rb ternary plot shows better

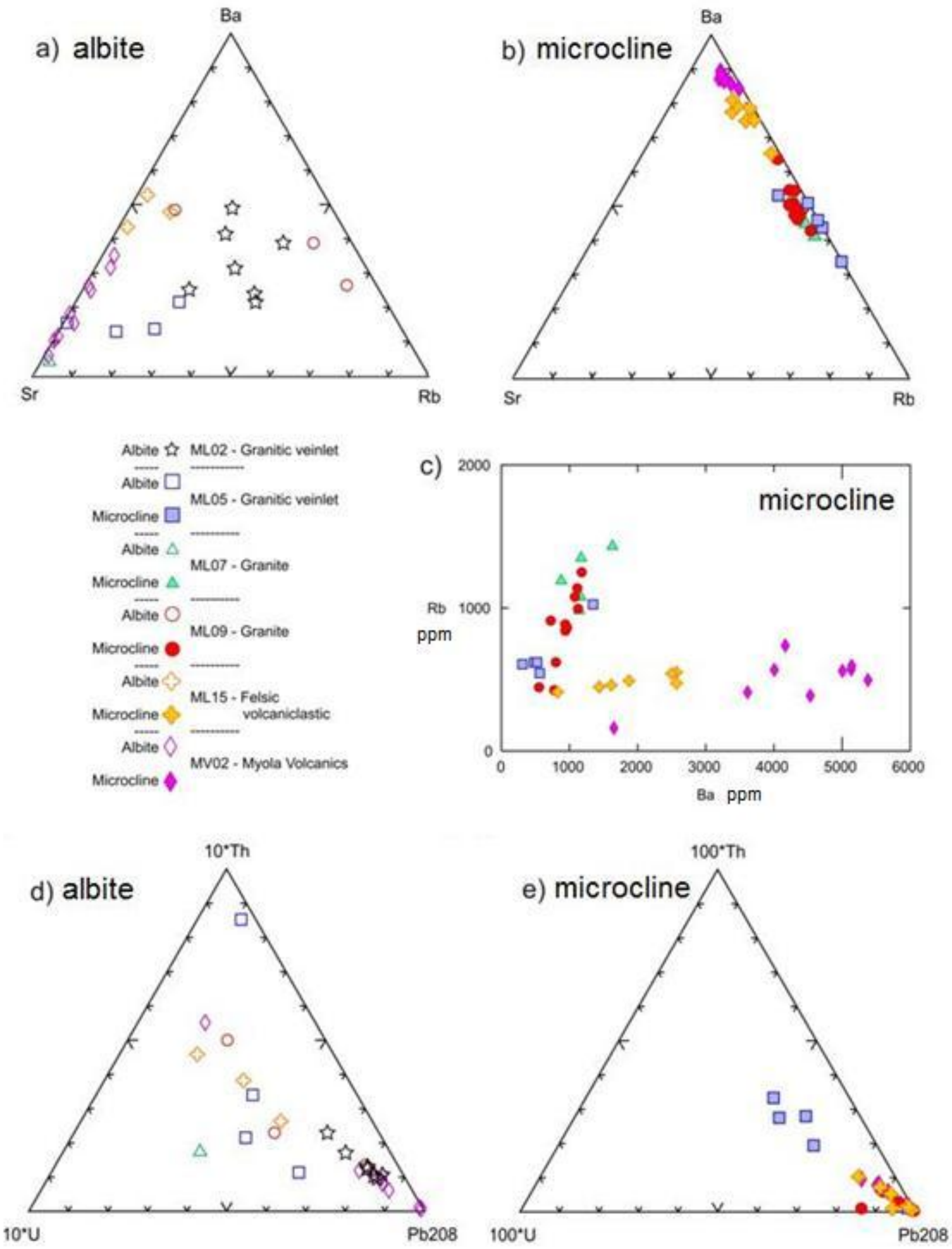

Figure 14 a) & b) Rb-Sr-Ba ternary plots for feldspars. Note albite is relatively rich in Sr in comparison to microcline. c) Rb-Ba binary plot showing distinct trends for microcline from felsic volcaniclastics, rhyolite porphyry, and granite. These plots allow for discrimination among lithologies. d) & e) U-Th-Pb ternary plots for feldspars, showing that albite has increased concentrations of U and Th with respect to Pb.

separation and very different trends for the granitic samples (very steep positive trend) versus felsic volcaniclastic samples (horizontal to slightly positive trend) (Figure 14c). Ismail *et al.* (in press) were able to use Rb-Sr-Ba ternary plots to differentiate microcline in ore-stage altered granite at Hillside from that in other lithologies. The ore-stage microcline was found to trend more towards the Sr apex than Moola prospect granite and granite veinlets in this study.

U-Th-Pb plots show albite is enriched in U and Th compared to microcline (Figure14d & e). Microcline in the Moola Prospect granitic veinlet plots alone and is able to be differentiated from other lithologies based on increased U and Th with respect to Pb.

Pyrite

Pyrite shows zonation with respect to As; correlation coefficients show no relationship between As and other elements analysed (Appendix D). Elevated Ni was found in PS12.

LA-ICP-MS ELEMENT MAPS

LA-ICP-MS element mapping of selected **Fe-oxide** grains (Figure 15) confirms that REY-enrichment corresponds to the degree of martitisation. This strongly suggests that the late-stage oxidising fluids responsible for replacement of pre-existing magnetite carried REY. There is also a positive correlation between enrichment in Mn, Zn and REY, as also shown by kutnohorite. The maps also confirm that V, Co and Ti are hosted within Fe-oxides.

LA-ICP-MS element maps (Figure 16) demonstrate the heterogeneous character of **kutnohorite** with respect to the major elements Ca, Fe, Mg and Mn, suggesting this mineral crystallised either during two or more discrete stages, or as a product of an

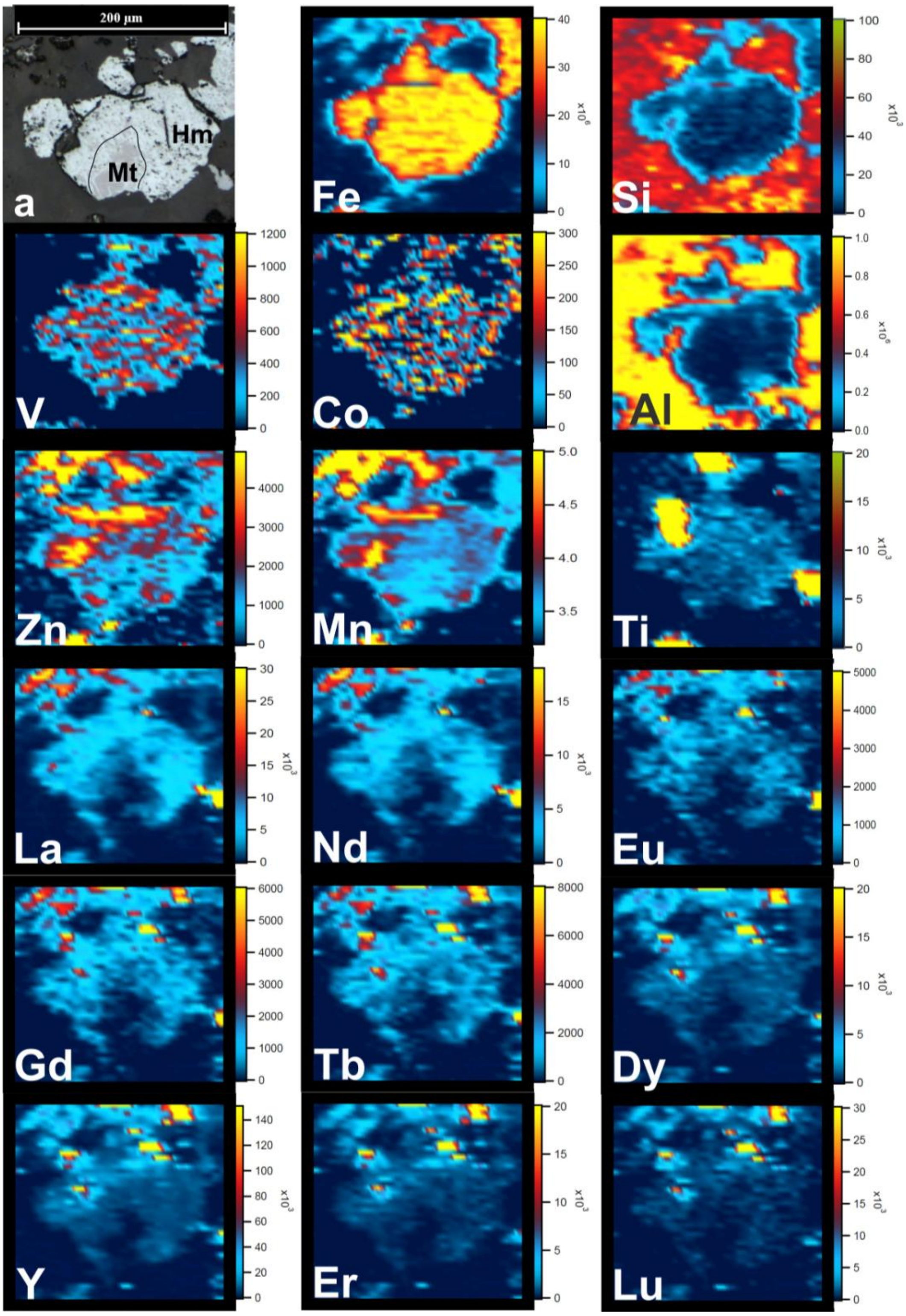

Figure 15 a) Reflected light image displaying the martite texture of hematite (Hm) replacement of magnetite (Mt). Remaining images are LA-ICP-MS element maps for the martite grain shown in (a). The degree of martitisation correlates with REE enrichment (particularly LREE). A moderate correlation can be seen between martitisation and the concentrations of Mn and Zn. Maps showing the distributions of V and Co illustrate their presence in Fe-oxides. Scales are in counts per second (logarithmic scale).

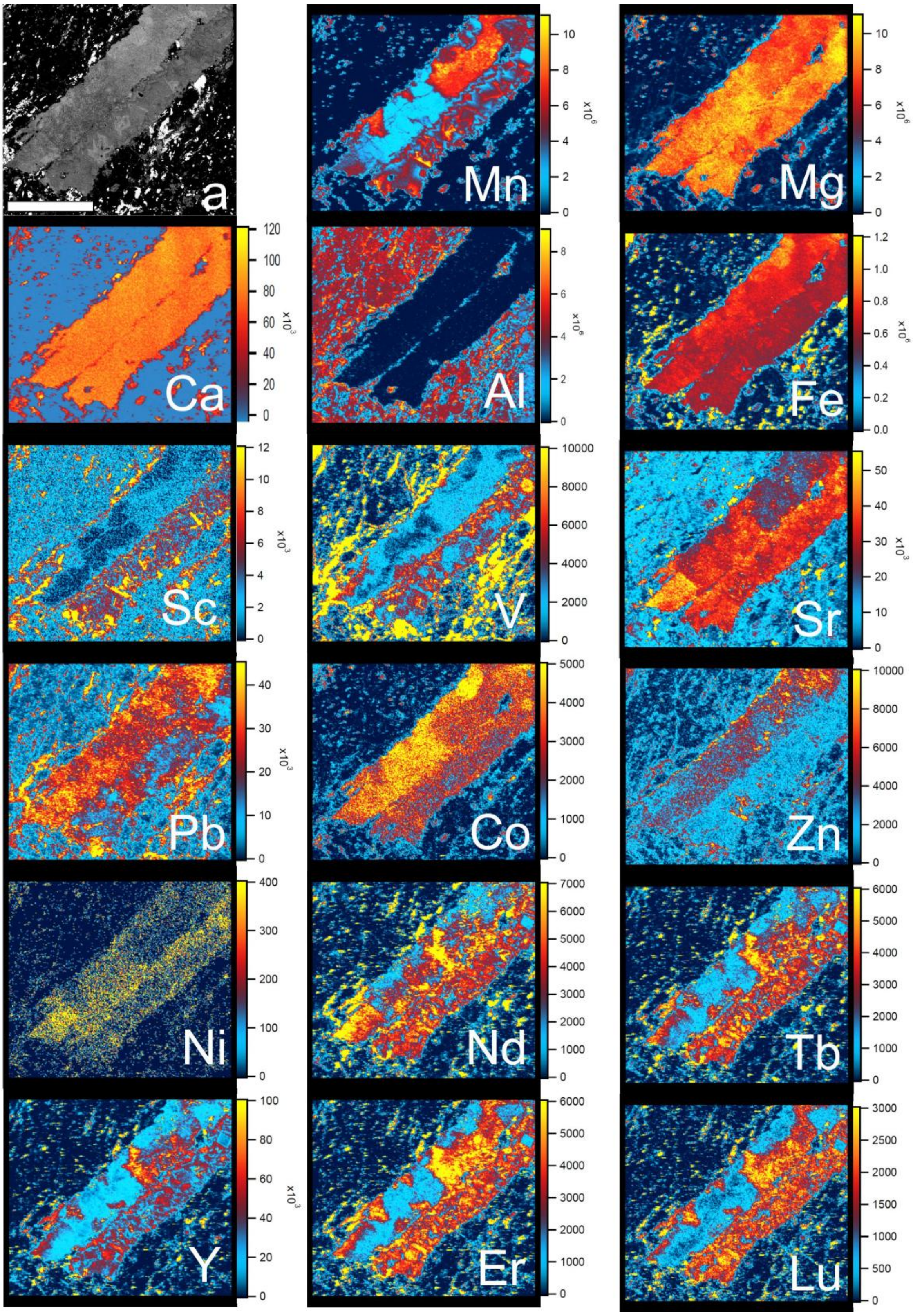

Figure 16 a) Back-scatter electron image of kutnohorite grain displaying compositional zonation (scale bar 1 mm). Remaining images are LA-ICP-MS element maps of this grain. Mn, Mg, Fe and Ca maps show that the grain-scale compositional zonation is largely attributable to major variations in Mn content. Kutnohorite is also zoned with respect to, and is a significant carrier of various metals and incompatible elements. Scales are in counts per second (logarithmic scale).

evolving hydrothermal fluid. A moderate correlation between Mn and REY is also noted. These elements, and in particular HREE, are strongly enriched in parts of the grain.

The zonation of metals and incompatible elements within the kutnohorite suggests the image is of two separate grains which grew in fluctuating chemical conditions. The top-left grain grew at a time of increased Pb, Zn and Ni and low Mn and REY; the grain may show similar REY zonation to the bottom-right grain if cut on a different cross section. Zonation within the bottom-right grain shows a progressive inward growth of kutnohorite; fluids were initially enriched in V, shown by the V zonation within initial growth. This was followed by an influx of Mn and REY.

Geothermometry

Temperatures of mineralisation can be bracketed by geothermometry applied to minerals that characteristically form relatively early such as rutile, and those formed later such as chlorite.

ZR-IN-RUTILE GEOTHERMOMETRY

Concentrations of Zr in rutile have been found to provide an accurate estimate of the temperature at which the rutile crystallised (Watson *et al.* 2006). Multiple LA-ICP-MS rutile analyses of rutile associated with late-stage ilmenite in sample ML16 gave a tight cluster of Zr concentration data (Table 8). Applying the calibration of Watson *et al.* (2006):

$$T(^{\circ}\mathrm{C}) = \frac{4470 \ \pm 120}{(7.36 \ \pm 0.10) - \log(Zr)} - 273$$

gives a temperature estimate of 458 ± 18 °C.

Table 8 Results of Zr-in-rutile geothermometry using the calibration of Watson et al. (2006).

Element	Zr (ppm)	T (°C)
ML16_RU01	14.1	447
ML16_RU02	19.2	463
ML16_RU03	16.4	454
ML16_RU04	20.4	466
ML16_RU05	19.0	462
ML16_RU06	22.6	471
ML16_RU07	32.4	491
ML16_RU08	21.1	467
ML16_RU09	14.1	447
ML16_RU11	15.6	452
ML16_RU12	7.59	417
	Average (μ)	458
	Std. Dev (σ)	17.7
Min Temperature =	μ - 2σ =	**440**
Max Temperature =	μ + 2σ =	**475**

CHLORITE GEOTHERMOMETRY

EMPA datasets for chlorite in 5 samples was obtained: 3 from the Moola Prospect and 2 from the Princess Prospect (Table 9). Chlorite-group minerals display a wide range of compositional variability in and around mineral deposits. Cathelineau (1988) has proposed that the chemical composition of chlorite, notably the distribution of Al between the two structural sites, can be used to calculate physiochemical conditions, in particular temperature, at the time of formation.

Chlorite in the Moola Prospect has a Fe/(Fe+Mg) ratio of ≤0.5. Temperatures calculated based on calibrations given by Cathelineau (1988) and Jowett (1991) range from 252 °C to 322 °C, possibly increasing with depth, although the small size of the dataset makes

Table 9 Electron probe microanalytical data for chlorite. Estimated formation temperature is calculated based on the calibrations of Cathelineau (1988) and Jowett (1991).

	ML04		ML06		ML17	PS05		PS14	
	mean	std. dev.	mean	std. dev.		mean	std. dev.	mean	std. dev.
	(n=9)		(n=8)		(n=1)	(n=9)		(n=19)	
Wt.%									
F	1.52	1.50	0.78	1.00	3.11	1.15	1.23	0.66	0.84
Cl	1.26	1.09	0.91	0.93	0.00	0.85	0.76	0.49	0.66
Na_2O	0.53	0.43	0.57	0.35	0.00	0.71	0.35	0.57	0.40
MgO	12.6	2.06	13.0	2.10	21.0	10.9	1.59	10.1	1.62
Al_2O_3	16.8	1.49	17.5	1.03	17.4	20.5	2.24	20.3	2.13
SiO_2	27.9	4.36	27.0	1.83	28.5	24.6	2.26	24.6	1.59
P_2O_5	0.34	0.31	0.29	0.19	0.31	0.32	0.09	0.32	0.18
K_2O	0.93	1.23	0.97	0.60	0.00	0.74	0.64	0.47	0.40
CaO	0.66	0.39	0.18	0.24	0.00	0.28	0.29	0.52	0.32
TiO_2	0.39	0.34	0.49	0.34	0.20	0.27	0.28	0.61	1.08
Cr_2O_3	0.34	0.50	0.94	1.03	0.00	1.10	0.56	0.64	0.60
MnO	1.20	1.41	0.38	0.89	3.20	0.90	1.03	0.75	0.84
FeO	23.7	4.37	24.5	3.77	23.3	29.4	2.23	27.9	3.44
Total	88.3	3.47	87.2	4.79	94.4	88.6	4.32	88.0	3.93
Atoms in formula based on Chlorite [(Fe,Mg)10Al2](Al2Si6)O20(OH)16									
Al (total)	4.32	0.29	4.48	0.28	4.04	5.18	0.40	5.24	0.41
Si	6.07	0.72	5.87	0.24	5.61	5.27	0.30	5.39	0.34
Al	1.93	0.72	2.13	0.24	2.39	2.73	0.30	2.61	0.34
Total	8.00	0.00	8.00	0.00	8.00	8.00	0.00	8.00	0.00
Al	2.39	0.62	2.35	0.23	1.65	2.45	0.48	2.63	0.39
Mg	4.09	0.58	4.20	0.67	6.15	3.46	0.54	3.30	0.49
Fe	4.31	1.00	4.45	0.69	3.84	5.25	0.51	5.11	0.65
Mn	0.22	0.26	0.07	0.16	0.53	0.16	0.18	0.14	0.16
Ti	0.06	0.06	0.08	0.05	0.03	0.04	0.04	0.10	0.19
Cr	0.06	0.08	0.16	0.17	0.00	0.19	0.09	0.11	0.10
Ca	0.15	0.09	0.04	0.06	0.00	0.06	0.06	0.12	0.08
Na	0.23	0.18	0.24	0.15	0.00	0.29	0.15	0.24	0.17
K	0.26	0.33	0.27	0.17	0.00	0.20	0.16	0.13	0.11
Total	11.8	0.49	11.9	0.26	12.2	12.1	0.30	11.9	0.35
F	1.05	1.03	0.54	0.69	1.94	0.78	0.84	0.45	0.57
Cl	0.46	0.40	0.33	0.35	0.00	0.31	0.27	0.18	0.25
(OH)	14.5	1.36	15.1	0.58	14.1	14.9	0.86	15.4	0.64
Total	16.0	0.00	16.0	0.00	16.0	16.0	0.00	16.0	0.00
Fe/(Fe+Mg+Mn)	0.50	0.06	0.51	0.06	0.37	0.59	0.03	0.60	0.06
% clinochlore	47.5	5.79	48.1	6.81	58.4	39.0	2.99	38.6	5.43
% chamosite	50.0	5.90	51.1	6.23	36.5	59.2	2.50	59.7	5.77
% pennantite	2.56	2.95	0.80	1.96	5.06	1.83	2.29	1.62	1.84
Alivc (KN)	2.29	0.74	2.49	0.22	2.66	3.15	0.30	3.04	0.33
Alivc (J)	1.98	0.72	2.19	0.24	2.43	2.79	0.30	2.67	0.33
Temperature (°C) estimates									
Cath 1988	**252**	53.3	**282**	-23.5	**322**	**379**	-13.1	**358**	-7.98
J 1991	**250**	45.8	**280**	-31.5	**318**	**377**	-20.8	**357**	-15.8

this difficult to confirm. Chlorite in samples from the Princess Prospect is consistently richer in Fe and returns higher temperatures (358-379 °C).

DISCUSSION

Comparison of the Princess and Moola Prospects and Myola Volcanics

Direct comparison of trace element patterns in the three areas proved difficult due to the major lithological differences between them, which impacts on mineral assemblages present and the relative proportions of each phase. Although the Myola Volcanics and the Moola Prospect can be compared, the Princess Prospect is significantly different in several respects. Additionally, the fine-grained character of samples from the Princess Prospect resulted in a reclassification of lithology (from fine-grained mafic unit to metasediments) following petrographic investigation.

Multiple generations of Fe-(Ti)-oxides, each with distinct trace element geochemistry, are recognised in many samples (Figures 6c, e, 9, 11 & 15; Table 3). The Myola Volcanics feature an early magnetite phase that subsequently underwent varying degrees of martitisation (Figures 9 & 15). Iron-oxides in the Moola Prospect and Myola Volcanics are enriched in both Ti and Mn. Titaniferous hematite is the dominant Fe-oxide in the Moola Prospect, alongside a subordinate, late-stage bladed Ti-poor hematite (Figure 10). Iron oxides in the Princess Prospect are constrained to the hematite breccia (Figures 4g & 5g); no Fe-oxides were observed in the metasedimentary rocks. Here, bladed hematite was poor in both Ti and Mn, fine-grained within breccia clasts, and coarse-grained within breccia infill. A late-stage magnetite was observed as rims of bladed grains (Figure 8f).

The diversity of textures and morphologies shown by hematite (and, to some extent, magnetite) is comparable with those in other IOCG systems in the Olympic Province (Belperio *et al.* 2007; Ciobanu *et al.* in press), even if most of the studied samples are relatively poor in Fe-oxides compared to these other systems.

Sulphides are present at all three sample locations, although most of the sulphides are restricted to late-stage quartz-carbonate veins (Figures 7a, b & 8c, h). Disseminated pyrite and chalcopyrite are common, the most significant volumes of sulphides (and highest Cu contents) are found in the Moola Prospect at the contact between the granite and the felsic volcaniclastic rock within silicic breccias. The silicic breccia hosts a complex, overprinting sulphide assemblage (Figure 8a, e & d).

Accessory minerals are present throughout sample suite. Multiple generations of Rutile (volcanic and hydrothermal) are present in the Moola Prospect (Figure 6e, h & k) whereas the Princess prospect mainly contains detrital rutile (Figure 6j) with minor, very fine-grained hydrothermal (?) rutile associated with monazite (Figure 6a). Apatite was fine grained and sparsely disseminated throughout all samples.

Rubidium, Sr and Ba concentrations and ternary plots for feldspars allows for differentiation between minerals and lithology (Figure 14).

REY distributions and their petrogenetic and exploration significance

Distribution of REY within and surrounding mineralisation have been proposed as a potential exploration tool for IOCG-style mineralisation (Ismail *et al.* in press). Since alteration halos enclosing an ore can be significantly larger than the mineralised zone itself, they may be easier to find, especially when exploring under cover. A regional comparison of REY and other trace element concentrations within selected minerals, in the context of regional-scale albitisation, and more local-scale potassic alteration, may thus provide a viable vector to ore. An understanding of the partitioning of REY between all minerals in the unaltered rock, alteration halo(s) and mineralised zone, and their behaviour during successive alteration events, is however required before such techniques can be routinely applied.

Iron-oxides have been demonstrated to be significant carriers of REY in IOCG systems (Ciobanu *et al.* in press). Further work by the same authors, as yet published, shows the distribution of REY in Fe-oxides varying between samples from different parts of an IOCG system. Within this context, a significant advance in understanding the underlying processes related to REE-enrichment in Fe-oxides comes from the study of the Myola Volcanics reported here. The data clearly demonstrates that the degree of martitisation correlates with an influx of REE (Figure 9 & Table 3). 'Primary' magmatic magnetite characteristically contains relatively low REY but with increasing degrees of replacement by hematite, REY concentrations (mostly LREE) increase over several orders of magnitude. A logical interpretation of these patterns is that a late, oxidising fluid was responsible for martitisation and it was this fluid which introduced REY (and other trace elements) into the system (either directly from source or via remobilisation from elsewhere in the system) (Figure 9, Table 3). This may occur during hydrolithic alteration associated with sericite enrichment (e.g. Williams *et al.* 2005).

Enrichment in LREE is a common feature of Fe-oxides-dominated ores at Olympic Dam (Oreskes & Einaudi 1990; Ehrig *et al.* 2013); and in other IOCG systems in the Olympic Province which display a dominant sericitic alteration. In contrast, hematite from IOCG systems associated with skarn alteration display a marked enrichment of

HREE that can be correlated with the stage of mineralisation. Additional data are clearly required to ascertain whether predictable patterns exist which carry implications for the development of exploration tools, or whether REY endowments in Fe-oxides are controlled by partitioning among coexisting minerals

Titaniferous hematite in the Moola Prospect is generally low in REY and displays highly variable chondrite-normalised REY fractionation plots albeit with a slight, consistent increase of ΣREE down-hole, through different lithologies (Figure 10, Table 3). The highly variable patterns may be attributed to REE partitioning between hematite and exsolved lamellar ilmenite; the relatively low spatial resolution of LA-ICP-MS analysis (spot size 30 μm) would have inevitably led to varying amounts of ilmenite being analysed (Figures 6e & 7e).

Iron-oxides in the Princess Prospect display very different REY fractionation trends. Bladed hematite within the hematite breccia has relatively low ΣREY and variable chondrite-normalised patterns; the fine-grained bladed hematite in breccia clasts displays a slight LREE-enrichment when compared to the coarse-grained breccia infill (Table 3). This indicates that the remobilised hematite was not deposited from REY-rich fluids. Late-stage magnetite rims on bladed hematite grains (Figure 8f), however, do show elevated REY, indicating there was a late Fe-oxide remineralisation event, probably under reduced conditions. Such relationship contrast, however, with those seen in the Myola Volcanics, suggesting that highly localised conditions and sequences of hydrothermal fluid flow may be present, and their respective fluid/rock ratios, may vary considerably across the district.

Feldspars were identified only in the Myola Volcanics and Moola Prospect and are not significant carries of REE; La and Ce were the only elements found above minimum detection limits (Figure 12, Table 4). This contrasts with the critical role of feldspars as REY-carriers at Hillside (Ismail *et al.* in press). Despite the obvious limitations of interpreting results that are close to or below minimum detection limits, the REY plots nevertheless show similarities to those presented for Hillside.

Accessory minerals play an important role in controlling REY distributions. Minerals of the apatite-supergroup (Pasero *et al.* 2010), in particular, can incorporate up to several wt.% ΣREE (Pan & Breaks 1997); substitution of REE^{3+} for Ca^{2+} is compensated by replacement of P^{5+} by Si^{4+}. Apatite from the Moola Prospect granite, granitic veinlet and felsic gneiss showed consistent REY patterns (MREE-enriched) that mimic those observed in the ore-stage skarn assemblage at Hillside (Ismail *et al.* in press) (Figure 13a, Table 6). Apatites in flow-banded rhyolite from the Moola Prospect and in the metasedimentary rocks have similar negative REY trends but only rhyolite-hosted apatite features a negative Eu-anomaly. If these patterns indicate a systematic response of apatite chemistry to alteration associated with mineralisation, following ideas presented by Cao *et al.* (2012) and others, they would suggest that the Princess Prospect is not as prospective as an IOCG target as the Moola Prospect.

Rutile displays a considerable diversity of textures throughout the same suite (both between and within individual lithological groups) and displays the most diverse range of REY fractionation trends of all the minerals covered in this study (Table 5). Sub-populations of detrital, magmatic and hydrothermal rutile exist. This mineral has attracted considerable interest from earth scientists because of its varied geochemistry which makes it a suitable mineral for innovative applications in geochronology, thermometry and isotope geochemistry (e.g. Meinhold 2010) but a comprehensive treatment of rutile chemistry is beyond the scope of the present study. In particular, better constraints on rutile chemistry would require sampling and analysis of less-altered lithologies, particularly magmatic rocks, to unequivocally constrain primary geochemical signatures.

Titanite observed in the Myola Volcanics rhyolite porphyry forms clusters together with rutile (Figure 6j). The adjacent rutile shows LREE-enrichment whereas the titanite shows HREE-enrichment suggesting equilibrium partitioning between the two phases (Figure13b & c). The REY fractionation trends for titanite are similar to those given for other IOCG systems, Ismail *et al.* (in press) and Smith *et al.* (2009). The latter author relates the pattern to hydrolithic alteration.

This study presents LA-ICP-MS trace element data for kutnohorite and pyrolusite, which to our knowledge has not been given in any previous study (Figures 6d, 8b, 13d, e &16, Table 7). The data shows that these minerals are all significant hosts for REY. Both minerals, as well as the poorly characterised jacobsite (omitted due to uncertainties regarding its internal homogeneity at the scale of the laser spot) are relatively late-stage minerals. The observed REE-enrichment may have been caused by remobilisation of existing REY within the system, or via a later influx of REE. Manganese, an element more abundant in the studied locations than in other IOCG systems, correlates strongly with REE enrichment; this relationship is observed on both the martite and kutnohorite element maps (Figures 15 & 16).

Significant local variation of the REY distributions is observed within individual lithologies. This is demonstrated by the dissimilar REY distribution in Fe-oxides and apatite between the two macroscopically near-identical Myola Volcanic rhyolite porphyry samples collected 20 m from each other (Figures 9 & 13a).

Towards a preliminary genetic model

PRINCESS PROSPECT

Hematite-rich breccias are the major host rock for sulphide Cu-Au-(U) mineralisation at Olympic Dam (Ehrig *et al.* 2013); no sulphides are, however, observed within the Princess Prospect hematite breccia. Low overall ΣREY values and a slight decrease in abundance from breccia clast to matrix suggest breccia fluids were not REY-rich (Table 3).

There is evidence for late-stage fluid mobilisation in the metasedimentary rocks; quartz-carbonate crackle veins and silica flooding is associated with increased sericitic alteration, late-stage Mn minerals (rhodochrosite, kutnohorite and jacobsite (?)), pyrite and chalcopyrite (Figure 8a, e & d). Nickel baring pyrite shows zonation suggesting it grew in the presence of an evolving fluid with a potential mafic source, or which leached metals from a mafic source (Figure 8c). Uraninite, the most common uranium mineral in IOCG mineral (Hitzman & Valenta 2005), is seen in vughs. The metasedimentary rocks contain little to no Fe-oxides which, suggesting there is no direct evidence in the studied samples for a genetic relationship between the hematite breccia and introduction of hydrothermal fluids.

Chlorite within the Princess Prospect metasedimentary rocks is relatively Fe-rich. Application of chlorite geothermometry (De Caritat *et al.* 1993) gives an estimated formation temperature of between 357 ºC and 379 ºC (Table 9). The temperature is consistent between different samples collected over considerable depth range. This temperature can potentially be interpreted as representing the conditions of the metamorphic event which converted the sedimentary protolith to the metasedimentary sequence observed. It may, alternatively, show temperature conditions of the metasomatic/hydrolithic alteration episode.

REY fractionation trends in minerals from the Princess Prospect drill core do not reflect those seen in other IOCG deposits (Smith *et al.* 2009; Ehrig *et al.* 2013; Ismail *et al.* in press). The fine grain-size was a major limiting factor for analysis by LA-ICP-MS. Further investigation of, preferably coarse-grained samples, of other Princess Prospect lithologies (not present in sampled drill core) would be required to better understand the REY distribution within this prospect.

MOOLA PROSPECT AND MYOLA VOLCANICS

A sequence of events can be reconstructed based on the textural, mineralogical and geochemical data presented above. Hydrolithic alteration associated with an influx of REY has affected both the Moola Prospect and Myola Volcanics.

Two brecciation events are observed within the Moola Prospect; the breccia observed in the felsic banded gneiss contains clasts of both granite and felsic gneiss suggesting formation late in the evolution of the sequence (Figure 4b). It displays no observed association with sulphides, and the infill is chlorite-rich (Figure 5b) and relatively silica poor when compared to the breccia at depth. The infill does, however, contain Mn-minerals and also late-stage, Ti-poor bladed hematite (contrasting with the clasts in which the hematite is Ti-rich).

Breccia observed between the granite and the felsic volcaniclastic has predominantly silicic infill contains unique sulphide mineralogy (Figure 8a, d & e). It contains evidence for several stages of superimposed Cu-mineralisation, supporting the idea that

this breccia must have formed relatively early in the evolution of the sequence, and that its greater porosity enabled it to continue to serve as a conduit for an evolving fluid.
REY fractionation trends for titanite (Figure 13b) support the hypothesis that hydrolithic alteration of the Myola Volcanics rhyolite porphyry is potentially associated with influx of oxidising fluids responsible for martitisation and remobilisation of REY, Mn and Zn (Figures 9 & 15). This hydrolithic alteration resulted in an increase in REY concentrations, particular LREE. This hypothesis is supported by REY distributions in Fe-oxides and rutile in the two Myola Volcanics samples (MV01 and MV02). Iron-oxides in MV01 show martitisation and rutile enriched in LREE, whereas MV02 contains only unaltered magnetite, and the rutile is relatively HREE-enriched. This would suggest that hydrolithic alteration was more pervasive in the first sample, raising the possibility of pronounced local variations in the intensity of alteration as a function of minor lithological differences that dictate major fluctuations in fluid/rock ratios.
Martite, titaniferous hematite, rutile, ilmenite, pyrolusite, albite and microcline in the Moola Prospect and Myola Volcanics consistently indicate an enrichment of LREE within the system (Figures 9, 10, 11, 12, & 13c, d).
Quartz-carbonate veins observed to crosscut the Moola Prospect granite contain late-stage pyrite, chalcopyrite, sphalerite and uraninite (Figure 7b).
Zr-in-rutile geothermometry on a single rutile grain from the Moola Prospect flow-banded rhyolite featuring late-stage ilmenite alteration associated with REE enrichment indicated a formation temperature in the range 440 ºC to 475 ºC (Table 8). This temperature is considered to represent formation conditions and is possibly an approximate temperature estimate for the hydrothermal event. Lower temperatures obtained from chlorite geothermometry (250-282 ºC in granitic veinlets, and 318-322 ºC

in flow-banded rhyolite) are taken to represent either retrograde hydrothermal conditions, or those of the metamorphic overprint (Figure 11, Table 8).

Covellite, the last Cu-mineral to form in voids in the felsic breccia (Figure 8d), is a common supergene replacement product of bornite or chalcocite, and less commonly, also chalcopyrite (e.g. at Olympic Dam; Ehrig *et al.* 2013). The relationship between kutnohorite and covellite seen in the Moola Prospect silicic breccia may suggest that Mn minerals within vughs and voids could be explained by late supergene processes (Fig. 8b & d). The timing of that supergene event is, however, highly uncertain.

Although many authors consider IOCG mineralisation in the Gawler Craton to be a single event at ~1595-1585 Ma (e.g. Skirrow *et al.* 2007), a number of published post-1590 Ma ages for mineralisation (McInnes *et al.* 2008; Maas *et al.* 2011) may be evidence for late-stage, lower-temperature overprinting.

CONCLUSIONS

This paper has confirmed that the martitisation event, in which primary magnetite was replaced by hematite, was accompanied by an influx of REE. This is significant for development of a sustainable genetic model which can be applied to both previously characterised and newly-discovered IOCG system in South Australia. This finding carries implications for both the relative timing of hydrothermal fluid flow (post-dating an initial generation of magnetite), and for fluid chemistry (identifying a shift to oxidising conditions). In many IOCG systems, primary magnetite is scarcely preserved (e.g. Prominent Hill), or is restricted to certain parts of the deposit (e.g. Olympic Dam). Sulphide assemblages observed within the Moola Prospect, in particular, are complex and record sequential cycles of recrystallisation as a response to evolving conditions, remobilisation of some components, and a distinct, late-stage oxidised overprint. Compositional zoning is recognised in pyrite suggesting fluid evolution during growth. Similar trace minerals (e.g. wittichenite) are identified as in other South Australian IOCG systems, stressing the communality of ore-forming processes across the region. Patterns of brecciation and replacement and are also similar to those identified in other IOCG domains, emphasizing shared origins. The relatively late Mn-enrichment is, however, a conspicuous feature of IOCG-style mineralisation in the Middleback Ranges. This may relate to the presence of Mn-rich rocks within the host sequence from which the element was leached.

There is widespread evidence for element redistribution within the mineralisation during at least one, superimposed, retrograde event. This is supported by the successive replacement of Cu-sulphides and late-stage remobilisation of Mn (forming pyrolusite and kutnohorite).

Comparison of the REE chemistry of minerals in mineralised, altered and barren zones represents a potential exploration tool *if* robust constraints on the factors responsible for the observed patterns can be established. This study has shown that minerals such as kutnohorite and pyrolusite are hitherto unrecognised REE-carriers, and their presence may impact on overall REE distributions.

This study has generated a dataset which is broadly congruent with those from other South Australian IOCG systems. The very fine grain size of some samples (making accurate application of some microanalytical techniques, notably LA-ICP-MS, difficult or impossible), and the extensive heterogeneity of geochemical patterns between samples and different lithologies, may nevertheless impact on development of an empirical exploration model or exploration tool at this stage.

Observations in this study are consistent with the presence of sizeable/multiple IOCG alteration envelopes within the Middleback Ranges. A comparative study between Myola Volcanics and the Moola and Princess Prospects has found significant differences; REY distributions in apatite and Fe-oxides suggest that IOCG alteration was more prevalent in the Moola Prospect and Myola Volcanics.

ACKNOWLEDGMENTS

I would like to thank Nigel Cook for his guidance and assistance throughout the duration of this 2-year part-time project; his input, knowledge and support has been invaluable. A special mention goes to Cristiana Ciobanu for her guidance in petrographic analysis and contribution to this manuscript. I would also like to thank Arrium Mining for supporting this project and the exploration team for their patience and assistance; in particular, Geoff Johnson for his continued backing and encouragement - I will be forever grateful for the opportunity to work and study in conjunction. I would like to thank the staff at Adelaide Microscopy, namely, Ben Wade, Angus Netting, Aoife McFadden and Ken Neubauer.

REFERENCES

BAKER T., REID A. & GREGORY C. 2011. The 1.6 to 1.5 Ga IOCG event: origin and timing of IOCG mineral systems. *SGA 2011, 11th Biennial Meeting*.

BASTRAKOV E. N., SKIRROW R. G. & DIDSON G. J. 2007. Fluid evolution and origins of iron oxide Cu-Au prospects in the Olympic Dam district, Gawler craton, south Australia. *Economic Geology* **102**, 1415-1440.

BAU M. 1996. Controls on the fractionation of isovalent trace elements in magmatic and aqueous systems: Evidence from Y/Ho, Zr/Hf, and lanthanide tetrad effect. . *Contributions to Mineralogy and Petrology* **123**, 323-333.

BELPERIO A., FLINT R. & FREEMAN H. 2007. Prominent Hill: A hematite-dominated, iron oxide copper-gold system. *Economic Geology* **102**, 1499-1510.

CAO M., LI G., QIN K., SEITMURATOVA E. Y. & LIU Y. 2012. Major and trace element characteristics of apatites in granitoids from Cantral Kazachstan: Implications for petrogenesis and mineralization. *Resource Geology* **62**, 63-83.

CATHELINEAU M. 1988. Cation site occupancy in chlorites and illites as a function of temperature. *Clay Minerals* **41**, 471-485.

CAVE B. 2010. Copper - Gold Exploration in the Middleback Ranges; Source(s) of Fluids and Metals. Bachelor of Science with Honours in Geology thesis, Department of Geology and Geoscience, The University of Adelaide (unpubl.).

CHAMALAUN F. H. & PORATH H. 1967. Palaeomagnetism of Australian Hematite Ore Bodies–I The Middleback Ranges of South Australia. *Geophysical Journal of the Royal Astronomical Society* **14**, 451-462.

CIOBANU C. L., WADE B., COOK N., SCHMIDT-MUMM A. & GILES D. in press. Uranium-bearing hematite from the Olympic Cam Cu-U-Au deposit, South Australia; a geochemical tracer and reconnaissance Pb-Pb geochonometer. *Precambrian Research*. doi.org/10.1016/j.precamres.2013.10.007.

CONOR C., RAYMOND O., BAKER T., TEALE G., SAY P. & LOWE G. 2010. Alteration and Mineralisation in the Moonta-Wallaroo Cu-Au Mining Field Region, Olympic Domain, South Australia. *Hydrothermal Iron Oxide Copper-Gold and Related Deposits: A Global Perspective.* 1-24.

DE CARITAT P., HUTCHEON I. & WALSHE J. L. 1993. Chlorite geothermometry: a review. *Clay and Clay Minerals* **41**, 219-239.

EHRIG K., MCPHIE J. & KAMENETSKY V. S. 2013. Geology and mineralocigal zonation of the Olympic Dam iron oxide Cu-U-Au-Ag deposit, South Australia. *Society of Economic Geologists Feology and Genesis of Major Copper Deposits and Districts of the World, a Tribute to Richard Sillitoe.* 237-368.

FIETZ G. 1989. The geological structure and slope stability of the Iron Duke iron ore deposit. . South Australian Institute of Technology (unpubl.).

GROVES D., BIERLEIN F., MEINERT L. & HITZMAN M. W. 2010. Iron Oxide Copper-Gold (IOCG) Deposits through Earth History: Implications for Origin, Lithospheric Setting, and Distinctions from other Epigenetic Iron Oxide Deposits. *Economic Geology* **105**, 641-654.

HAND M., REID A. & JAGODZINSKI L. 2007. Tectonic Framework and Evolution of the Gawler Craton, Southern Australia. *Economic Geology* **102**, 1377-1395.

HAYNES D. W., CROSS K. C., BILLS R. T. & REED M. H. 1995. Olympic Dam ore genesis: A fluid mixing model. *Economic Geology* **90**, 281-307.

HAYWARD N. & SKIRROW R. G. 2010. Geodynamic setting and controls on iron oxide Cu-Au (+/−Y) ore in the Cawler Craton, South Australia. *Hydrothermal Iron Oxide Copper Gold & Related Deposits: A Global Perspective. Vol 3.* 1-27.

HICKS C. B. 2010. The Regolith Expression of Cu-Au mineralisation within the Northern region of the Project Mawson area, NE Eyre Peninsula, South Australia. Bachelor of Science with Honours in Geology thesis, Department of Geology and Geophysics, The University of Adelaide (unpubl.).

HITZMAN M. W. 2000. What, where, when and why. *Australian Mineral Foundation Hydrothermal iron oxide copper-gold and related deposits. A global perspective.* 9-26.

HITZMAN M. W., ORESKES N. & EINAUDI M. T. 1992. Geological Characteristics and Tectonic Setting of Proterozoic Iron-Oxide (Cu-U-AU-REE) Deposits. *Precambrian Research* **58**, 241-287.

HITZMAN M. W. & VALENTA R. K. 2005. Uranium in iron oxide-copper-gold (IOCG) systems. *Economic Geology* **100**, 1657-1661.

ISMAIL R., CIOBANU C. L., COOK N., GILES D., SCHMIDT-MUMM A. & WADE B. in press. Rare Earths and other trace elements in mineral form skarn assemblages, Hillside iron oxide-copper-gold deposit, Yorke Peninsula, South Australia. *Lithos.* doi.org/10.1016/j.lithos.2013.07.023.

JOHNSON J. P. & CROSS K. C. 1995. U-Pb geochronological constraints on the genesis of Olympic Dam Cu-U-Au-Ag deposit, South Australia. *Economic Geology* **88**, 1046-1063.

JOWETT E. C. 1991. Fitting iron and magnesium into the hydrothermal chlorite geothermometer. GAC/MAC/SEG Joint Annual Meeting, Toronto (unpubl.).

LEEVERS P. 2006. The Hematite Report. *OneSteel*.

MAAS R., KAMENETSKY V. S., EHRIG K., MEFFE S., MCPHIE J. & DIEMAR G. 2011. Olympic Dam U-Cu-Au deposit, Australia: New age constraints. *Mineralogical Magazine* **75**, 1375.

MCDONOUGH W. F. & SUN S. S. 1995. The composition of the Earth. *Chemical Geology* **120**, 223-253.

MCINNES B. I. A., KEAYS R. R., LAMBERT D. D., HELLSTROM J. & ALLWOOD J. S. 2008. Re-Os geochronology and isotope systematics of the Tanami, Tennant Creek and Olympic Dam Cu-Au Deposits. *Australian Journal of Earth Sciences* **55**, 967-981.

MCINTYRE 2001. Middleback Ranges Project - South Australia. EL 2763 Annual Report. *Helix Resources N.L.*

MCPHIE J., KAMENETSKY V. S., ALLEN S., EHRIG K., AGANGI A. & BATH A. 2011. A flourine link between a supergiant ore deposit and a silicic large igneous province. *Geology* **39**, 1003-1006.

MEINHOLD G. 2010. Rutile and its applications in earth sciences. *Earth Science Reviews* **102**, 1-28.

MITCHELL C. 2010. The Regolith Expression of IOCG mineralisation within the southern region of the Project Mawson area, NE Eyre Peninsula, South Australia. Bachelor of Science with Honours in Geology thesis, Department of Geology and Geophysics, The University of Adelaide (unpubl.).

MURASHKO M. N., CHAKANOV N. V., MUKHANOVA A. A., VAPNIK E., BRITVIN S. N., POLEKHOVSKY Y., S. & IVAKIN Y. D. 2011. Barioferrite $BaFe_{12}O_{19}$: A New Mineral Spicies of the Magnetoplumbite Group from the Haturim Formation in Israel. *Geology of Ore Deposits* **53**, 558-563.

ORESKES N. & EINAUDI M. T. 1990. Origin of Rare Earth Element-Enriched Hematite Breccias at the Olympic Dam Cu-U-Au-Ag Deposit, Roxby Downs, South Australia. *Economic Geology* **85**, 1-28.

PAN Y. & BREAKS F. W. 1997. Rare-earth elements in fluoroapatite, Separation Lake Area, Ontario: Evidence for S-type granite - rare element pegmatite linkage. *Canadian Mineralogist* **35**, 659-671.

PARKER A. J. 1993. Precambrian. The geology of South Australia. Vol. 1, The Precambrian. *South Australia, Geological Survey, Bulletin*.

PARKER A. J. & FANNING C. M. 1998. *Explanatory Notes for the WHYALLA 1:250 000 Geological Map*. SA P. I. a. R. Gillingham Printers Pty Ltd.

PARKER A. J., FANNING C. M., FLINT R., MARTIN A. R. & RANKIN L. R. 1988. Archaen Proterozoic granitoids, metasediments and mylonites of southern Eyre Peninsula, South Australia. *Geological Society of Australia. Specialist Group in Techtonics and Structural Geology.*

PASERO M., KAMPF A. R., FERRARIS C., PEKOV I. V., RAKOVAN J. & WHITE T. J. 2010. Nomenclature of the apatite supergroup minerals. . *European Journal of Mineralogy* **22**, 163-179.

SKIRROW, R.G., RAYMOND, O.L., BASTRAKOV, E., DAVIDSON, G. & HEITHERSAY, P. 2002. The geological framework distribution and controls of Fe oxide Cu-Au mineralisation in the Gawler craton, SA. Part II. Alteration and mineralisation. In: Porter, T.M. ed. *Hydrothermal IOCG and related deposits: A global perspective*, vol. 2. Australian Mineral Foundation, Adelaide, pp. 33-47.

SKIRROW R. G., BASTRAKOV E. N., BAROVICH K., FRASER G. L., CREASER R. A., FANNING C. M., RAYMOND O. L. & DAVIDSON G. J. 2007. Timing of Iron Oxide Cu-Au-(U) Hydrothermal Activity and Nd Isotope Contraints on Metal Sources in the Gawler Craton, South Australia. *Economic Geology* **108**, 1441-1470.

SMITH N. P., STOREY T. E., JEFFRIES T. E. & RYAN C. 2009. *In Situ* U-Pb and Trace Element Analysis of Accessory Minerals in the Kiruna District, Norrbottem, Sweden: New Constraints on the Timing and Origin of Mineralization. *Journal of Petrography* **50**, 2063-2094.

SZPUNAR M., HAND M., BAROVICH K., JOGODZINSKI E. & BELOUSOVA E. 2011. Isotopic and geochemical constraints on the Paleoproterozoic Hutchison Group, southern Australia: implications for Paleoproterozoic continental reconstructions. *Precambrian Research* **187**, 99-126.

WATSON E. B., WARK D. A. & THOMAS J. B. 2006. Crystallisation thermometers for zircon and rutile. *Contrib Mineral Petrol* **151**, 413-433.

WILLIAMS P. J., BARTON M. D., JOHNSON D. A., FONTBOTE L., HALLER A., MARK G., OLIVER N. H. S. & MARSCHIK R. 2005. Iron oxide copper-gold deposits: Geology, space-time distribution, and possible modes of origin. *Economic Geology 100th Anniversary Volume*. 371-405.

WILLIAMS P. J. & POLLARD P. J. 2002. Australian Proterozoic Iron Oxide-Cu-Au Deposits: An Overview with New Metallogenic and Exploration Data from the Cloncurry District, Northwest Queensland. *Explor. Mining Geol.* **10**, 191-213.

YEATES G. 1990. Middleback Range Iron Ore Deposit. *The Institute of Mining and Metallurgy Geology of the Mineral Deposits of Australia and Papua New Guinea*. 1045-1048.

APPENDIX A - METHODS

Sample Collection

Myola Volcanics Samples (MV01 & MV02)

- 3 hand samples, roughly 20 x 20 x 20 cm^3 in size and weighing ~1 kg, were collected from the Myola Volcanics Type Location.
- Samples were collected from outcrop with a geo-pick.
- Sample selection considered the degree of weathering of the surface outcrop and targeted rhyolite that showed little to no alteration or deformation.
- Two of the three hand samples were selected to make thin sections from – these samples were washed and cut to reveal fresh surfaces.
- In preparation for the thin section production 2.5 x 5 cm areas on the sample were selected, marked on sample and photographed.

Drill core samples (ML01-ML17 & PS01-PS16)

- 18 samples were selected from ML001DD drill core and 19 samples were selected from PRD01A drill core based on assay and lithology data. All but 1 were half core samples, the other was a quarter core sample.
- Selection criteria considered:
    - Representative samples for different lithologies.
    - Representative samples for different alteration styles, particularly sericite alteration.
    - Presence of iron oxides, particularly hematite.
    - Presence of sulphides, particularly Cu bearing sulphides.
    - Presence of veining.
- A second review of drill core samples resulted in 17 samples from ML001DD and 16 samples from PRD01A being selected to make thin sections. The rejection of 4 samples was based on them being quite similar to other samples.
- In preparation for thin section production 2.5 x 5 cm areas were selected, marked on sample and photographed.
- MapInfo GIS software was used to prepare location maps of samples.
- Datamine software was used to model locations of samples on drill holes. The model of ML001DD also included location of samples taken from previous University of Adelaide Geology Honours projects.

Sample Preparation

- A total of 35 samples were sent to Pontifex and Associates who cut samples and prepared 2.5 x 5 cm thin sections for mineralogical and petrographic analysis.

Petrographic Analysis

All petrographic analysis was completed at Adelaide Microscopy

Transmitted and Reflected Light Petrography

- The Nikon LV100 polarising petrological microscope was used to analyse samples; the machine has a capacity to magnify up to 50x and can function with both transmitted and reflected light modes.
- Samples were analysed with transmitted light to detail the transparent mineral suite. A particular focus was to document size, distribution and zonation of:
    - Feldspars – microcline/plagioclase (albite)
    - Alteration minerals – chlorite/sericite/carbonate
    - Accessory Minerals – rutile/zircon/monazite
- Samples were analysed with reflected light to detail the opaque mineral suite. A particular focus was to document size, texture, distribution and zonation of:
    - Iron Oxides – hematite/magnetite
    - Sulphides – pyrite/chalcopyrite
    - Accessory Minerals - rutile/zircon/monazite
- Software and camera packages were used to image minerals, mineral relationships and textures of interest.

Scanning Electron Microscope (SEM)

- Samples were carbon coated by Adelaide Microscopy staff.
- Equipment used:
    - Quanta 450 SEM – Instrument includes EDAX TEAM Energy Dispersive X-ray Spectroscopy (EDS) with silicon drift detector (SDD) detector and back-scatter electron (BSE) detector.
    - Phillips XL40 SEM – Instrument includes EDAX Genesis EDS.
        - The Phillips XL40 SEM is equipped with a tungsten filament for imaging of sample surfaces. A solid state backscattered electron detector enables mean atomic number imaging and the two thin film EDS detectors allow for X-ray analysis. The XL40 has a large stage area suitable for larger samples–, allowing up to 150mm of lateral movement and 45mm of vertical movement
- SEM was operated in back-scatter mode (BSE) at:
    - Accelerated voltage of 20kv
    - Spot size of 5 microns
- Software and camera packages were used to image minerals, mineral relationships and textures of interest.
- The BSE imaging allowed observations on minerals of interest, including their speciation and the micro-scale association between gangue, alteration and ore minerals. Their fine textures, mineral intergrowths, compositional zoning and inclusions were also observed and captured.
- Qualitative analysis of minerals was performed using EDAX to further analyse mineral characteristics.

Laser Ablation Inductively Coupled Plasma Mass Spectrometry (LA-ICP-MS)

- The LA-ICP-MS used was an Agilent HP-7500 Quadrupole ICPMS. This machine is equipped with a New Wave UP-213 Nd:YAG laser ablation system running on MeoLaser 213 software. Glitter software was used for data reduction. Several samples were analysed on the Resonetics LA-ICP-MS.
    - The laser ablation ICP-MS system is used for micro sampling of solid material for trace element, predominately cation analysis. Detection limits reach to the ppb range allowing for true trace element analysis of a wide variety of solid geological material.
- The settings were:
    - Spot size 30 µm
    - Pulse rate of 5 Hz
    - Power rate of 80%; post 28/6/13 machine maintenance used 52%
    - Analysis time of 80 seconds with 30 seconds of background (laser off)
- Several thin sections were selected for LA-ICP-MS analysis based on minerals observed in the SEM analysis; targeting iron oxides, feldspars and accessory minerals.
- The element suite analysed on the New Wave LA-ICP-MS included (Resonetic LA-ICP-MS analysed ^{49}Ti and ^{56}Fe):

	Dwell Time New Wave	Dwell time Res		Dwell Time New Wave	Dwell time Res		Dwell Time New Wave	Dwell time Res		Dwell Time New Wave	Dwell time Res		Dwell Time New Wave	Dwell time Res		Dwell Time New Wave	Dwell time Res
^{23}Na	10	10	^{48}Ti	30		^{60}Ni	30	10	^{95}Mo	30	10	^{153}Eu	30	40	^{175}Lu	30	40
^{24}Mg	30	10	^{49}Ti		10	^{65}Cu	30	10	^{118}Sn	30	10	^{157}Gd	30	40	^{181}Ta	30	20
^{27}Al	30	10	^{51}V	50	10	^{66}Zn	30	10	^{121}Sb	30	10	^{159}Tb	30	40	^{182}W	30	20
^{29}Si	10	10	^{53}Cr	30	10	^{75}As	30	10	^{137}Ba	30	10	^{163}Dy	30	40	^{206}Pb	30	20
^{31}P	30	10	^{55}Mn	30	10	^{85}Rb	30	10	^{139}La	30	40	^{165}Ho	30	40	^{207}Pb	30	20
^{39}K	10	10	^{56}Fe		10	^{88}Sr	30	10	^{140}Ce	30	40	^{166}Er	30	40	^{208}Pb	30	20
^{43}Ca	10	10	^{57}Fe	30		^{89}Y	30	40	^{141}Pr	30	40	^{169}Tm	30	40	^{232}Th	30	20
^{45}Sc	30	10	^{58}Fe	30		^{90}Zr	30	10	^{146}Nd	30	40	^{172}Yb	30	40	^{238}U	30	20
^{47}Ti	30		^{59}Co	50	10	^{93}Nb	30	10	^{147}Sm	30	40						

- Calibration was conducted in the following format:

  Iron Oxides, feldspars, ilmenite, jacobsite & rutile.
    - 2 x BRC2 standard
    - 2 x BHVO internal standard
    - 10-12 x mineral sample spots per slide
    - 2 x BHVO internal standard
    - 2 x BRC2 standard

  Titanite, zircon, apatite, pyrolusite
    - 2 x NIST610 standard
    - 2 x NIST612 internal standard
    - 10-12 x mineral sample spots per slide
    - 2 x NIST612 internal standard
    - 2 x NIST610 standard

Kutnohorite
  - 2 x MACS3 standard
  - 2 x NIST610 internal standard
  - 10-12 x mineral sample spots per slide
  - 2 x NIST610 internal standard
  - 2 x MACS3 standard

Pyrite
  - 2 x MASS standard
  - No internal standard
  - 10-12 x mineral sample spots per slide
  - No internal standard
  - 2 x MASS standard

- Internal standard concentrations for data reduction in glitter were as follows:
  - Microcline - 18.32 wt% Al2O3
  - Albite – 20.35 wt% Al2O3
  - Hematite – 89.9776 wt% Fe
  - Magnetite – 93.0909 wt% Fe
  - Rutile – 100 wt% TiO_2
  - Monazite – 29.58 wt% P_2O_5
  - Zircon – 58.27 wt% ZrO_2
  - Hornblende – 11.84 wt% CaO
  - Titanite – 30.29 wt% TiO_2
  - Apatite – 55.07 wt% CaO
  - Kutnohorite – 27.23 wt% CaO
  - Ilmenite – 60.01 wt% TiO_2
  - Calcite – 56.03 wt% CaO
  - Jacobsite – 9.48 wt% FeO; 52.67 wt% Fe_2O_3; tot 62.15 wt %
  - Pyrite – 46 wt% Fe
  - Xenotime – 61.4 wt% Y_2O_3/38.60 wt% P_2O_5
- The results are based on the measured concentrations leading to detection limits being calculated for each element from the different hematite, magnetite or feldspar spot analyses.
- Images of spot locations were captured for future reference.

Electron Microprobe Analysis (EPMA)

- Several thin sections were selected for EPMA.
- A CAMECA SX-51 instrument with wavelength-dispersive spectrometers was used for EPMA.
- EPMA was used for quantitative compositional data for representative REE-bearing sulphides, feldspars and oxides (previously observed through SEM). It was also used to investigate F enrichment of sericite.
- The elements analysed using the X-ray lines and standards are given in Appendix 1.

LA-ICP-MS element mapping

- LA-ICP-MS mapping was conducted using a Resonetics M-50-LR 193-nm Excimer laser microprobe coupled to an Agilent 7700cx Quadrupole ICP-MS. The M-50 utilises a two-volume small volume ablation cell designed by Laurin Technic Pty. Ablation was performed in an atmosphere of UHP He (0.7 l/min), and upon exiting the cell the aerosol cell is mixed with Ar (0.93 l/min) immediately after the ablation cell, after which the mix is passed through a pulse-homogenizing device or “squid” prior to direct introduction into the torch. The ICPMS was optimized daily to maximize sensitivity on isotopes of the mass range of interest, while keeping production of molecular oxide species (i.e., 232Th16O/232Th) and doubly charged ion species (i.e., 140Ce2+/140Ce+) as low as possible, and usually <0.2%.
- Imaging was performed by ablating sets of parallel line rasters in a grid across the sample. A beam size of 5 microns and a scan speed of 5 µm/s were chosen which resulted in the desired sensitivity of elements of interest, and adequate spatial resolution for the study. The spacing between the lines was kept at a constant 5 µm to match the size of the laser beam used. The effect of redeposition during mapping was minimized by preablating each line prior to its main data collection run. A laser repetition of 10 Hz was selected at a constant energy output of 100mJ, resulting in an energy density of ~6 J/cm2 at the target. Using these beam conditions depth of ablation during mapping was around 5-10 µm. A set of 21 elements were analysed with dwell time for all masses set to 0.003 s, resulting in a total sweep time of ~0.07 s. A 30 second background acquisition was acquired at the start of every raster, and to allow for cell wash-out, gas stabilisation, and computing processing, a delay of 15 s was used after each line. Identical rasters were done on the standard glass NIST 610, and reference materials BCR-2G and BHVO-2G at the start and end of a mapping run.
- Images were compiled and processed using the program Iolite developed by the Melbourne Isotope Group at Melbourne University. Iolite is an open source software package for processing ICP-MS data, and is an add-in for the data analysis program Igor developed by WaveMetrics. A typical mapping run was analysed over a 6-7h session, in which significant instrument drift could occur. To correct for this, standards were analysed immediately before and after the run to assess drift and if present, was corrected for by applying a linear fit between the two sets of standards. Following this, for each raster and every element, the average background was subtracted from its corresponding raster, and the rasters were compiled into a 2-D image displaying combined background/drift corrected intensity for each element.

APPENDIX B - SAMPLE SUMMARY

Sample ID	Hole ID	Sample depth (m)	SAMPLE TYPE	SAMPLE DESCRITPTION
MV01			FIELD SAMPLE	Rhyolite porphyry
MV02			FIELD SAMPLE	Rhyolite porphyry
ML01	ML001DD	85.2	HALF CORE SAMPLE	Felsic breccia
ML02	ML001DD	98.5	HALF CORE SAMPLE	banded felsic gneiss with granite veinlet
ML03	ML001DD	100.9	HALF CORE SAMPLE	Granitic vein
ML04	ML001DD	121.6	HALF CORE SAMPLE	felsic fine grain banded gneiss
ML05	ML001DD	124.8	HALF CORE SAMPLE	hybrid granite/gneiss
ML06	ML001DD	128.9	HALF CORE SAMPLE	Granite
ML07	ML001DD	137.2	HALF CORE SAMPLE	Granite
ML08	ML001DD	142.9	HALF CORE SAMPLE	Granite
ML09	ML001DD	145.7	HALF CORE SAMPLE	Granite - k alteration
ML10	ML001DD	156.8	HALF CORE SAMPLE	Granite
ML11	ML001DD	168.0	HALF CORE SAMPLE	Brecciated granite
ML12	ML001DD	173.7	HALF CORE SAMPLE	silicified brecciated granite
ML13	ML001DD	177.7	HALF CORE SAMPLE	felsic volcaniclastic
ML14	ML001DD	202.8	HALF CORE SAMPLE	foliated felsic volcaniclastic
ML15	ML001DD	227.7	HALF CORE SAMPLE	flow banded rhyolite-dacite
ML16	ML001DD	232.3	HALF CORE SAMPLE	disrupted flow banded rhyolite
ML17	ML001DD	237.9	HALF CORE SAMPLE	banded felsic volcanic with ferromag zones
PS01	PRCD1	227.0	HALF CORE SAMPLE	hematite ore brecciated
PS02	PRCD1	233.5	HALF CORE SAMPLE	Fe and Si dominated breccia
PS03	PRCD1	258.6	HALF CORE SAMPLE	Chl dominated fine grained metasediment
PS04	PRCD1	267.0	HALF CORE SAMPLE	massive fine grained metasediment
PS05	PRCD1	272.6	QUARTER CORE SAMPLE	pale green altered/veined chl rich metasediment
PS06	PRCD1	275.0	HALF CORE SAMPLE	metasediment with minor brecciaiton
PS07	PRCD1	279.2	HALF CORE SAMPLE	minor crackle breccia in metasediment
PS08	PRCD1	282.2	HALF CORE SAMPLE	vuggy metasediment with sparry qz
PS09	PRCD1	287.0	HALF CORE SAMPLE	ductile deformation of metasediment
PS10	PRCD1	297.0	HALF CORE SAMPLE	qz stringers in metasediment
PS11	PRCD1	299.4	HALF CORE SAMPLE	qz-co3 vein with chl alt
PS12	PRCD1	308.0	HALF CORE SAMPLE	metasediment with smokey qz veins
PS13	PRCD1	335.0	HALF CORE SAMPLE	metasediment with smokey qz veins
PS14	PRCD1	340.0	HALF CORE SAMPLE	foliated/blebby metasediment with flow banding
PS15	PRCD1	352.0	HALF CORE SAMPLE	metasediment less intense flow-banding
PS16	PRCD1	373.0	HALF CORE SAMPLE	chl-plag dominated metasediment

APPENDIX C - IOCG TARGETING EXPLORATION EFFORTS CONDUCTED WITHIN ARRIUM'S MIDDLEBACK RANGES EXPLORATION AND MINING TENEMENTS (McIntyre 2001, Cave 2010).

Year	Type of Exploration	Location	Company
1999	Stream sediment sampling	Regional	Helix/BHP
1999	Calcrete sampling	Regional	Helix/BHP
1999	Soil traverses	Regional	Helix/BHP
1999	Rock chip sampling and geological mapping	Regional	Helix/BHP
1999	Ground Magnetics and Geophysics	Regional	Helix/BHP
1999	Drill core logging and assaying	Regional	Helix/BHP
2000	RAB Drilling	Moola Prospect	Helix/BHP
2000	RC Drilling	Moola Prospect	Helix/BHP
2000	Calcrete sampling	Moola Nth	Helix/BHP
2000	RC and Diamond Drilling	Princess Prospect	Helix/BHP

APPENDIX D – LA-ICP-MS TRACE ELEMENT DATA FOR PYRITE

Summary of LA-ICP-MS trace element data for pyrite (ppm).

		Mn	Ni	Cu	Zn	As	Mo	Sn	Sb	Ba	W	^{206}Pb	^{207}Pb	^{208}Pb
PS03	mean	93.2	1286	20669	10.3	189	1.93	5.34	43.9	2.25	0.02	287	270	294
	std. dev.	88.5	6.71	3783	3.97	111	0.87	4.26	14.1	0.65	0.00	18.2	19.7	12.2
	min	4.66	1280	16886	6.32	78.8	1.06	1.08	29.8	1.60	0.02	269	250	282
	max	182	1293	24452	14.3	300	2.79	9.60	58.0	2.89	0.02	305	290	306
PS12	mean	2.31	99.3	474	6.52	5590	4.08	0.16	3.97	5.96	0.06	660	765	732
	std. dev.	0.34	70.5	94.5	1.71	1109	7.49	0.07	0.69	8.68	0.09	510	620	568
	min	1.79	23.5	332	4.65	4129	0.10	0.07	2.97	0.39	0.00	220	245	246
	max	2.78	208	599	9.11	7156	19.0	0.25	5.06	23.2	0.23	1643	1969	1831
PS13	mean	49.3	3938	295	21.7	2573	13.1	0.40	19.2	32.7	0.13	895	1044	1028
	std. dev.	33.8	1629	146	10.6	969	15.7	0.54	7.04	10.9	0.15	511	608	579
	min	3.21	1981	39.8	6.73	1045	0.58	0.07	5.64	18.0	0.02	177	218	198
	max	91.2	7655	569	38.1	4632	50.5	1.96	28.4	48.3	0.53	1955	2279	2131

Elements removed because 95% below detection limit = Na, V & Cr. Fe was removed as it was used as the internal standard. The Co content of pyrite is not relevant to this study and as such is not displayed.

APPENDIX E – LA-ICP-MS TRACE ELEMENT DATA FOR ZIRCON

Summary of LA-ICP-MS trace element data for zircon (ppm).

		Na	Mg	Al	Si	P	K	Sc	^{49}Ti	V	Cr	Mn	^{56}Fe	Co	Ni	Cu	Zn	As	Rb	Sr	Y	Nb	Mo	Sn
ML04 (n-4)	mean	237	40.1	163	190051	4881	119	518	40.5	2.25	3.37	77.8	1008	0.13	0.91	2.76	9.13	7.08	2.04	3.73	2273	3.00	11.1	1.98
	std. dev.	164	35.2	202	21712	7388	161	39.0	9.68	1.17	2.23	93.5	1143	0.05	0.59	3.44	8.46	4.48	2.10	3.02	1218	0.41	10.0	2.50
	min	47.9	10.5	4.19	167065	58.5	7.08	474	27.8	0.47	1.32	3.10	87.8	0.08	0.39	0.58	0.78	1.78	0.19	0.31	1499	2.39	4.73	0.25
	max	492	100	500	224780	17662	397	577	53.9	3.58	6.65	237	2943	0.21	1.92	8.71	23.3	13.8	5.58	8.58	4380	3.46	28.4	6.30
		Sb	Ba	La	Ce	Pr	Nd	Sm	Eu	Gd	Tb	Dy	Ho	Er	Tm	Yb	Lu	Ta	W	^{206}Pb	^{207}Pb	^{208}Pb	Th	U
	mean	9.07	5.41	1.25	25.1	2.07	16.3	18.3	4.95	72.2	20.4	230	78.8	347	69.9	627	115	1.41	1.31	552	79.9	63.0	170	393
	std. dev.	7.68	3.93	0.78	6.32	1.13	8.00	9.00	2.14	34.6	10.7	122	41.7	178	33.3	259	48.2	0.46	1.26	128	40.5	38.0	84.2	141
	min	1.08	0.38	0.02	15.2	0.20	3.00	6.33	1.89	50.0	11.5	143	53.2	230	45.6	401	74.9	0.99	0.40	418	35.5	25.9	103	181
	max	21.7	11.4	2.05	32.5	3.26	23.0	31.6	7.90	132	38.6	440	151	655	127	1063	194	2.18	3.46	763	144	119	314	574
		Na	Mg	Al	Si	P	K	Sc	^{49}Ti	V	Cr	Mn	^{56}Fe	Co	Ni	Cu	Zn	As	Rb	Sr	Y	Nb	Mo	Sn
ML10 (n-2)	mean	2149	23222	47796	183035	2118	668	921	31816	64.0	10.1	2067	105579	56.3	32.3	164	297	129	11.9	270	17621	565	12.3	6.71
	std. dev.	295	9126	20254	13293	17.0	370	35.3	28924	18.4	4.13	446	42246	28.1	16.2	50.1	91.9	11.6	7.67	2.70	1619	260	3.08	3.77
	min	1854	14096	27541	169741	2101	298	885	2893	45.6	5.99	1621	63333	28.2	16.1	114	205	118	4.25	267	16002	305	9.20	2.94
	max	2445	32348	68050	196328	2135	1038	956	60740	82.3	14.2	2512	147825	84.4	48.5	214	389	141	19.6	273	19239	824	15.4	10.5
		Sb	Ba	La	Ce	Pr	Nd	Sm	Eu	Gd	Tb	Dy	Ho	Er	Tm	Yb	Lu	Ta	W	^{206}Pb	^{207}Pb	^{208}Pb	Th	U
	mean	513	75.7	359	2048	377	1987	1187	225	1938	451	3418	755	2455	445	3616	531	65.4	65.1	2043	278	218	2387	6687
	std. dev.	5.51	24.5	31.6	201	41.1	291	199	34.7	335	78.7	638	167	547	85.2	646	108	30.7	0.46	195	94.0	92.9	730	2651
	min	507	51.3	328	1847	336	1696	988	191	1603	372	2780	588	1909	360	2970	423	34.7	64.6	1848	184	125	1656	4035
	max	518	100	391	2249	418	2279	1387	260	2273	530	4055	922	3002	530	4262	639	96.1	65.5	2238	372	311	3117	9338
		Na	Mg	Al	Si	P	K	Sc	Ti	V	Cr	Mn	^{57}Fe	Co	Ni	Cu	Zn	As	Rb	Sr	Y	Nb	Mo	Sn
PS07 (n-6)	mean	*	6947	44019	140702	800	*	49.0	840	72.0	193	255	14771	3.12	16.7	*	33.5	61.7	76.2	22.1	1654	6.00	1.55	1.74
	std. dev.		4745	35811	53094	580		17.9	790	61.1	208	112	11686	1.30	10.7		24.8	35.1	64.7	12.5	724	2.71	0.94	1.13
	min		923	2185	69972	191		22.1	0.0	2.80	26.5	110	3786	1.13	5.45		14.4	8.61	1.24	8.15	733	2.90	0.60	0.41
	max		15965	95943	219129	1833		75.1	2028	173	634	410	38719	5.43	31.7		86.9	104	173	42.8	2718	10.9	3.17	3.34
		Sb	Ba	La	Ce	Pr	Nd	Sm	Eu	Gd	Tb	Dy	Ho	Er	Tm	Yb	Lu	Ta	W	^{206}Pb	^{207}Pb	^{208}Pb	Th	U
	mean	39.2	591	45.3	135	17.9	102	52.2	28.9	113	30.1	237	55.5	177	31.4	270	39.1	0.89	2.31	224	54.4	31.9	252	449
	std. dev.	23.0	512	75.2	139	13.6	58.5	19.8	12.0	49.6	13.5	107	24.5	75.2	12.8	104	14.6	0.34	0.91	75.0	19.0	17.0	107	192
	min	12.4	33.2	2.59	29.1	4.82	33.9	25.4	15.5	55.0	12.4	97.2	25.0	88.8	17.2	163	24.6	0.51	1.04	115	22.1	11.9	150	211
	max	70.8	1469	211	432	45.0	204	86.2	45.7	190	50.1	392	92.7	290	50.5	419	61.5	1.41	3.51	311	72.7	63.3	470	713
		Na	Mg	Al	Si	P	K	Sc	Ti	V	Cr	Mn	^{57}Fe	Co	Ni	Cu	Zn	As	Rb	Sr	Y	Nb	Mo	Sn
MV01 (n-9)	mean	2738	1390	10376	109683	1387	12264	144	14765	1.11	#DIV/0!	2476	18138	*	*	5.72	48.4	19.4	40.7	20.6	4902	141	2.81	33.7
	std. dev.	3015	2966	4753	14933	1883	20212	23.4	19637.0	0.85	#DIV/0!	1721	26288			3.49	63.6	30.3	78.4	10.0	4776	165	5.26	35.2
	min	34.0	54.1	290	76998	167	15.1	100	400	0.19	0.00	76.8	698			0.71	4.34	2.42	0.37	7.42	824	10.0	0.57	3.94
	max	9027	9712	17173	134100	5610	66436	181	52128	2.62	0.00	4826	77043			13.8	219	104	260	36.2	17603	467	17.7	109

Summary of LA-ICP-MS trace element data for zircon (ppm) cont.

		Sb	Ba	La	Ce	Pr	Nd	Sm	Eu	Gd	Tb	Dy	Ho	Er	Tm	Yb	Lu	Ta	W	^{206}Pb	^{207}Pb	^{208}Pb	Th	U
MV01 (N-9)	**mean**	4.52	148	73.7	171	20.5	91.8	41.9	12.2	113	36.5	353	101	348	61.9	542	72.3	8.01	3.52	160	29.8	26.2	168	287
	std. dev.	2.52	240	103	217	22.3	90.2	26.2	7.34	90.1	30.6	298	80.3	247	35.1	283	33.2	9.06	4.38	30.3	9.10	10.0	96.5	190
	min	0.72	1.63	3.76	20.5	3.21	17.5	14.5	3.39	34.1	9.02	85.0	27.5	115	23.0	231	30.9	1.11	0.63	109	16.1	13.7	47.2	115
	max	8.87	793	277	649	65.7	288	81.5	22.8	339	116	1137	313	995	150	1247	151	27.2	15.2	222	47.0	45.1	339	706
MV02 (n-7)		**Na**	**Mg**	**Al**	**Si**	**P**	**K**	**Sc**	**Ti**	**V**	**Cr**	**Mn**	**^{57}Fe**	**Co**	**Ni**	**Cu**	**Zn**	**As**	**Rb**	**Sr**	**Y**	**Nb**	**Mo**	**Sn**
	mean	48.5	57.2	199	81439	310	136	96.8	655	0.14	*	949	1033	0.29	0.25	1.25	26.9	3.12	1.66	4.96	2731	14.4	0.87	2.57
	std. dev.	95.1	56.6	201	9651	276	128	11.7	830.2	0.10		2090	776	0.40	0.26	0.76	40.6	3.62	1.92	6.89	1802	13.9	0.70	2.37
	min	0.40	0.91	3.46	66293	81.9	1.06	81.7	185.9	0.02		1.94	16.1	0.02	0.09	0.32	1.75	0.44	0.12	0.25	1086	2.17	0.27	0.28
	max	281	160	509	96600	911	369	121	2616	0.34		6062	1950	1.06	0.85	2.52	124	10.1	5.31	20.6	6737	44.2	2.48	7.57
		Sb	**Ba**	**La**	**Ce**	**Pr**	**Nd**	**Sm**	**Eu**	**Gd**	**Tb**	**Dy**	**Ho**	**Er**	**Tm**	**Yb**	**Lu**	**Ta**	**W**	**^{206}Pb**	**^{207}Pb**	**^{208}Pb**	**Th**	**U**
	mean	1.20	16.9	11.2	49.9	3.72	19.4	17.7	4.54	56.8	21.3	229	68.0	246	45.2	407	51.0	1.45	0.46	138	21.1	21.0	142	147
	std. dev.	2.10	27.1	6.35	31.7	2.10	8.63	9.03	3.23	30.1	13.3	149	41.3	141	23.7	191	20.6	1.05	0.48	45.0	8.29	11.0	104	90.3
	min	0.06	0.21	1.27	9.82	0.64	5.43	7.31	1.10	26.9	8.75	84.1	26.6	102	21.5	200	27.2	0.45	0.03	85.6	11.7	7.54	70.7	74.9
	max	6.29	81.85	23.28	112	7.89	33.5	30.3	10.5	112	46.8	513	152	533	94.9	786	94.3	3.73	1.23	211	32.3	34.4	386	349

* = 95% below detection limit; Ca was removed from the table as it had 95% of values below minimum detection limit (160). Zr was used as the internal standard and is omitted. The titanium (Ti) value given is an average of calculated total Ti based on measurement of ^{47}Ti and ^{48}Ti; in ML04 and ML10 the ^{49}Ti measurement is displayed. In ML04 and ML10 ^{56}Fe is displayed whereas in the rest of the samples ^{57}Fe is displayed.

APPENDIX F– WHOLE ROCK GEOCHEMISTRY OF SAMPLES

1. Moola Prospect (hole ID: ML001DD) drill core sample depth and whole rock geochemistry.

SAMPLE	DEPTH	Au	Bi	Ca	Cu	Fe	K	Na	Pb	S	Zn	Mo	U	Ba
ML01	85.2	<10	<5	1780	5	15200	35500	21500	15	200	22	0	5	290
ML02	98.5	<10	<5	5850	220	18600	26000	26100	<10	450	26	0	5	365
ML03	100.9	<10	<5	6050	39	15700	38700	17400	10	150	24	0	10	475
ML04	121.6	<10	<5	4500	5	14900	30600	16800	15	100	17	0	5	460
ML05	124.8	<10	<5	3540	250	19400	37900	14500	15	450	12	0	10	400
ML06	128.9	<10	<5	4300	750	23600	29800	20400	15	1000	35	0	20	330
ML07	137.15	10	20	4040	950	14600	43200	24200	25	1200	23	0	30	365
ML08	142.9	10	30	18100	850	12400	42400	26300	30	1100	15	0	30	395
ML09	145.7	<10	15	10500	1300	10900	40300	26700	20	1600	7	0	25	335
ML10	156.8	10	<5	12500	85	11500	42400	17600	20	250	10	0	35	355
ML11	168	<10	5	6600	1300	23000	26600	19400	<10	2000	35	0	10	375
ML12	173.65	40	20	2320	2900	14600	32000	10500	15	3700	25	0	10	335
ML13	177.7	30	85	2160	8600	16000	4560	1080	10	5400	17	0	10	40
ML14	202.8	<10	70	37200	43	95800	1260	24300	10	500	280	0	<4	120
ML15	227.7	<10	5	6850	<2	60200	24900	26300	<10	350	100	0	10	450
ML16	232.3	<10	35	23500	36	79500	10500	25100	<10	450	100	0	5	155
ML17	237.9	<10	<5	6450	8	59200	19900	22600	<10	350	80	0	5	350

2. Princess Prospect (hole ID: PRCD01) drill core sample depths and whole rock geochemistry.

SAMPLE	DEPTH	Au 1ppb	Ag 0.5ppm	As 1ppm	Bi 5ppm	Co 1 ppm	Cu 1ppm	Mo 1ppm	Pb 3ppm	Sb 5ppm	Zn 1ppm
PS01	227	4	1	4	<5	2	10	<1	<3	<5	3
PS02	233.5	120	<0.5	130	<5	13	94	2	8	<5	15
PS03	258.6	<1	<0.5	12	<5	17	47	2	6	<5	95
PS04	267	1	<0.5	12	<5	18	66	5	26	<5	78
PS05	272.6	<1	<0.5	7	<5	13	39	2	18	<5	64
PS06	275	<1	<0.5	7	<5	15	15	3	14	<5	76
PS07	279.2	<1	<0.5	12	<5	18	29	2	20	<5	74
PS08	282.2	<1	<0.5	9	<5	13	26	2	110	<5	79
PS09	287	<1	<0.5	15	<5	18	24	4	20	<5	73
PS10	297	1	<0.5	12	<5	15	16	1	24	<5	66
PS11	299.4	<1	<0.5	9	<5	12	19	2	30	<5	69
PS12	308	<1	<0.5	12	<5	16	35	<1	16	<5	73
PS13	335	<1	<0.5	9	<5	14	40	1	44	<5	78
PS14	340	2	<0.5	13	<5	17	80	3	90	<5	95
PS15	352	<1	<0.5	15	<5	17	58	2	34	<5	87
PS16	373	<1	<0.5	8	<5	11	37	3	10	<5	71

APPENDIX G Barioferrite $BaFe_{12}O_{19}$

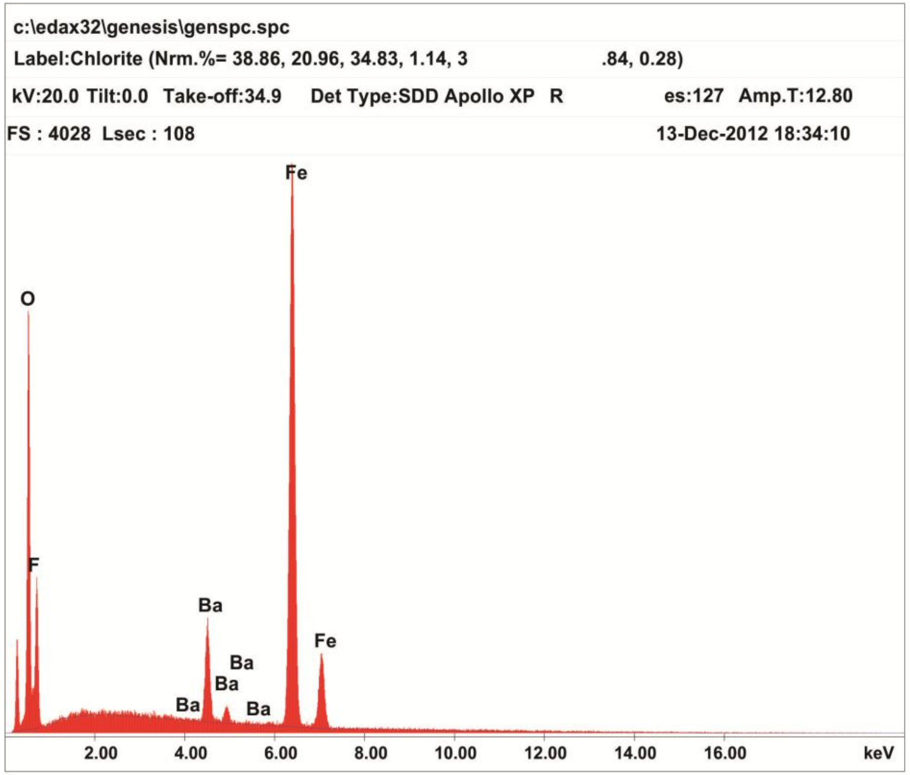

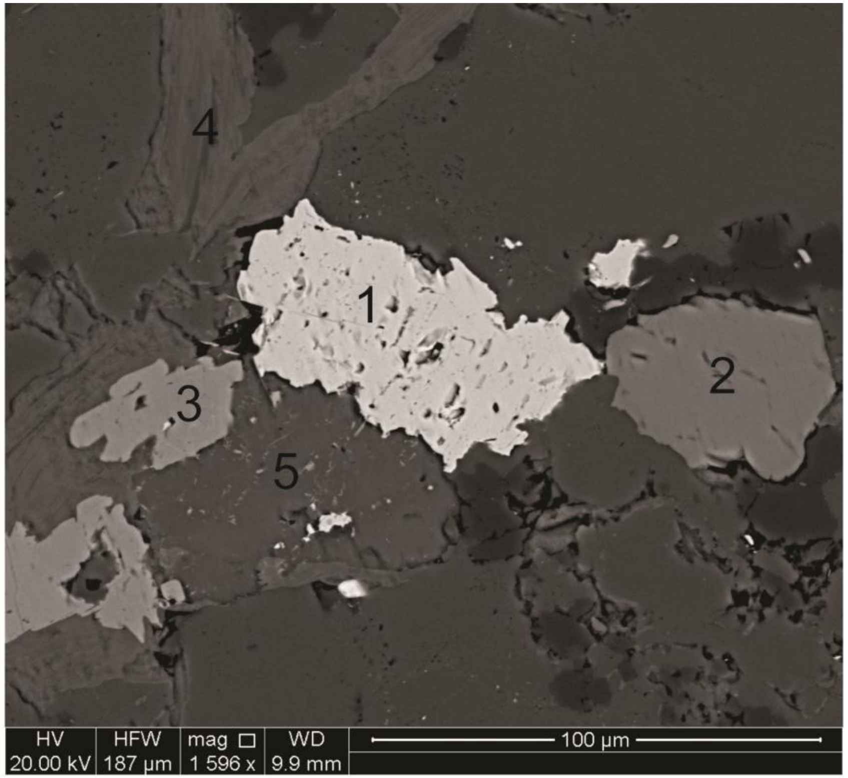

EDAX ZAF Quantification (Standardless)
Element Normalized
SEC Table : Default

Element	Wt %	At %	K-Ratio	Z	A	F
O K	14.25	36.69	0.0739	1.1512	0.4494	1.0030
F K	4.54	9.85	0.0188	1.0816	0.3806	1.0061
BaL	14.72	4.42	0.1390	0.8278	1.0650	1.0711
FeK	66.49	49.04	0.6367	0.9871	0.9701	1.0000
Total	100.00	100.00				

Element	Net Inte.	Bkgd Inte.	Inte. Error	P/B
O K	134.61	1.25	0.84	107.95
F K	38.86	1.73	1.61	22.50
BaL	58.05	9.45	1.45	6.14
FeK	387.53	5.43	0.50	71.35

Sample ID MI04 - Moola Prospect, granitic veinlet.
1 Barioferrite
2 Apatite
3 Rutile
4 Chlorite
5 Kutnohorite (?)

1 is the location for the SEM EDAX analysis for barrioferrite

APPENDIX H MINERAL LIST

SULPHIDES	
Mineral	**Composition**
Pyrite	FeS2 - cubic
Chalcopyrite	CuFeS2
Sphalerite	(Zn,Fe)S
Marcocite	FeS2 - orthorombic
Chalcocite	Cu2S
Covellite	CuS
Galena	PbS
Carrollite	CuCo2S4
Wittichenite	Cu3BiS3
Anilite	Cu7S4
Cuprobimutite	Cu10Bi12S23
Bornite	Cu5FeS4
idaite	Cu5feS6

OXIDES	
Mineral	**Composition**
Fe	
Magnetite	Fe3O4
Hematite	Fe2O3
Goethite	FeO(OH)
Siderite	FeCO3
Barioferrite	BaFe12O19
Ilmenite	FeTiO3
Dellafossite	CuFeO2
Jacobsite	MnFe2O3
Mn	
Pyrolusite	MnO2
Rhodochrosite	MnCO3
Manganoan Calcite	$(Mn,Ca)CO_3$
Kutnohorite	Ca(Mn,Mg,Fe)(CO3)2

GANGUE	
Mineral	**Composition**
Albite	NaAlSi3O8 (Na end member of plagioclase)
Ankerite	Ca(Fe,Mg)(CO3)2
Bardolite	K2Mg5FeFe4Al2Si12O40 - similar to chl (has K)
Biotite	K(Mg,Fe)3AlSi3O10(F,OH)2
Calcite	CaCO3
Ferrobustamite	Ca(Fe,Ca,Mn)(Si2O6)
Hornblende	Ca2(Mg,Fe,Al)5(Al,Si)8O22(OH)2
K-Feldspar	$KAlSi_3O_8$
Lime	CaO
Microcline	$KAlSi_3O_8$
Perthite	(K,Na)AlSi3O8
Plagioclase	(Na,Ca)(Si,Al)4O8
Quartz	SiO2
Sapphirine	$(Mg,Al)_8(Al,Si)_6O_{20}$
Tourmaline	$(Na,Ca)(Li,Mg,Al)(Al,Fe,Mn)_6(BO_3)_3(Si_6O_{18})(OH)_4$

ACCESSORY	
Mineral	**Composition**
Rutile	TiO2
Zircon	ZrSiO4
Monazite	(La,Ce,Nd)PO4
Apatite	Ca5(PO4)3(OH,F,Cl)
Barite	BaSO4
Xenotime	YPO4
Uraninite	UO2
Cassiterite	SnO2

ALTERATION	
Mineral	**Composition**
Sericite	KAl2(Si3Al)O10(OH,F)2
Chlorite	(Mg,Fe)3(Si,Al)4(OH)2(Mg,Fe)3(OH)6